CUINSE$_2$ AND RELATED ALLOY THIN FILM SEMICONDUCTORS

FOR PHOTOELECTROCHEMICAL HYDROGEN PRODUCTION

by

Jennifer Elyn Leisch

ProQuest Number: 10797140

![ProQuest](ProQuest logo)

ProQuest 10797140

A thesis submitted to the Faculty and Board of Trustees of the Colorado

School of Mines in partial fulfillment of the requirements for the degree of Doctor

of Philosophy (Applied Chemistry)

Golden, Colorado

Date _11 May 2006_

Signed: _____
Jennifer E. Leisch

Approved: _____
Dr. Scott A. Cowley
Thesis Advisor

Approved: _____
Dr. John A. Turner
Thesis Co-Advisor

Golden, Colorado

Date _May 9, 2006_

Approved: _____
Dr. Paul Jagodzinski
Professor and Head
Applied Chemistry and Geochemistry

ii

ABSTRACT

  Photoelectrochemical (PEC) water splitting directly produces hydrogen from sunlight and water at a semiconductor surface immersed in an electrolyte. PEC is a promising technology for the renewable production of hydrogen, however, semiconductor materials that can perform this reaction with high efficiency remain elusive. Thin film materials such as $CuInSe_2$ 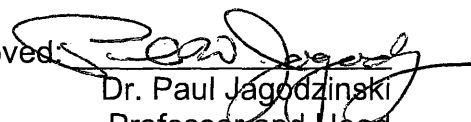(CIS) have demonstrated very high photovoltaic (PV) efficiencies, and have many potential low-cost deposition methods, one of which is electrodeposition. Band gap modifications to these commercial photovoltaic materials need to be made in order to create a viable photoelectrochemical water splitting system. Alloying gallium and sulfur into CIS can increase the band gap of these films, as well as modify surface energetics. In this work, gallium and sulfur containing CIS alloys were fabricated by the physical vapor enrichment of electrodeposited precursors. Graded profiling of gallium, sulfur, and indium was observed in these materials. The presence of the chalcopyrite crystalline phase was observed, and some films showed evidence of phase separation. This approach represents a potential low-cost method for fabricating ideal band gap thin films for both PV and PEC applications.

  Band gap and band edge grading are techniques employed in PV devices to increase system efficiencies. Band gap and band edge grading in $Cu(In,Ga)(Se,S)_2$ materials were investigated. An empirical equation to describe this grading based on the gallium and sulfur content in CIS was developed, and applied to prepared thin films. This equation was able to predict the

experimentally determined band gaps. This is an important tool for predicting material properties, and for guiding the further investigation of the dependence of material properties on band gap and band edge energetics.

Tandem devices using $CuGaSe_2$ (CGS) thin films deposited on a p-n Si junction were investigated as a possible way to overcome non-ideal surface energetics. Theoretical calculations show photovoltaic conversion efficiencies up to 33.1%, and photoelectrochemical conversion efficiencies up to 29.3%. Using single absorber CGS thin films, the ideal corrosion properties of the system were examined. These materials show cathodic protection under illumination, though hydrogen production under extended time periods shows some film instability. The electrodeposition of CGS thin films was examined as a possible low-cost method for tandem cell fabrication. Gallium incorporation into these films was dependent on parameters including solution composition, pH, and applied potential. Though gallium incorporation was achieved, no evidence of the crystalline chalcopyrite phase was observed in the as-deposited films. Further annealing of these materials will be necessary to obtain high-quality films.

TABLE OF CONTENTS

LIST OF FIGURES

LIST OF TABLES

ACKNOWLEDGEMENTS

scientists. Though it has been many years, your passion and influence are not forgotten.

For Saka

"Yes, my friends, I believe that water will one day be employed as fuel, that hydrogen and oxygen which constitute it, used singly or together, will furnish an inexhaustible source of heat and light, of an intensity of which coal is not capable. . .

There is, therefore, nothing to fear. As long as the earth is inhabited it will supply the wants of its inhabitants, and there will be no want of either light or heat. . . . I believe, then, that when the deposits of coal are exhausted we shall heat and warm ourselves with water. Water will be the coal of the future."

Jules Verne – The Mysterious Island, 1874

CHAPTER 1

INTRODUCTION

1. 1 Hydrogen as a Fuel

As our dependence on foreign oil increases and concerns about global climate change rise, the need to develop sustainable energy technologies is becoming increasingly significant. The United States is the largest consumer of petroleum in the world, utilizing over 20 million barrels of oil per day, of which 57.8% is imported[1]. As petroleum consumption continues to increase, our already problematic dependence on imported fuel will grow. Price fluctuations, political instability in exporting nations, and national security concerns are all critical issues associated with foreign oil dependence.

In 2002, world anthropogenic carbon dioxide emissions exceeded 24 billion metric tons, and this number is expected to rise to over 38 billion metric tons by 2025[1]. This increase in emissions is a product of an ever-increasing demand for energy, and a corresponding rise in the combustion of carbon containing fossil fuels such as coal, petroleum, and natural gas. Undisputable scientific evidence indicates significant changes in the global climate have occurred in recent years, and models predict global temperature increases ranging between 1.4 – 5.8°C by the year 2100[2]. Impacts of climate change and the resulting atmospheric warming are extensive, and know no political or geographic boundaries. These far-reaching effects will be manifested as environmental, economic, socioeconomic, and geopolitical issues.

Almost all of the energy consumed in the United States is from fossil fuels, with only 6% of energy usage from renewable sources in 2004, seen in Figure 1.1[1]. With an average solar irradiance of 1800kWh/m^2 in the U.S., it is estimated that a land area of roughly 10,000 square miles, half of it covered with 10% efficient photovoltaics, would meet the entire electricity needs of the nation[3]. Adding other renewable energy technologies to the mix, such as wind and biofuels, rapidly decreases this area, and highlights our domestic capacity to power the nation with pollution free renewable energy. Offsetting the projected increase in fossil energy use with renewable energy production will require large increases in renewable energy systems, as well as the ability to store and transport clean domestic fuels.

2004 U.S. Energy Consumption by Source (%)

Petroleum 40.23

Coal 22.45

Natural Gas 23.05

Nuclear 8.25
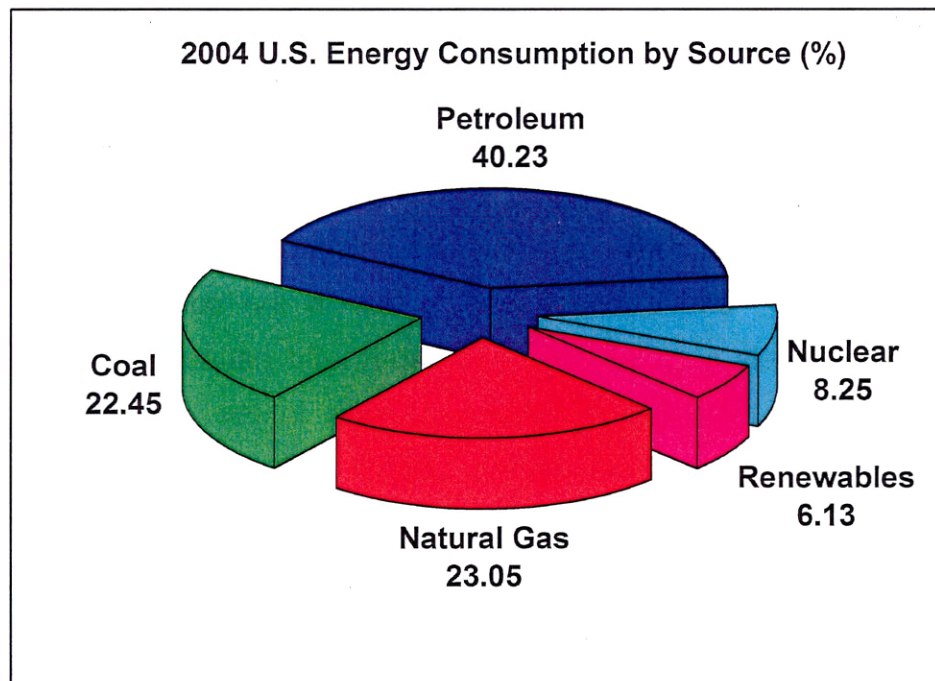
Renewables 6.13

Figure 1.1 Percent of US energy makeup by type. Data from the Energy Information Administration.

There are many environmental and economic benefits to the use of renewable energy for electricity generation. Renewable energy technologies implemented on small residential or neighborhood scales can be used for the distributed or de-centralized generation of power. Distributed generation can provide energy cost savings through the elimination of the high-capital cost equipment of a centralized power plant, as well as reducing transmission and distribution costs. Distributed generation also provides energy security, with more localized effects of power losses or shortages. Renewable energy systems such as solar photovoltaics and wind turbines are amenable to mass production, allowing the widespread utilization of these technologies. Mass producing smaller units for distributed generation can decrease the overall system cost of these renewable technologies, making them more cost competitive alternatives to fossil fuels for electricity generation.

Storage and transport of electricity generated from intermittent resources such as wind and solar is central to the widespread use of renewables. Many options exist for the storage of electricity, including batteries, flywheels, and pumped hydro. Each of these technologies has its associated limitations. While batteries for energy storage can have a high energy density, the drawbacks are their large weight, limited cycling lifetime, and possible inclusion of hazardous materials. Flywheel storage has a high efficiency, but low energy density. Pumped hydro can be a high capacity low-cost solution, but is very site specific.

Hydrogen created from water electrolysis is an option for energy storage and transport, and represents a pollution-free source of fuel when generated using renewable electricity. Hydrogen serves to blur the line between stationary

and mobile power applications, as it can be used as both a transportation fuel and for stationary electricity generation.

Hydrogen generated from water electrolysis using fossil fuel electricity has no point source pollution when used in a fuel cell or vehicle engine, but produces large amounts of CO_2 during electricity generation, and thus is not a viable option for truly carbon-free fuel. Of the 9 million tons per year of hydrogen produced in the United States, which is used mostly in the petroleum and agriculture industry, 95% results from steam reforming of natural gas[4]. Steam reforming proceeds via the two reactions seen in Equations (1.1) and (1.2), resulting in 4 moles of hydrogen, and one mole of CO_2 produced per mole of methane[5]. Though carbon byproducts are produced, this is the least carbon intensive form of hydrogen production from a fossil fuel, and may represent a promising transitionary technology on a path toward a renewable hydrogen economy. Ultimately though, renewable production of hydrogen is necessary to maintain a pollution-free fuel and avoid carbon containing byproducts.

$$CH_4 + H_2O \xrightarrow{700-1100°C} CO + 3H_2 \tag{1.1}$$

$$CO + H_2O \rightarrow CO_2 + H_2 \tag{1.2}$$
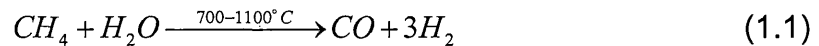
There are several pathways for renewable hydrogen production; those from solar energy are outlined in Figure 1.2[3]. Currently, the most cost effective method of renewable hydrogen production couples wind electricity to an electrolyzer, splitting water into hydrogen and oxygen. The current cost of hydrogen produced via this method is between $3-$7.40 per kilogram[1]

---

[1] One kilogram of hydrogen is considered roughly the energy equivalent of one gallon of gasoline.

delivered[6]. Though the energy comparison is between one gallon of gasoline and one kilogram of H_2, it is typically considered that fuel cell vehicles will have fuel efficiencies twice that of gasoline burning vehicles. This brings the current cost of hydrogen produced via wind-electrolysis to a competitive level of current gasoline fuel costs (2006 prices).
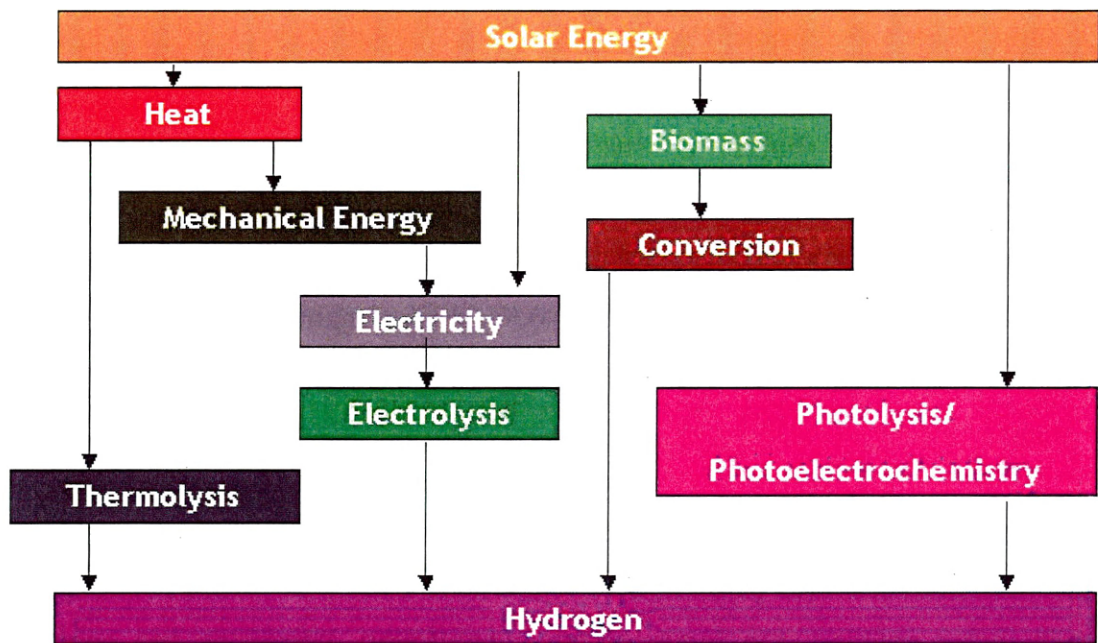
Figure 1.2 Sustainable Pathways to Hydrogen Production [3]

Water use is a worldwide issue, and is often cited as a major concern in developing nations. Fossil fuel electricity generation utilizes water, as does the production of gasoline, which requires about 300 billion gallons of water per year in the U.S. alone. It has been shown that the amount of water required to supply

hydrogen for an entire U.S. fuel cell vehicle fleet of 230 million vehicles is roughly 100 billion gallons of water per year[7]. By both phasing out fossil fuel electricity and the use of gasoline as transportation fuel, water usage in the U.S. can actually be lessened. Implementation of a renewable energy economy instead of centralized fossil fuel electricity generation in the developing world can lessen the impact of water use issues as these nations develop an energy infrastructure.

1.2 Direct Solar to Hydrogen Conversion

More direct routes to hydrogen production are photolysis and/or photoelectrolysis. These processes directly convert solar energy (photons) into hydrogen, without any intermediate conversion steps. The advantages of a direct water splitting method are two-fold: (a) an increase in system efficiency; and (b) a reduction in overall system costs.

Direct photolysis encompasses several methods of energy conversion. These processes can be classified as (a)photobiological, (b)photochemical, (c)thermochemical, and (c)photoelectrochemical systems. Photoelectrochemical (PEC) water splitting, the focus of this dissertation, combines the concept of photovoltaic electricity generation and water electrolysis into a single, monolithic device, seen in Figure 1.3. Here, a semiconductor electrode is immersed in an aqueous environment, electrically connected to a counter electrode. Upon illumination, charge carriers are generated in the material, which in turn can perform redox reactions at the electrode surface. Water is then oxidized at one electrode, and reduced at the other, forming O_2 and H_2, as seen in the half-reactions outlined in Equations 1.3 and 1.4. The generation of these two gases at

separate electrodes is an added benefit in this system, eliminating the additional cost and energy loss of gas separation.
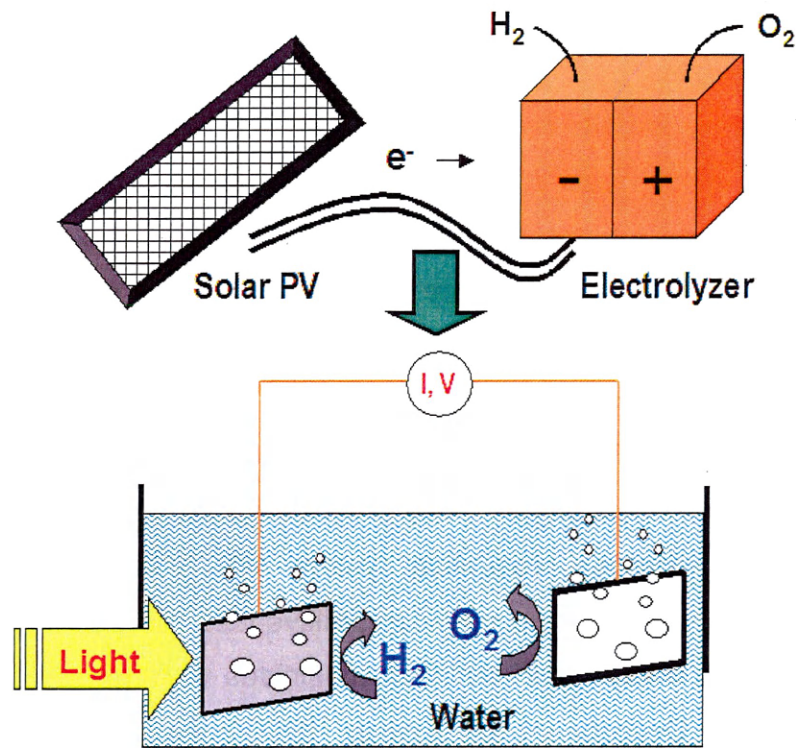
Figure 1.3 Schematic representation of a photoelectrochemical water splitting system, combining light collection and electrolysis into a single monolithic device.

1.3 Photoelectrochemical Systems

Photoelectrochemical energy conversion systems actually encompass two different electrochemical devices. Photoelectrochemical cells can be configured

as photovoltaic devices for current generation, or as photoelectrolysis cells for the conversion of light energy into chemical energy. In an electrochemical photovoltaic cell, a semiconductor electrode is immersed in an electrolyte with only one redox couple. This redox couple is both oxidized and reduced, causing electron flow in an external circuit which generates an electric current, with no net change in electrolyte composition. Photolysis cells, on the other hand, have two different redox couples, and chemical change occurs within the electrolyte solution. This results in the conversion of incident light energy to chemical energy, resulting in the opportunity to store and transport a chemical energy carrier. In this dissertation, the photoelectrolysis of water and the subsequent generation of hydrogen and oxygen are of interest, with the opportunity to store and utilize hydrogen as an energy carrier are studied.

In 1995, Bard and Fox declared the splitting of water by sunlight to be one of the "Holy Grails" of chemistry[8]. They proposed universal requirements for a realistic renewable hydrogen production system: 10% solar energy conversion efficiency; a 10 year lifetime; and cost competitiveness with hydrogen produced from fossil fuel. This "Holy Grail" definition coincides with the requirements put forth by the U.S. Department of Energy (DOE) for photoelectrochemical hydrogen production systems. These requirements are outlined in Table 1.1, which shows 2010, 2015, and commercialization goals for device efficiency and durability[9].

Table 1.1 DOE technical targets for PEC hydrogen production systems.

DOE Targets	2010	2015	Commercial
Efficiency	8%	10%	16%
Durability	1,000hrs	5,000hrs	15,000hrs

Photoelectrochemical systems can be classified by several cell structures, two of which, single-electrode and bi-photoelectrode systems, will be discussed. Single-electrode photoelectrolysis systems consist of a semiconductor photoelectrode, either n-type, p-type, or tandem, and a conducting metal counter electrode, often platinum, seen in Figure 1.4. If the material is p-type, the reduction of water occurs by electrons at the photocathode, resulting in the formation of H_2. Electron vacancies (holes) are transported through the external circuit to the metal anode where oxygen is produced. The resulting H^+ ions then diffuse through the electrolyte back to the photocathode for further hydrogen production. These two half-reactions comprise the overall splitting of water into H_2 and O_2. In n-type systems, oxidation occurs at the semiconductor electrode surface and reduction at the counter electrode, and an analogous mechanism can be described.
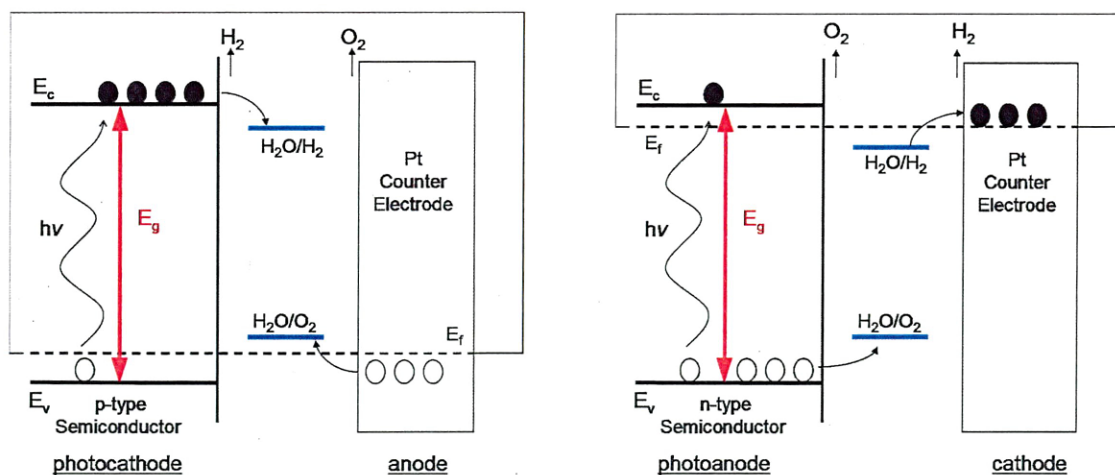
Figure 1.4 (a) A single-electrode PEC system using a photocathode; (b) a single-electrode PEC system using a photoanode.

A bi-photoelectrode system utilizes both a semiconductor anode and cathode, requiring simultaneous illumination. In this scheme a p-type photocathode and an n-type photoanode are used. Both electrodes absorb solar energy, converting it into charge carriers, after which both reduction and oxidation occur, forming H_2 and O_2 as in the previously discussed mechanisms. Efficiencies in such a system are limited by the lowest current density electrode.

The splitting of water into hydrogen and oxygen is a reduction-oxidation reaction, with both reactions necessary to have the overall result. The overall red-ox reaction occurs as:

$$\frac{1}{2}O_{2(g)} + 2H^+ + 2e^- \rightarrow H_2O_{(aq)} \qquad E^0 = +1.23V \ (vs. \ NHE) \tag{1.3}$$

$$2H^+ + 2e^- \rightarrow H_{2(g)} \qquad E^0 = 0.00V \ (vs. \ NHE) \tag{1.4}$$

$$H_2O \rightarrow \frac{1}{2}O_{2(g)} + H_{2(g)} \qquad E^0 = -1.23V \ (vs. \ NHE) \tag{1.5}$$
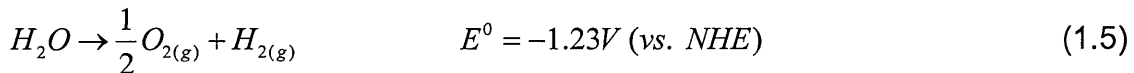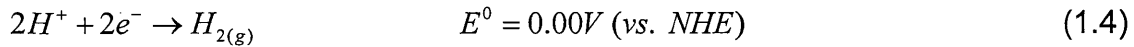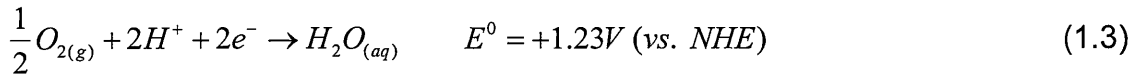
The reduction of water occurs through a mechanism involving protons in solution, seen in Equation (1.4). Since the mechanism involves H^+, the reaction potential depends on the pH of the electrolyte. The Nernst Equation given in Equation (1.6) gives the electrode potential relationship based on reactant concentrations, where R is the ideal gas constant, T is temperature, n is the number of electrons transferred, and F is the Faraday constant. This relationship tells us that the potential for the water splitting redox reactions is shifted by ~59mV for every change in pH unit.

10

$$E = E^0 - \frac{RT}{nF} \log Q = 1.23V - .059 pH \qquad (1.6)$$

Figure 1.5 shows the reduction and oxidation potentials of water as a function of pH. The importance of these potentials is discussed in the next section.
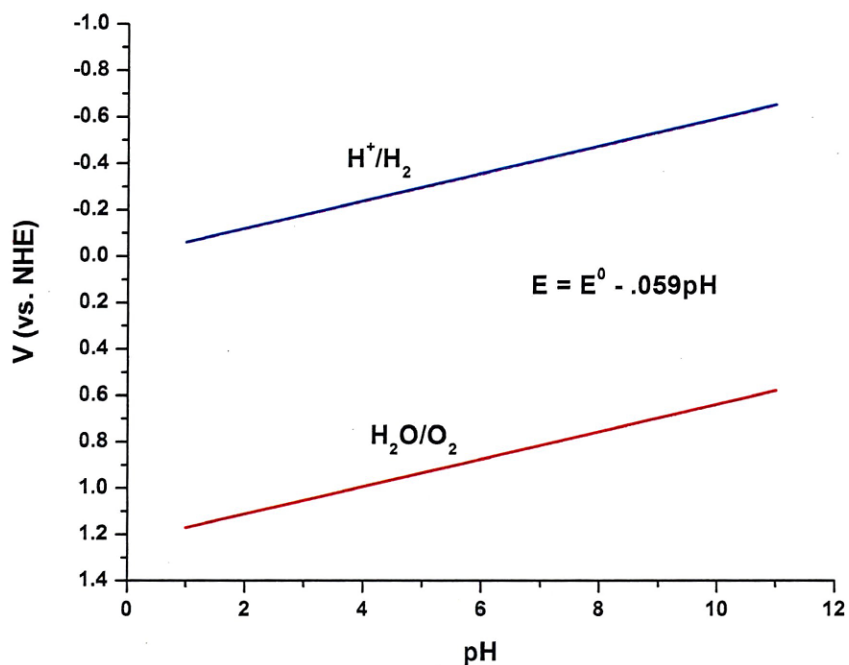
Figure 1.5 The pH dependence of the water reduction and oxidation potentials vs. NHE.

1.4 Photoelectrochemical H₂ Production Material Requirements

Electrode materials for PEC hydrogen production must be carefully chosen. There are several requirements that must be simultaneously satisfied within the semiconductor material to create a viable system. The main criteria for this application include the semiconductor band gap (E_g), the band edge positions, efficient charge transfer at the semiconductor surface, and corrosion resistance.

The semiconductor band gap is intimately related to the overall solar energy conversion efficiency of the material. In a semiconductor, only photons with energy greater than or equal to the band gap can be absorbed, and thus converted to charge carriers by the electrode. The electrochemical potential needed for water splitting is 1.23V (vs. NHE) at 25°C. This potential is the lowest allowable value for the semiconductor band gap. Due to overpotentials and system non-idealities, more energy is required, and the actual voltage needed for the reaction can be estimated between 1.7 and 2.0eV. These overpotentials arise from energy loss due to recombination of charge carriers, resistance both within the electrode and at the contacts, kinetics of the electron transfer reactions, and diffusion and mass transfer limitations within the electrolyte[10]. The upper limit of the allowable material band gap is related to absorption of the solar energy spectrum. Figure 1.6 shows the atmospheric photon flux as a function of photon energy, which decreases as photon energy increases. At larger band gaps, less solar energy is available for absorption, due to lower photon flux. The amount of current generated in an illuminated semiconductor material is found by integrating the photon flux from short wavelengths to the limiting wavelength of optical absorption (the band gap). The photons in this range are those available for generation of electron-hole pairs in the semiconductor. Ideally, the band gap

12

of the electrode material will remain below 2.0eV to optimize energy absorption and overall solar conversion efficiency by taking advantage of the greater photon flux at lower energies.

$$J = \int_{E_i}^{\infty} N(E) \, dE$$
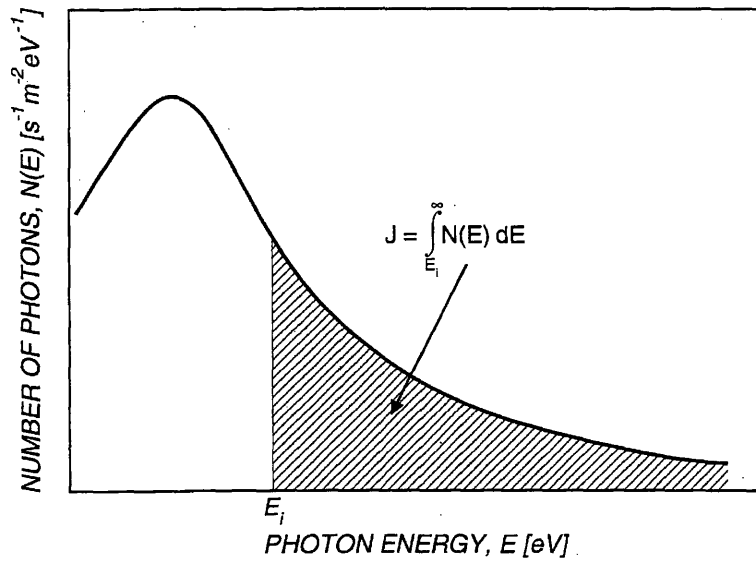
Figure 1.6 This shows the intensity of the light spectrum as a function of photon energy. Only the photons with energy greater than E_i are available for energy conversion. (J = photon flux) [11]

The band edge positions at the semiconductor electrolyte interface (Appendix 1) must be energetically positioned to favor the water redox reaction. Only electrons with a more negative potential than the H_2O/H_2 reduction potential will be transferred from the conduction band to the solution for the reaction to occur. Analogously, only holes (electron vacancies) at a higher potential than that of the H_2O/O_2 oxidation potential can be used in this reaction. The valence band and conduction band position at the interface must thus be positioned to straddle

the discussed redox potentials of water at the given operating pH, as shown in Figure 1.7.
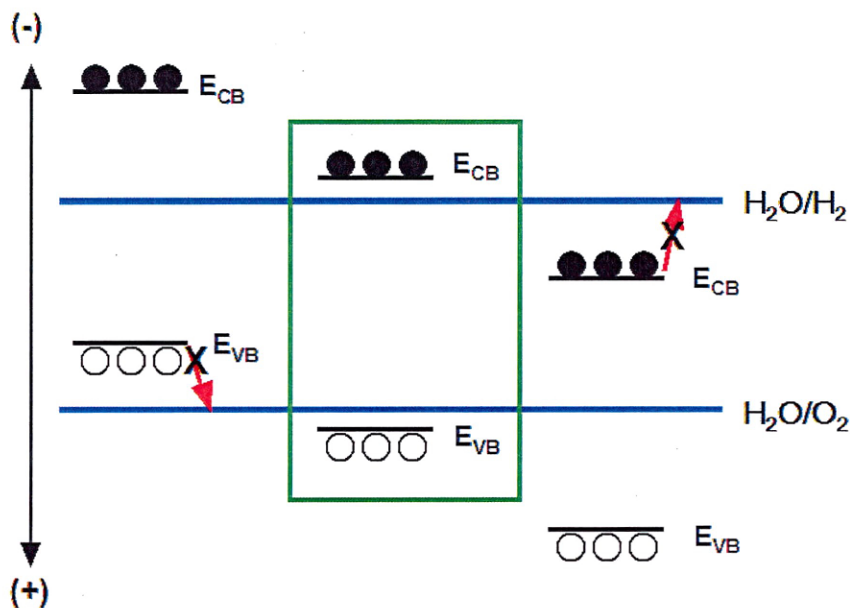
Figure 1.7 Band edge position requirements for a PEC semiconductor material. The conduction band (E_{CB}) and valence band (E_{VB}) energies must straddle the water redox potentials.

The conduction band edge, where reduction occurs, must be more negative than the water reduction potential. The energetics of the semiconductor/electrolyte interface is often determined by adsorbed H^+ and OH^- solution species, depending upon pH[12]. The position of the conduction band edge at a semiconductor/electrolyte interface often follows Nernstian pH dependence. Thus, as the pH of the electrolyte changes, the band edge energies and water splitting potentials change with pH.

Transfer of electrons (holes) from the semiconductor surface to the electrolyte for reduction (oxidation) must occur rapidly. Charge carriers that are not quickly transferred across the interface can build up at the surface of the material. Charge build-up can give rise to semiconductor corrosion or lead to shifting of the band edge positions at the interface, which can further inhibit the red-ox reaction.

Lastly, robustness of the material must be taken into consideration. Lifetimes of these materials are important when factoring in operating lifetime, and frequency of replacement. Typically, the band gap of a material is an indication of the bond strength, with high band gap materials such as metal oxides being more resistant to corrosion. Materials for photoanodes are chosen based on oxidation characteristics, with metal-oxide materials often favored due to their oxidation resistance. P-type non-oxide semiconductors are often chosen as photocathodes since the reduction reaction occurs at the semiconductor surface where the material is protected from oxidation. Cathodic corrosion is still an issue in these non-oxide materials, and often small amounts of noble metal catalyst such as Pt are plated on the surface. Corrosion of the semiconductor surface competes with electrolyte redox reactions, the kinetics of which determines the outcome of the competing reactions[12].

1.5 Review of Photoelectrochemical Materials

There are numerous materials under investigation for semiconductor electrodes in PEC systems. The importance of material research for this application is perhaps put best by Bak, et al, "... Commercial applications for

hydrogen generation… will be determined by the progress in materials science and engineering applied to the candidate materials for photoelectrodes." [11]

For clarification, this discussion divides these materials into several categories: (a) metal-oxide materials, (b) crystalline inorganic materials, (c) advanced hybrid and tandem materials, and (d) thin films. Each material set is discussed in detail, with the focus of this research on tandem and thin film semiconductor electrodes. To date, the highest efficiencies and lifetimes achieved within each classification are shown in Table 1.2.

Table 1.2 Some lifetime and efficiency milestones achieved by PEC materials.

Cell Type	Material	Efficiency	Durability	REF
Single Electrode	Oxides	<1%	Longest	[11]
Tandem Cell	GaAs/GaInP$_2$	12.4%	Low	[13]
Dye Sensitized	Oxides	4.5%	Dye Instability	[14]
Single Electrode	GaN	<1%	High	[15]

1.5.1. Metal-Oxide Electrodes

Metal-oxides typically yield n-type semiconductor electrodes, which are used as photoanodes in PEC cells. Semiconductor metal-oxide materials have high band gaps, in the range of 2.3 – 3.7eV[11]. The large band gaps of these materials contribute to both desirable and detrimental consequences for PEC water splitting. High band gaps and the correspondingly high bond strength in these materials contribute to corrosion resistance and stability in aqueous solution. Satisfaction of this important requirement in PEC systems makes these oxide materials popular candidates for much of the current PEC research.

16

Though these materials are robust, limitations also arise from the high material band gap. Metal oxides have low solar energy absorption, since only photons with energy greater than or equal to the band gap can be absorbed. As discussed, low photon flux in this portion of the solar spectrum yields less available energy for photoconversion.

Another common challenge with these materials is the lack of band edge overlap, which is required for hydrogen production in a non-biased cell. The conduction band is generally too positive in many of the oxides for the water reduction reaction to occur. Typically, the valence band position in oxides is dictated by the O (2p) orbitals, and the conduction band positions from the metal s or p orbitals[16]. Band positions for several common oxide materials can be seen in Figure 1.8.
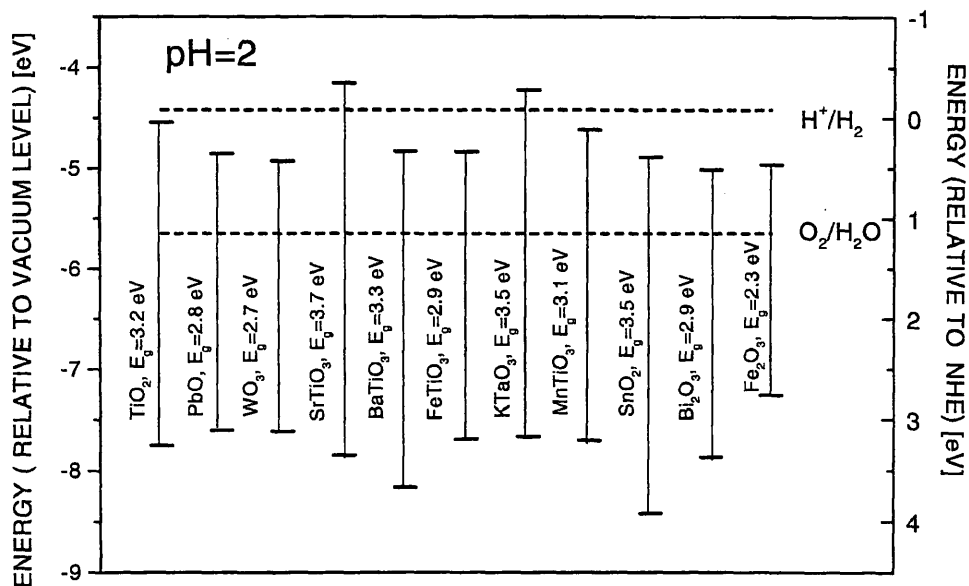
Figure 1.8 Band edge positions relative to the water red-ox potentials for several common oxide materials at pH 2.[11]

17

Well-researched metal-oxide materials for photoelectrochemical hydrogen production include TiO_2, $SrTiO_2$, WO_3, and more recently Fe_2O_3[11, 17, 18]. Fujishima and Honda first reported the use of TiO_2 for photoelectrochemical water splitting in 1972 [19]. This single n-type electrode cell became the ground-breaking research that photoelectrochemical hydrogen production is based on today. What is often not recognized with this work was the use of a chemical bias (due to pH differences between the counter and TiO_2 electrode) to overcome the band edge mismatch noted in Figure 1.8. Pioneering work done by Gratzel has shown that it is possible to increase the efficiencies of these oxide materials through a process called dye sensitization. Dye sensitized photoelectrochemical solar cells have shown efficiencies above 10% for electricity production, though this number is much lower when used for photolysis[20]. Other methods of improving the solar energy absorption of oxides include nano-structured materials, quantum confinement effects, catalyst impregnation, and chemically modified metal oxide materials[20]. It has been suggested that development of novel multi-component oxide semiconductors is necessary in order to find oxide systems with potential for water splitting devices[17].

1.5.2 Crystalline Inorganic Materials

As seen in Table 1.2, the highest solar-to-hydrogen conversion efficiencies to date in a single electrode unbiased PEC cell are only up to 1% for GaN[15, 21, 22]. Usually p-type single-crystal inorganic materials are examined for use as photocathodes for hydrogen production in PEC cells. Many of these materials have a band gap within the necessary range for efficient solar energy absorption but have a tendency to corrode in aqueous solution. $GaInP_2$[23], GaAs[24], InP[25], InGaN[26, 27], CdTe[28], and SiC[29] have also been

examined for this application. Many of these systems suffer from improper band edge positions that are too far negative, which prevents the completion of the oxidation half reaction for water splitting.

1.5.3 Hybrid and Tandem Materials

Monolithic tandem devices have achieved the highest reported efficiencies for PEC water splitting systems to date, with 12.4% solar-to-hydrogen conversion efficiency reported by Khasalev and Turner in 1998[13]. A tandem cell is comprised of a PEC layer on top of a PV junction, which provides internal bias to the system, adding additional energy to overcome non-ideal band edge alignment. This world record cell, shown in Figure 1.9, used an integrated photovoltaic device (a p-n GaAs layer) to voltage bias the interconnected p-$GaInP_2$ top layer, which was exposed to solution. Photons with an energy higher than the $GaInP_2$ top layer band gap (1.83eV) are absorbed, and those with lower energy pass through to the bottom GaAs absorber layer. The GaAs layer can absorb photons with as little energy as 1.42eV. The overall energetics can be seen in Figure 1.9[13]. The resulting process is a two photon/one electron mechanism. This type of monolithic device allows the mismatched energetics of the top layer to be compensated for by the voltage bias of the bottom layer. Top layer stability is still an important parameter in this system, which saw degradation after 20 hours under illumination and hydrogen production conditions. Other tandem materials for photoelectrochemical hydrogen production that have been investigated are Fe_2O_3/a-Si:Ge[30]. Tandem devices can give high efficiencies and the ability to overcome non-ideal band edge energetics for PEC systems. Drawbacks to such a device are the cost of fabrication and the need for a corrosion-resistant top layer.
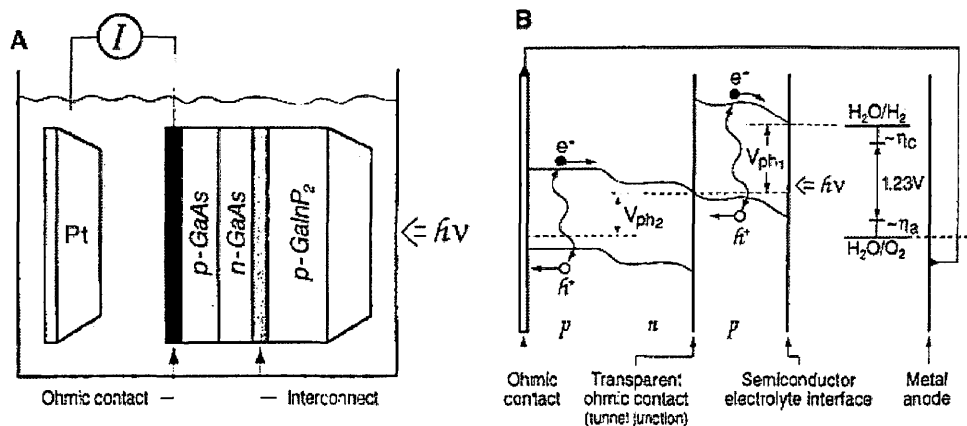
Figure 1.9 (a) A schematic of the 12.4% efficient tandem device (b) A band diagram and mechanism for the same device, showing the two photon, one electron process. [13]

1.5.4 Thin Films

Thin film semiconductor materials have diverse applications from solar energy conversion to microelectronics. Thin film photovoltaics are predicted to overtake other solar technologies due to their low-cost production and high efficiencies[31]. Thin films that have received a great deal of attention for PV applications include CdTe, CuInSe$_2$, and amorphous Si:H[31]. These thin film materials are characterized by high absorption coefficients, potential for manufacturing scale-up, and low-cost deposition possibilities. PEC devices using CIS-based thin films[32, 33], oxide thin films[34, 35], and SnN and InN thin films[36] have been investigated. Thin film materials are promising for PEC hydrogen production due to their high PV conversion efficiencies and their potential low cost.

20

1.6 Material Problems and Challenges / Reasons for Examining $CuInSe_2$

Material problems and challenges identified when looking for new PEC materials can be traced back to the criteria outlined in Section 1.4. Currently no single material exists that meets all three of the band gap, energetic, and corrosion requirements for a working system. Materials within the band gap range for high efficiency water splitting tend to be susceptible to corrosion. Stable, high band gap materials inefficiently absorb the solar spectrum. Both oxides and non-oxide materials show insufficient conduction or valence band positions, respectively. Material lifetime in systems that show optimum energetics is low. Many of the higher efficiency systems, such as tandem devices, are very expensive to fabricate, and thus pose additional problems with commercialization and large area fabrication.

For many of these reasons, the $CuInSe_2$ thin film alloy system is examined in this dissertation. These materials are already known to have high photovoltaic conversion efficiencies. As thin film materials, there are many potential low-cost deposition mechanisms. The $CuInSe_2$ alloy system can potentially be tailored to fit the needs of PEC energetic requirements through alloying. There exists an established framework for the study and synthesis of these materials for PV applications. The properties of the $CuInSe_2$ alloy system are detailed in the next section.

1.7 Review of CIS Materials

$CuInSe_2$-based (CIS) thin films materials are well researched for solid-state photovoltaic applications, and have also been studied as photoelectrochemical solar cells[37, 38]. CIS crystallizes with the chalcopyrite structure, whose unit cell structure is seen in Figure 1.10[39]. CIS is a direct gap semiconductor with a very high absorption coefficient for photons with energy higher than the band gap, on the order of $10^5 cm^{-1}$, making films as thin as $1\mu m$ functional in PV devices[31].
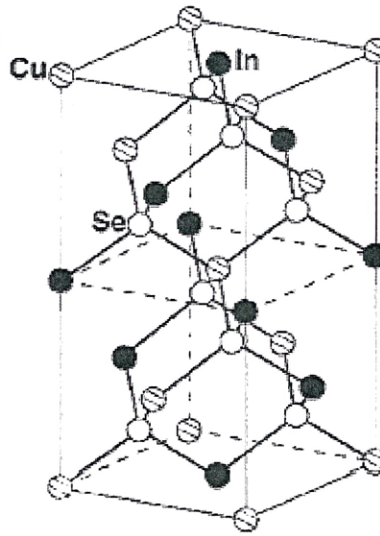
Figure 1.10 Chalcopyrite unit cell structure of $CuInSe_2$[39]

CIS is part of the $Cu-III-VI_2$ alloy system, where III = Al, Ga, In, and VI = S, Se. The alloy system has a large band gap range, with $CuInSe_2$ = 1.0eV, and

$CuGaS_2 = 2.54eV[40]$. These extensive energetics make CIS materials ideal candidates for study in PEC systems.

CIS and its alloys are most thoroughly studied for use in thin film solid-state solar cells. Typical solid state CIS photovoltaic devices consist of a conductive substrate, followed by a CIS or $Cu(In,Ga)Se_2$ (CIGS) layer, which is then coated with a buffer layer to form a heterojunction. This buffer layer is often CdS, however recent work eliminates the cadmium-containing layer and substitutes indium and zinc compounds[41, 42]. A transparent conducting oxide (TCO) window layer is used as a top contact before the cells are connected in a module. A schematic of the layers in a CIS PV cell is seen in Figure 1.11.
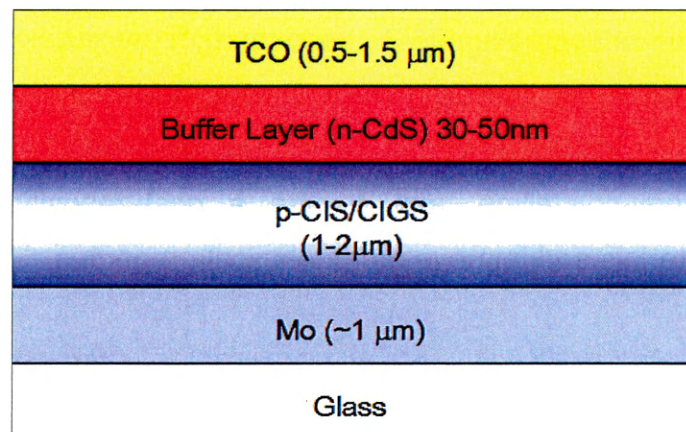
Figure 1.11 Layered structure of a CIS-based photovoltaic cell, where absorber layers as thin a 1um can efficiently absorb incoming radiation.

Many deposition routes for the synthesis of CIS materials have been reported, including vapor phase deposition[43], spray pyrolysis[44], selenization/sulfurization of metal precursors[31], and electrodeposition followed by annealing[45]. The most well developed synthetic route is a multi-stage vapor deposition process, which has been patented by NREL[46, 47]. The world record photovoltaic cell efficiency for CIS-based materials has reached over 19% for single small area CIGS cells[48] which where fabricated using the patented vapor deposition methods.

High efficiency materials have also been successfully made from electrodeposited precursors, showing efficiencies up to 15.4%[49]. These materials were made from electrodeposited $Cu(In,Ga)Se_2$ films which were then enriched and annealed in a vapor atmosphere to obtain stoichiometric films. Initial studies on the one-step electrodeposition of CIS thin films were performed by Bhattacharya over 20 years ago [50]. Since then, many studies have looked at the one-step deposition of $CuInSe_2$, $Cu(In,Ga)Se_2$, and their sulfur analogs for use in photovoltaic applications[45]. Electrodeposited materials are typically amorphous or semi-crystalline, and require a post-deposition treatment to crystallize the materials and improve morphological properties.

To date, there have been a handful of studies on CIS and CIGS systems for photoelectrochemical water splitting. $CuInSe_2$ thin films for water splitting have been studied in both modified and unmodified forms by Fernandez-Valverde et al.[51, 52]. They studied both electrodeposited and vapor deposited CIS films, modified with selenium and Ru coatings to prevent corrosion. In these studies, the CIS cells needed between 400-700mV cathodic bias for hydrogen production. It was found that photodegradation in the semiconductor occurs through the dissolution of In, which was suppressed in films with selenium and

Ru protective coatings. Work by Valderrama et al. [33] studied $Cu(In,Ga)Se_2$ thin films for hydrogen production. These films produced hydrogen at a bias of -400mV vs. SCE, and showed little compositional degradation over time. Martinez et al [53] studied the sulfide based film, $CuInS_2$, for hydrogen production, and found band edge positions too negative compared to the oxidation potential of water, though actual hydrogen production was not investigated. Evaporated $Cu(In,Ga)S_2$ analogs with band gaps in the range for water splitting again showed improper band edge positions[32]. These materials were coupled with a RuO_2 photoanode in a non-traditional multiple cell setup, where the CIGS films were used as solar cells to externally bias the photoanode. This setup has shown over 4% efficiency[54], however without a direct interface between the solution and the CIGS thin film this is not truly considered photoelectrochemical hydrogen production. To the knowledge of the author, there have been no studies concerning $CuGaSe_2$, $Cu(In,Ga)(Se,S)_2$, or tandem photoelectrodes using CIS materials for photoelectrochemical hydrogen production, nor any studies on the electrodeposition of $CuGaSe_2$ thin films.

1.8 Research Approach

The CIS alloy system, though ideal for PV applications, has several challenges for PEC water splitting. The first challenge addressed in this thesis is the low-cost synthesis of high band gap materials. To address this issue, these materials will be alloyed with gallium and sulfur in order to achieve band gaps that meet the criteria outlined above. In order to approach material synthesis via low cost methods, electrodeposited precursors are enriched in order to eliminate one or more steps in the multi-stage high vacuum process. Creating a less

intensive deposition method for the synthesis of these higher band gap materials is important in identifying a commercially viable system.

A way to empirically calculate the band gap for this alloy system had not yet been described when this research was initiated. This is an important tool in need of development to better understand the effect of alloying on the system energetics, useful in both PV and PEC applications.

Previous studies outlined above have shown that the band edges are too negative in some of the CIS materials relative to the water redox reactions, thus inhibiting the oxidation half reaction. Coupling this material to a bottom PV layer in a tandem device is one option for overcoming this challenge.

Finally, the electrodeposition of $CuGaSe_2$ thin films is examined. Multiple high temperature deposition steps can create fabrication issues when dealing with tandem cells, and a low-temperature ambient pressure technique for the synthesis of the top PEC layer could eliminate this problem. Electrodeposition provides a potential low cost mechanism for the fabrication of tandem CGS devices.

<u>References</u>

1. *Energy Information Administration Database.* 2006, US Department of Energy, www.eia.doe.gov.

2. IPCC, *Climate Change 2001: The Scientific Basis.* 2001, Intergovernmental Panel on Climate Change: Cambridge, UK. p. http://www.ipcc.ch/pub/wg1TARtechsum.pdf.

3. J.A. Turner, A Realizable Renewable Energy Future. *Science* **285**, p. 687-689 (1999).

4. U.S. Department of Energy, *Hydrogen Production: Natural Gas Reforming Fact Sheet.* 2006.

5. B. Suresh, *Chemical Economics Handbook*, in *Marketing Research Report: Hydrogen.* 2004, SRI Consulting.

6. M.Z. Jacobson, W.G. Colella, and D.M. Golden, Cleaning the Air and Improving Health with Hydrogen Fuel-Cell Vehicles. *Science* **308**, p. 1901-1905 (2005).

7. J.A. Turner, Sustainable Hydrogen Production. *Science* **305** (13 August 2004), p. 972-974 (2004).

8. A.J. Bard and M.A. Fox, Artificial Photosynthesis: Solar Splitting of Water to Hydrogen and Oxygen. *Accounts of Chemical Research* **28** (3), p. 141-145 (1995).

9. *Hydrogen, Fuel Cells & Infrastructure Technologies Program Multi-Year Research, Development and Demonstration Plan.* 2005, Department of Energy Office of Energy Efficiency and Renewable Energy.

10. A.J. Bard and L.R. Faulkner, <u>Electrochemical Methods: Fundamentals and Applications</u>. 2nd Edition ed. 2001: John Wiley and Sons.

11. T. Bak, J. Nowotny, M. Rekas, and C.C. Sorrell, Photo-Electrochemical Hydrogen Generation from Water Using Solar Energy: Materials-Related Aspects. *International Journal of Hydrogen Energy* **27**, p. 991-1022 (2002).

12. A.J. Nozik, Photoelectrochemistry: Applications to Solar Energy Conversion, *Annual Review of Physical Chemistry* **29**, p. 189-222 (1978)

13. O. Khasalev and J.A. Turner, A Monolithic Photovoltaic-Photoelectrochemical Device for Hydrogen Production Via Water Splitting. *Science* **280** (17 April 1998), p. 425-427 (1998).

14. M. Gratzel, Perspectives for Dye-Sensitized Nanocrystalline Solar Cells. *Progress in Photovoltaics: Research and Applications* **8**, p. 171-185 (2000).

15. S.S. Kocha, M.W. Peterson, D.J. Arent, J.M. Redwing, M.A. Tischler, and J.A. Turner, Electrochemical Investigation of the Gallium Nitride-Aqueous Electrolyte Interface. *Journal of the Electrochemical Society* **142** (12), p. L238-L240 (1995).

16. Y. Xu and M.A.A. Schoonen, The Absolute Energy Positions of Conduction and Valence Bands of Selected Semiconducting Minerals. *American Mineralogist* **85**, p. 543-556 (2000).

17. V.M. Aroutiounian, V.M. Arakelyan, and G.E. Shahnazaryan, Investigations of the Metal-Oxide Semiconductors Promising for Photoelectrochemical Conversion of Solar Energy. *Solar Energy Materials and Solar Cells* **89**(2-3), p. 153-163 (2005).

18. V.M. Aroutiounian, V.M. Arakelyan, and G.E. Shahnazaryan, Metal Oxide Photoelectrodes for Hydrogen Generation Using Solar Radiation-Driven Water Splitting. *Solar Energy* **78** (5), p. 581-592 (2005).

19. A. Fujishima and K. Honda, Electrochemical Photolysis of Water at a Semiconductor Electrode. *Science* **238**, p. 37-38 (1972).

20. M. Gratzel, Photoelectrochemical Cells. *Nature* **414**(15 November 2001), p. 338-344 (2001).

21. K. Fujii and K. Ohkawa, Photoelectrochemical Properties of P-Type GaN in Comparison with N-Type GaN. *Japanese Journal of Applied Physics, Part 2 (Letters)* **44** (28-32), p. L909-L911 (2005).

22. K. Fujii and K. Ohkawa, Bias-Assisted H_2 Gas Generation in HCl and KOH Solutions Using N-Type GaN Photoelectrode. *Journal of the Electrochemical Society* **153** (3), p. A468-A471 (2006).

23. O. Khaselev and J.A. Turner, Electrochemical Stability of P-GaInP$_2$ in Aqueous Electrolytes toward Photoelectrochemical Water Splitting. *Journal of the Electrochemical Society* **145**(10), p. 3335-3338 (1998).

24.   M.M. Khader, M.M. Hannout, and M.S. El-Dessouki, Catalytic Effects for Hydrogen Photogeneration Due to Metallic Deposition on P-GaAs. *International Journal of Hydrogen Energy* **21** (7), p. 547-553 (1996).

25.   A. Barkschat, H. Tributsch, and J.K. Dohrmann, Imaging of Catalytic Activity of Platinum on P-InP for Photocathodical Hydrogen Evolution. *Solar Energy Materials and Solar Cells* **80**(4), p. 391-403 (2003).

26.   J.D. Beach, *$In_xGa_{1-x}N$ for Photoelectrochemical Water Splitting*, PhD. Thesis in *Department of Physics*. 2001, Colorado School of Mines: Golden.

27.   K. Fujii, K. Kusakabe, and K. Ohkawa, Photoelectrochemical Properties of IngGaN for H_2 Generation from Aqueous Water. *Japanese Journal of Applied Physics, Part 1 (Regular Papers, Short Notes & Review Papers)* **44** (10), p. 7433-7435 (2005).

28.   X. Mathew, A. Bansal, J.A. Turner, R. Dhere, N.R. Mathews, and P.J. Sebastian, Photoelectrochemical Characterization of Surface Modified CdTe for Hydrogen Production. *Journal of New Materials for Electrochemical Systems* **5** (2), p. 149-154 (2002).

29.   P.J. Sebastian, N.R. Mathewsa, X. Mathew, M. Pattabi, and J. Turner, Photoelectrochemical Characterization of SiC [Hydrogen Production Applications]. *International Journal of Hydrogen Energy* **26** (2), p. 123-125 (2001).

30.   E.L. Miller, R.E. Rocheleau, and S. Khan, A Hybrid Multijunction Photoelectrode for Hydrogen Production Fabricated with Amorphous Silicon/Germanium and Iron Oxide Thin Films. *International Journal of Hydrogen Energy* **29** (9), p. 907-914 (2004).

31.   N.G. Dhere and R.G. Dhere, Thin-Film Photovoltaics. *Journal of Vacuum Science & Technology A (Vacuum, Surfaces, and Films* **23** (4), p. 1208-1214 (2005).

32.   A.M. Fernandez, N. Dheree, J.A. Turner, A.M. Martinez, L.G. Arriaga, and U. Cano, Photoelectrochemical Characterization of the $Cu(In,Ga)S_2$ Thin Film Prepared by Evaporation. *Solar Energy Materials and Solar Cells* **85**(2), p. 251-259 (2005).

33.	R.C. Valderrama, P.J. Sebastian, J.P. Enriquez, and S.A. Gamboa, Photoelectrochemical Characterization of CIGS Thin Films for Hydrogen Production. *Solar Energy Materials and Solar Cells* **88** (2), p. 145-155 (2005).

34.	Y.S. Chaudhary, A. Agrawal, R. Shrivastav, V.R. Satsangi, and S. Dass, A Study on the Photoelectrochemical Properties of Copper Oxide Thin Films. *International Journal of Hydrogen Energy* **29** (2), p. 131-134 (2004).

35.	S. Ichikawa and R. Doi, Photoelectrocatalytic Hydrogen Production from Water on Transparent Thin Film Titania of Different Crystal Structures and Quantum Efficiency Characteristics. *Thin Solid Films* **292** (1-2), p. 130-134 (1997).

36.	T. Lindgren, M. Larsson, and S.E. Lindquist, Photoelectrochemical Characterisation of Indium Nitride and Tin Nitride in Aqueous Solution. *Solar Energy Materials and Solar Cells* **73** (4), p. 377-389 (2002).

37.	D. Cahen, G. Dagen, G. Hodes, Y. Mirovsky, Y.W. Chen, J.C.W. Folmer, P.J. Ireland, R. Noufi, J.A. Turner, K.J. Bachmann, S. Endo, C. Rincon, G.A. Sawatzky, and M. Tomkiewicz, n-Cu-In-Chalcogenide-Based Photoelectrochemical Cells. *Progress in Crystal Growth and Characterization* **10**, p. 263-270 (1984).

38.	G. Dagan, S. Endo, G. Hodes, G. Sawatzky, and D. Cahen, Ternary Chalcogenide-Based Photoelectrochemical Cells. III: n-$CuIn_5S_8$/Aqueous Polysulfide. *Solar Energy Materials* **11** (1-2), p. 57-74 (1984).

39.	S.B. Zhang, S.H. Wei, A. Zunger, and H. Katayama-Yoshida, Defect Physics of the $CuInSe_2$ Chalcopyrite Semiconductor. *Physical Review B* **57** (16), p. 9642-9656 (1998).

40.	O. Madelung, M. Schulz, and H. Weiss, eds. Physics of Ternary Compounds. Numerical Data and Functional Relationships in Science and Technology, Vol. 17; Semiconductors. 1985, Springer-Verlag: Berlin.

41.	A. Ennaoui, Chemical Bath Process for Highly Efficient Cd-Free Chalcopyrite Thin-Film-Based Solar Cells. *Canadian Journal of Physics* **77**(9), p. 723-729 (1999).

42. R.N. Bhattacharya, M.A. Contreras, and G. Teeter, 18.5% Copper Indium Gallium Diselenide (CIGS) Device Using Single-Layer, Chemical-Bath-Deposited Zns(O,OH). *Japanese Journal of Applied Physics, Part 2 (Letters)* **43**(11B), p. L1475-L1476 (2004).

43. H.W. Schock, Thin Film Photovoltaics. *Applied Surface Science* **92**, p. 606-616 (1996).

44. M.E. Beck and M. Cocivera, Thin-Film Copper Indium Diselenide Prepared by Selenization of Copper Indium Oxide Formed by Spray Pyrolysis. *Thin Solid Films* **272** (1), p. 71-82 (1996).

45. D. Lincot, J.F. Guillemoles, S. Taunier, D. Guimard, J. Sicx-Kurdi, A. Chaumont, O. Roussel, O. Ramdani, C. Hubert, J.P. Fauvarque, N. Bodereau, L. Parissi, P. Panheleux, P. Fanouillere, N. Naghavi, P.P. Grand, M. Benfarah, P. Mogensen, and O. Kerrec, Chalcopyrite Thin Film Solar Cells by Electrodeposition. *Solar Energy* **77**(6), p. 725-737 (2004).

46. D.S.C. Albin, J. J.;Tuttle, J. R.;Contreras, M. A.;Gabor, A. M.;Noufi, R.;Tennant, A. L., *Recrystallization Method to Selenization of Thin-Film Cu(In,Ga)Se$_2$ for Semiconductor Device Applications.*, U.S. Patent, 1995, Midwest Research Institute, Kansas City, Missouri: U.S.

47. R.G. Noufi, A. M.;Tuttle, J. R.;Tennant, A. L.;Contreras, M. A.;Albin, D. S.;Carapella, J. J., *Method of Fabricating High-Efficiency Cu(In,Ga)(Se,S)$_2$ Thin Films for Solar Cells*, U.S. Patent, 1995, Midwest Research Institute, Kansas City, Missouri: U.S.

48. M.A. Green, K. Emery, D.L. King, S. Igari, and W. Warta, Solar Cell Efficiency Tables (Version 26). *Progress in Photovoltaics: Research and Applications* **13** (5), p. 387-392 (2005).

49. R.N. Bhattacharya and A.M. Fernandez, CuIn$_{1-x}$Ga$_x$Se$_2$-Based Photovoltaic Cells from Electrodeposited Precursor Films. *Solar Energy Materials & Solar Cells* **76**, p. 331-337 (2003).

50. R.N. Bhattacharya, Solution Growth and Electrodeposited CuInSe$_2$ Thin Films. *Journal of the Electrochemical Society* **130**(10), p. 2040-2042 (1983).

51. A.L. Alanis, J.R.V. Garcia, R. Rivera, and S.M.F. Valverde, Protective Rhutenium Thin Films on CuInSe$_2$ for Hydrogen Evolution in Acidic Media. *International Journal of Hydrogen Energy* **27**(2), p. 143-147 (2002).

52. S. FernandezValverde, E. OrdonezRegil, R. ValenciaAlvarado, R. RiveraNoriega, and O. SolorzaFeria, Mass Spectrometry Quantification of Hydrogen Produced under Illumination of P-CuInSe$_2$ and Modified Surfaces. *International Journal of Hydrogen Energy* **22** (6), p. 581-584 (1997).

53. A.M. Martinez, L.G. Arriaga, A.M. Fernandez, and U. Cano, Band Edges Determination of CuInS$_2$ Thin Films Prepared by Electrodeposition. *Materials Chemistry and Physics* **88** (2-3), p. 417-420 (2004).

54. N.G. Dhere and A.H. Jahagirdar, Photoelectrochemical Water Splitting for Hydrogen Production Using Combination of CIGS Solar Cell and RuO$_2$ Photocatalyst. *Thin Solid Films* **480-481**, p. 462-465 (2005).

CHAPTER 2

ENRICHMENT SCHEMES FOR Cu(In,Ga)(Se,S)$_2$ THIN FILMS

FROM ELECTRODEPOSITED PRECURSORS

2.1 Abstract

CuInSe$_2$-based materials have the potential to meet the band gap requirements for the photoelectrochemical splitting of water. Alloying these materials with gallium and sulfur can increase band gap values into the desired range for this application. Electrodeposition of these thin film materials can meet low-cost, large area requirements, though the addition of sulfur and large amounts of gallium has proven extremely difficult using this method. In this work, Cu(In,Ga)Se$_2$ precursors are prepared via electrodeposition, and then compositionally adjusted to obtain further incorporation of sulfur and in some instances gallium. The effect of the solution concentration of the metal salts on electrodeposited precursor film composition was examined, and films with preferred stoichiometry were synthesized. X-ray diffraction patterns of the precursor films showed broad diffraction peaks, with 2θ values centered around several of the main CIGS peaks. SEM images revealed nanocrystalline morphology, which agrees with the observed XRD line-broadening. Physical vapor deposition post-treatment using several enrichment atmospheres was investigated as a method for forming crystalline materials with the desired composition for water splitting. A selenium vapor overpressure was found to be necessary to avoid film degradation during annealing. Films enriched in a gallium atmosphere showed phase separation, with two chalcopyrite alloy phases present.

33

2.2 Introduction

With a band gap of 1.04eV and excellent solar energy conversion characteristics, $CuInSe_2$ (CIS) thin films are of significant interest in photovoltaic research. Gallium is commonly added to these chalcopyrite materials forming $Cu(In,Ga)Se_2$, increasing the band gap and resulting in better photovoltaic performance in films with a compositional gradient[1]. Solid solutions of these chalcopyrite materials with sulfur can form $Cu(In,Ga)(Se,S)_2$ with a band gap between 1.04 – 2.43eV[2]. This range of energetics offers a unique system in which the band gap can be engineered to fit the specific requirements of either a photovoltaic or photoelectrochemical device. Materials for photoelectrochemical hydrogen production require a band gap optimally between 1.7-2.0eV[3].

CIS-based materials have been deposited via many reported methods, including physical vapor deposition[4, 5], selenization and sulfurization of metallic precursors[4], spray pyrolysis[6], and electrodeposition[7]. Materials realizing the highest efficiencies in this system are prepared via vapor deposition processes, requiring high vacuum conditions. The most common method of preparation for high-efficiency PV cells is a three-step physical vapor deposition process developed and patented by NREL. The process involves the evaporation of three sequential layers of differing composition, following by cooling in a selenium atmosphere[8, 9].

Electrodeposition of CIS thin films can potentially fulfill the low-cost, large-area manufacturing requirements for a photoelectrochemical hydrogen production system. Previous work documents solar cells prepared from physical vapor deposition (PVD) enrichment of electrodeposited CIS and $Cu(In,Ga)Se_2$ precursor materials with efficiencies up to 15.4%[10]. Sulfurization of the surface

of these photovoltaic absorbers has been reported as a means to boost cell performance without affecting the longer wavelength absorption [11]. For the application of photoelectrochemical water splitting, it is desirable to incorporate sulfur and gallium throughout the film to obtain a homogeneous material with a higher band gap throughout the bulk.

The electrodeposition process proceeds via electrochemical reductions in solution onto a conducting substrate. For the electrodeposition of Cu-In-Ga-Se precursors, the reactions in Equations (2.1) through (2.4) represent the conversion from aqueous ionic precursors to a solid film.

$$Cu^{2+} + 2e^- \Leftrightarrow Cu \qquad E^0 = +0.342V \quad (vs.NHE) \tag{2.1}$$

$$In^{3+} + 3e^- \Leftrightarrow In \qquad E^0 = -0.338V \quad (vs.NHE) \tag{2.2}$$

$$Ga^{3+} + 3e^- \Leftrightarrow Ga \qquad E^0 = -0.549V \quad (vs.NHE) \tag{2.3}$$

$$H_2SeO_3 + 4e^- + 4H^+ \Leftrightarrow Se + 3H_2O \qquad E^0 = +0.739V \quad (vs.NHE) \tag{2.4}$$
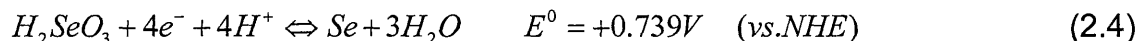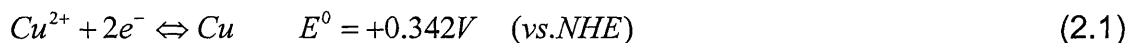
Electrodeposition results in amorphous or semi-crystalline materials, which can be crystallized through an additional annealing step. During the annealing process, it is possible to adjust the film composition by enrichment in an atmosphere of the desired elements. During physical vapor deposition (PVD), an evaporated element or compound for the enrichment process arrives at the substrate or precursor surface where it condenses. The amount of condensation depends on the vapor pressure of the compound and the condensation and re-evaporation rates at the substrate [12]. Condensation of an evaporated layer is followed by the reaction of the condensate with the precursor material to obtain the final film.

The benefit of enriching already prepared compounds over complete vapor deposition is the possibility of eliminating one or more of the steps in the overall deposition cycle. This also reduces the need for ultra-high vacuum, thus cutting down on fabrication time and energy intensity. Here, the electrodeposition of precursor materials, and the subsequent enrichment to obtain the desired final film properties is examined. In this study, Cu-In-Ga-Se thin film precursors were electrodeposited and then enriched with gallium and sulfur to obtain high band gap alloys. The electrodeposition parameters and resulting material properties are examined.

2.3 Experimental Methods

$Cu(In,Ga)(Se,S)_2$ semiconductor thin films were prepared using the multi-step process shown in Figure 2.1. Precursors were prepared by electrodeposition, then the materials were enriched and annealed in a PVD chamber, where several enrichment schemes were examined. Finally, the prepared films were characterized to examine morphology and composition.
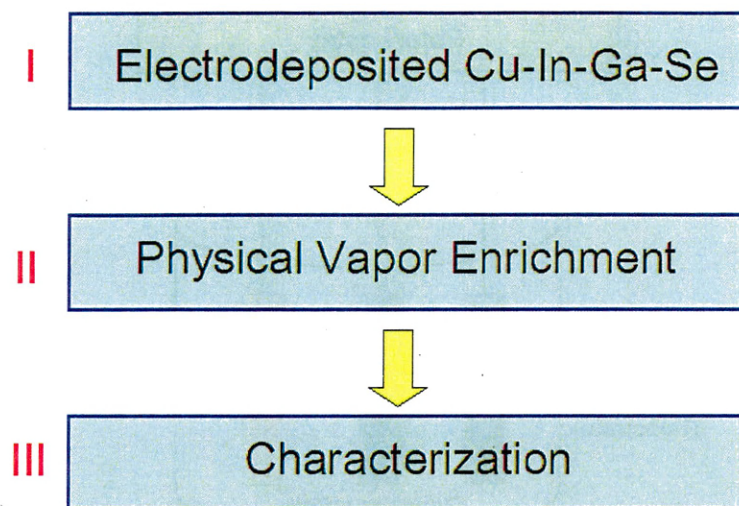
Figure 2.1 Steps in the preparation of $Cu(In,Ga)(Se,S)_2$ materials starting with electrodeposited precursors. These precursors were then enriched via physical vapor deposition and then characterized.

2.3.1 Electrodeposition

Thin film Cu-In-Ga-Se precursors were electrodeposited from aqueous solution onto molybdenum-coated glass working electrodes. $CuCl_2$, $InCl_3$, $GaCl_3$, and H_2SeO_3 (all reagent-grade) were dissolved in varying concentrations in pH 3 Hydrion buffer with LiCl as a supporting electrolyte. All depositions were performed unstirred, at -1.0V vs. a Pt mesh reference with a Pt counter electrode, using a Princeton Applied Research Model 273A potentiostat. Figure 2.2 shows a three electrode electrodeposition set up. Table 2.1 shows several deposition bath concentrations that were examined. The films formed in this step were used as the precursors for further compositional adjustment through a vapor deposition step.
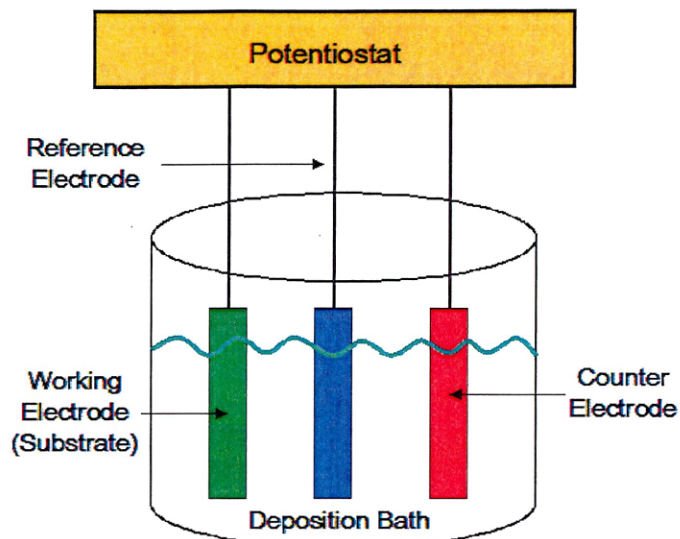
Figure 2.2 A three-electrode electrodeposition set-up.

2.3.2 Physical Vapor Deposition

The electrodeposited precursor films were separated into several batches for processing. The materials were annealed for 1 hour at 450°C in a vacuum of roughly 10^{-5} Torr, and enriched via PVD. Three different vapor deposition atmospheres were examined: a) S powder and In shot; b) In_2S_3 and Se shot; or c)In_2S_3, Ga_2S_3, and Se shot. These compounds were placed in individual heated boats in the vacuum system. The precursor films were horizontally mounted at the top of the vacuum chamber about 25 cm from the evaporation source, and the boats were heated to 450°C to evaporate the compounds into the system atmosphere. After one hour of deposition, the films were held in the vacuum chamber atmosphere until cooled.

2.3.3 Characterization

Precursor compositions were determined via inductively coupled plasma (ICP) analysis with a Varian-Liberty spectrometer. Samples for ICP analysis were prepared by dissolving 1 cm^2 films in aqua regia, then diluting to 25mL with 18MΩ purity deionized water. Electron-probe microanalysis (EPMA) was done at both 10 and 20 keV accelerating voltages, using a JEOL WD/ED combined microanalyzer. The same instrument was used to obtain SEM images at a 20 keV accelerating voltage. Auger electron spectroscopy (AES) survey scans and depth profiles were done at 5.0 keV with a Physical Electronics PHI 670 Auger instrument. X-ray diffraction (XRD) patterns of the precursor and final films were obtained using a Scintag XGEN diffractometer with a Cu Kα anode source.

2.4.1 Electrodeposition and Composition of Precursors

The effect of varying copper concentration in solution on the overall as-deposited film composition was studied. Three different copper concentrations were examined, with two sets of replicate baths. The resulting average film compositions normalized to copper are given in Table 2.1.

Table 2.1 Bath compositions in moles/L, and resulting average precursor film compositions normalized to copper.

Bath	$[CuCl_2]$ (M)	$[InCl_3]$ (M)	$[GaCl_3]$ (M)	$[H_2SeO_3]$ (M)	Film Composition
1	0.0046	0.0050	0.0057	0.0078	$CuIn_{0.68}Ga_{0.23}Se_{2.1}$
2	0.0056	0.0050	0.0057	0.0078	$CuIn_{0.62}Ga_{0.20}Se_{1.78}$
3	0.0056	0.0050	0.0057	0.0078	$CuIn_{0.57}Ga_{0.16}Se_{1.64}$
4	0.0067	0.0050	0.0057	0.0078	$CuIn_{0.56}Ga_{0.09}Se_{1.34}$
5	0.0067	0.0050	0.0057	0.0078	$CuIn_{0.53}Ga_{0.14}Se_{1.41}$

Higher copper concentration in solution resulted in greater copper content in the film, as expected. There is an inverse relationship between solution copper concentration and the amount of selenium electrodeposited in the precursor films, as seen in Figure 2.3. This phenomenon can be explained by the mechanism of film formation. It has been proposed in $CuInSe_2$ electrodeposition [13] that the mechanism of film formation is dependent on the ratio of the fluxes of selenium to copper (α) arriving at the surface of the electrode during deposition. In situations where this ratio of flux is less than 1, i.e. where more copper is arriving at the electrode surface than selenium, the film formation involves intermediates of Cu_2Se and Cu, shown in Equation (2.5). These intermediates then react with indium in solution, forming the $CuInSe_2$ ternary compound at more negative potentials, containing an excess of either Cu_2Se or Cu, depending on the reaction parameters.

$$Cu^{2+} + \alpha Se^{4+} + (2+4\alpha)e^- \rightarrow \alpha Cu_2Se + (1-2\alpha)Cu \qquad (2.5)$$
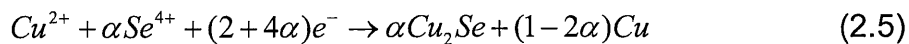
Since gallium and indium both have largely negative potentials relative to the copper reduction seen in Equations (2.2) and (2.3), it can be inferred that in the case of $Cu(In,Ga)Se_2$ electrodeposition the initial formation of Cu and Cu_2Se

holds true. Thus, as the amount of copper in solution is increased, the flux ratio (α) decreases, and this second copper-rich phase of either Cu or Cu_2Se is formed. The excess copper phase in the film was then analyzed by ICP, showing a higher copper concentration in the film than what is expected for pure $Cu(In,Ga)Se_2$. The overall film composition is reported normalized to copper, and the relative amount of selenium decreases with increasing copper concentration. Neither Cu nor Cu_2Se are observed in the diffraction patterns of the precursor materials, shown in Figure 2.4b, however the amount may be small, or the phase may be amorphous.
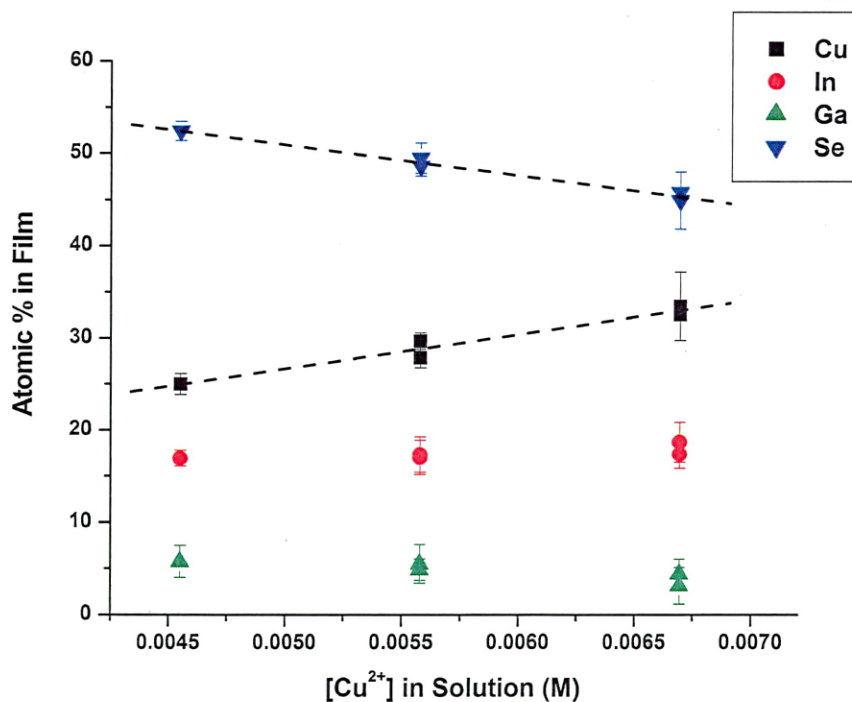
Figure 2.3. Effect of copper concentration in solution on the average film composition of precursor materials as determined by ICP. Error bars show standard deviation.

Changing the concentration of copper in the deposition solution had no statistical affect on the indium and gallium compositions of the precursors. If the formation mechanism proceeds as previously outlined, then the formation of CIGS is limited by the initial amount of Cu and Cu_2Se formed. As long as the gallium and indium concentrations in solution are adequate or in excess there will be no observed concentration effect on the final film concentration of these compounds. Although the initial electrodeposition solutions contained more gallium than indium, the films contained less gallium than indium due to more negative reduction potential of gallium. The deposition with the highest Se/Cu ratio in solution (~ 1.7) showed an average film composition closest to the desired stoichiometry of $Cu(In,Ga)Se_2$.

The reproducibility of these depositions was studied using consecutive depositions from the same bath, as well as depositions using two different electrodeposition baths with the same concentrations. It was seen that depositions from the same bath resulted in relatively similar compositions when done consecutively, showing that the concentration of the deposition solutions is high enough to not undergo significant depletion during electrodeposition. However, when solutions sat overnight or for extended lengths of time, the film compositions will vary from the previous depositions. Change in pH or oxidation due to air or dissolved oxygen exposure may contribute to change in solution composition, affecting the consistent deposition of films over time from the same bath. Comparing the average values of film composition from separate baths, it was seen that they differ slightly, possibly due to fluctuations in actual concentration due to error in metal salt weighing, or slight differences in substrate size, position, or placement in the deposition cell which can affect the deposition current and diffusion of ions from the solution to the electrode.

2.4.2 Precursor Microstructure

The electrodeposited precursor films have nanocrystalline morphology, seen in SEM images showing polycrystalline material with grain sizes under 100nm. (Figure 2.4a). All precursor films in this study showed XRD patterns with broad peaks around the key CIGS-based peaks (Figure 2.4b). Peak broadening attests to the presence of very small crystal domains in these materials. The thickness of the precursor films ranged from ~1.5 - 3 µm, determined from cross-sectional SEM images. Several of the films exhibited a cracked morphology, likely due to the generation of hydrogen gas bubbles from water reduction at the electrode surface during the electrodeposition.
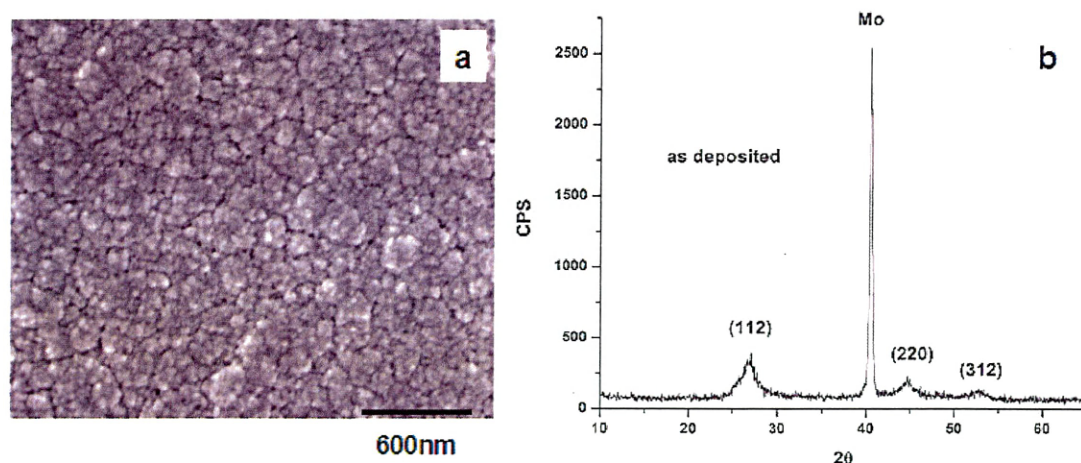
Figure 2.4. a. SEM of electrodeposited CIGS precursor film showing nanocrystalline morphology. b. XRD pattern showing broad CIGS peaks.

2.4.3 Film Enrichment and Annealing

Films formed during the electrodeposition step served as the precursors films in this phase of the study. Precursor films were separated into batches and then treated in vapor atmospheres of: a) S powder and In shot; b)In_2S_3 and Se shot; or c) In_2S_3, Ga_2S_3 and Se shot. Table 2.2 shows the average film composition resulting from each PVD atmosphere. The data reported here are average film compositions taken from 10 and 20keV EPMA analysis (unless otherwise indicated), with film compositions normalized to copper. All precursor materials showed sulfur incorporation after each of the PVD processes.

Films formed from enrichment in batch (a) showed a gain in sulfur, but a great loss in the selenium content, resulting in poor electronic properties. The thermal decomposition of $CuInSe_2$ has been shown to begin with an outgassing of Se_2 vapor[14]. This illustrates the necessity of a selenium overpressure for high temperature processing of these films to eliminate decomposition of the precursor material and corresponding loss of selenium. Due to the poor quality of the films generated in this approach, this method was abandoned and an enrichment atmosphere was selected that would prevent selenium outgassing. Batch (b) showed indium and sulfur enrichment, with selenium maintained in the film, while batch (c) showed enrichment in gallium and sulfur, and again selenium was maintained in the film. These procedures produced films with the general formula of $CuIn_mGa_nSe_xS_y$.

Table 2.2 Average film compositions of precursor and processed materials, obtained from ICP and EPMA, respectively. Overall composition is normalized to copper.

Batch	Cu (%)	In (%)	Ga (%)	Se (%)	S (%)	Film Composition
Prec*	27.83± 1.1	17.29± 1.9	5.46± 2.1	49.41± 1.7	0	$CuIn_{0.62}Ga_{0.20}Se_{1.78}$
a	15.19± 5.3	32.77± 3.8	1.23±0.2	2.15± 1.1	48.66± 2.6	$CuIn_{2.16}Ga_{0.08}Se_{0.14}S_{3.20}$
b	22.87± 4.2	25.67± 2.4	2.45± 1.2	29.97± 2.6	19.04± 1.9	$CuIn_{1.12}Ga_{0.11}Se_{1.31}S_{0.83}$
c	21.56± 3.1	8.95± 3.5	19.93± 1.8	29.51± 1.8	20.05± 1.3	$CuIn_{0.42}Ga_{0.92}Se_{1.37}S_{0.93}$

*Precursor compositions obtained by ICP analysis

2.4.4 Enriched Film Structure and Morphology

After the physical vapor deposition enrichment of the precursor films, the crystallinity of the films improved. Figure 2.5 shows typical microstructure from the processed films processed in batch (b) showing larger grain sizes.

The XRD patterns for these films also show evidence of the increased crystallinity after annealing, and much sharper peaks are observed , as shown in Figures 2.6 and 2.7. Many of the enriched materials show multiple chalcopyrite phases, evidenced by split diffraction peaks, an effect notably pronounced in films processed in batch (c).

600nm
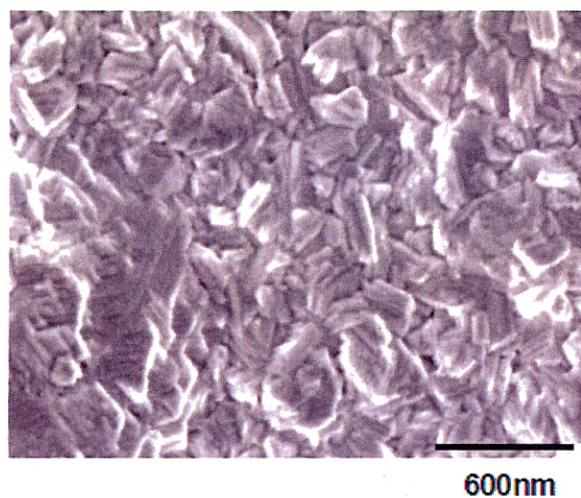
Figure 2.5. SEM micrograph of a CIGSS film prepared by physical vapor enrichment of electrodeposited precursor films, showing increased grain size after the vapor enrichment process.

XRD is a useful tool for examining this alloy system. The CIS system forms homogeneous alloys with gallium and sulfur, forming $Cu(In,Ga)(Se,S)_2$, where gallium substitutes for indium and sulfur for selenium in the $CuInSe_2$ lattice. Because the structure remains the same, the diffraction peaks for these alloy materials are characterized by peak positions that are shifted due to the change in lattice constant owing to the size differences of the alloyed element. This makes identification of the presence of the alloy material versus that of another crystal phase easy to distinguish through comparison with standard $CuInSe_2$ and the other ternary chalcopyrite peaks.

Figure 2.6a shows a typical XRD pattern from materials processed in batch (b), with the main CIS-based peaks observed. Figure 2.6b shows an enlarged area of the diffraction pattern around 27° 2θ, where the main (112) CIS

peak is observed. The standard peak positions for $CuInSe_2$ and $CuInS_2$ are shown, and it is seen that this peak lies between these two positions, indicating alloying between these phases, or overlapping separate peaks, which is evidenced by the broad structure. As sulfur is alloyed into $CuInSe_2$, the lattice constant decreases, shifting 2θ to larger values.
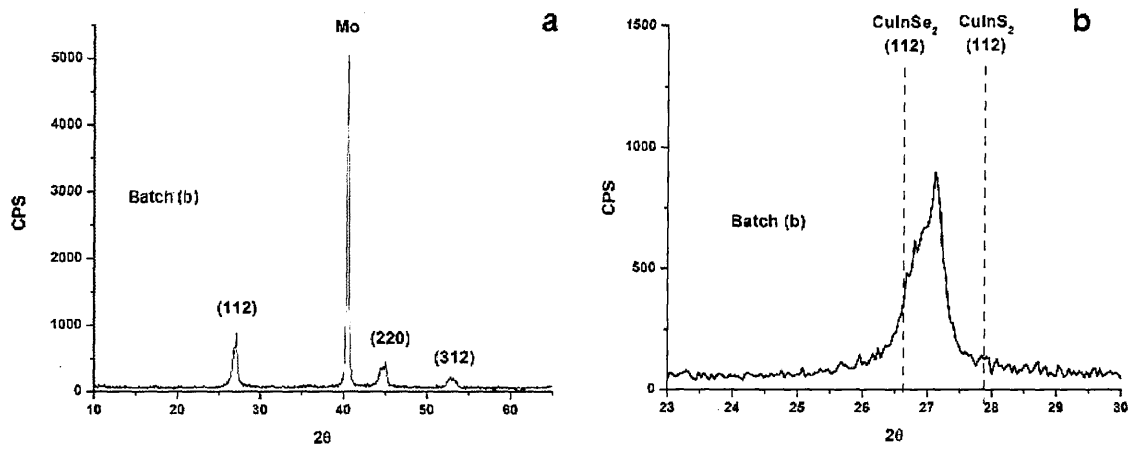
Figure 2.6 a. An XRD pattern of a CIGSS film processed in batch (b). **b.** An enlarged portion of the diffraction pattern showing broad peaks with dashed lines showing reference peak positions for $CuInSe_2$ and $CuInS_2$.

Figure 2.7a shows a typical diffraction pattern from materials processed in batch (c). The same CIS peaks are observed, however, peak splitting is more obvious. Figure 2.7b shows an enlarged area of the diffraction pattern around 27° 2θ. The reference peak positions for $CuInSe_2$ and $CuGaS_2$ are shown. Both gallium and sulfur decrease lattice constants, shifting peaks to higher values. The split peaks are evidence of multiple phases within the material. These peaks

suggest the existence of one phase containing a higher gallium and sulfur content.
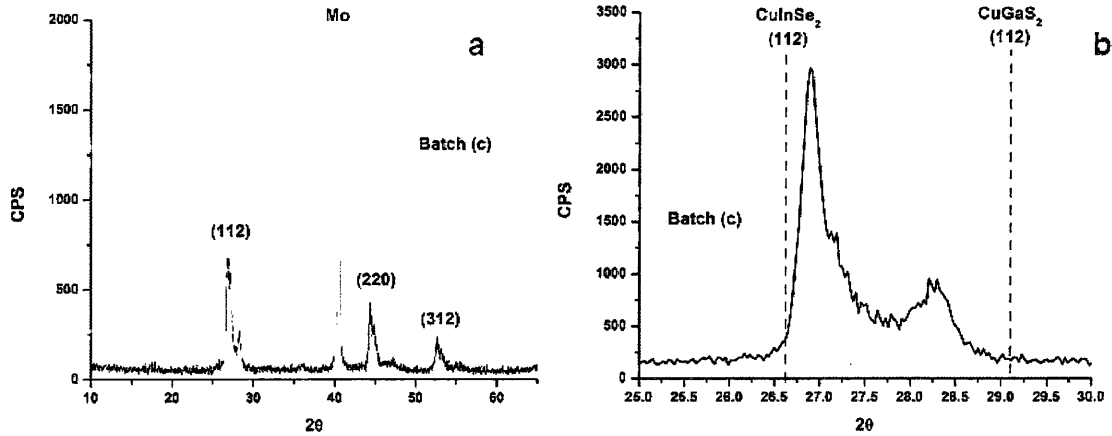
Figure 2.7. a. The XRD pattern of a CIGSS film processed in batch (c) showing a split peak pattern. b. An enlarged portion of the pattern from 25 - 30 degrees 2θ with dashed lines showing reference peak positions for $CuInSe_2$ and $CuGaSe_2$.

2.4.5 Depth Profiles

All of the films enriched via PVD were 2.5 to 3.0 microns thick, as determined from SEM cross sectional micrographs (not shown). The overall thickness of the films increased after annealing in the PVD atmosphere due to condensation of additional compounds on the precursor during enrichment. Oxygen can be seen in the bulk of films from both batches prepared in this study. The initial electrodeposited film likely contained mixed oxides as a result of electrodeposition in an aqueous environment. It is possible that the annealing temperature was not high enough to remove all oxygen from the films, or the

annealing time long enough for sulfur or selenium to completely replace the oxygen. From the AES depth profiles, it appears as though the gallium in the films is associated with this oxide phase, though no XPS measurements were performed to verify this hypothesis. However, band gap measurements on these samples, which were performed in Chapter 3, show the existence of a low band gap CIS phase in batch (b), which coincides to no gallium in the CIS structure. This is evidence that the gallium may be associated with oxygen in the precursor films, and this oxide takes higher temperatures or longer reaction times to be converted to a CIS alloy. Indium oxide is present at the very surface of all films due to air and moisture exposure, and is a desired coating that is hypothesized to protect materials from corrosion in solution [15].

The enrichment process, as seen in the depth profile in Figure 2.8 and Figure 2.9, affected the top 1 to 1.5 microns of the film. Atmosphere (b) caused an indium rich surface layer, whereas atmosphere (c) produced a gallium rich surface layer. Sulfur is seen in higher concentration in the top portion of all films, and then tails off into the bulk of the material suggesting sulfur incorporation is a diffusion limited process. From the depth profiles it can be seen that sulfur substitutes for selenium into the amorphous material, and during annealing forms a crystalline, sulfurized high band gap layer. If this reaction is taken as an equilibrium reaction between selenium and sulfur vapor, the following equilibrium equation given in Equation (2.6) is obtained. The rate at which sulfurization takes place will then depend on the relative ratios of Se_2 and S_2 in the vapor phase, the following interdiffusion of the sulfurized layers, and the overall time and temperature of reaction.

$$CuInSe_2 + S_2 \Leftrightarrow CuInS_2 + Se_2 \qquad (2.6)$$
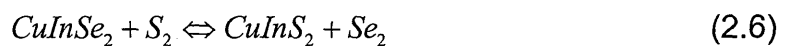
A typical AES depth profile of a material annealed in batch (b) is shown in Figure 2.8. During PVD, the evaporated compounds condense on the substrate, forming a layer of additional material on the precursor surface. In_2S_3 is commonly used as a buffer layer in $Cu(In,Ga)Se_2$ (CIGS) photovoltaic preparation, and the interdiffusion between this layer and CIGS has been studied[16, 17]. During the physical vapor deposition of In_2S_3, the thermal decomposition of the compound is thought to occur via Equation (2.7), resulting in several indium-sulfur vapor compounds, which will be referred to as In_xS_y, as well as S_2 vapor[16].

$$In_2S_3 \rightarrow In_xS_y(g) + S_2(g) \qquad (2.7)$$
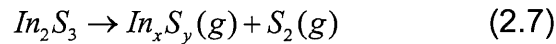
Large amounts of copper diffusion into this deposited buffer layer have been reported, with copper depletion on the CIGS side of the interface. Copper ions show a much higher mobility than indium ions, and this copper interdiffusion is seen to increase with temperature, though this phenomenon has only been studied up to $240°C$[17]. Since these In_xS_y compounds are non-stoichiometric, they have a high density of vacancies within their crystal structure. Diffusion in In_xS_y is thought to occur through the vacancies in the crystal structure that can be occupied by copper atoms, as well as the replacement of indium sites by Cu[16]. Indium is also shown to diffuse from the buffer layer into the CIGS structure, and theorized to occur by occupation of copper vacancies in the CIGS. This diffusion is apparent in the samples annealed in batch (b). In this atmosphere, an In_xS_y surface layer was deposited on the precursor Cu-In-Ga-Se during the PVD process. Indium from this surface layer diffused into the CIGS precursor, causing an enrichment of indium in a diffusion limited fashion from the interface. Copper from the precursor layer is seen to diffuse into the condensed In_xS_y, resulting in

the formation of the CIS compound at the surface. With the maintained selenium overpressure, the resulting layers were selenized, and $Cu(In,Ga)(Se,S)_2$ was formed as the top layer.

The diffusion of gallium in the precursor material toward the Mo/precursor interface was observed, where the gallium atomic percent is close to 10%. The diffusion of gallium toward the back contact in CIGS materials is well-known. One possible reason for this segregation is the difference in the surface free energies of $CuInSe_2$ and $CuGaSe_2$. Another possibility is the reported difference in the reaction rates of these compounds during annealing, with $CuInSe_2$ forming more rapidly at high temperatures[18]. As $CuInSe_2$ forms at the surface during the PVD enrichment, the gallium is preferentially segregated to the back of the material. The structure of the film resembles more of a layered, $CuIn(Se,S)_2/Cu(In,Ga)Se_2$.
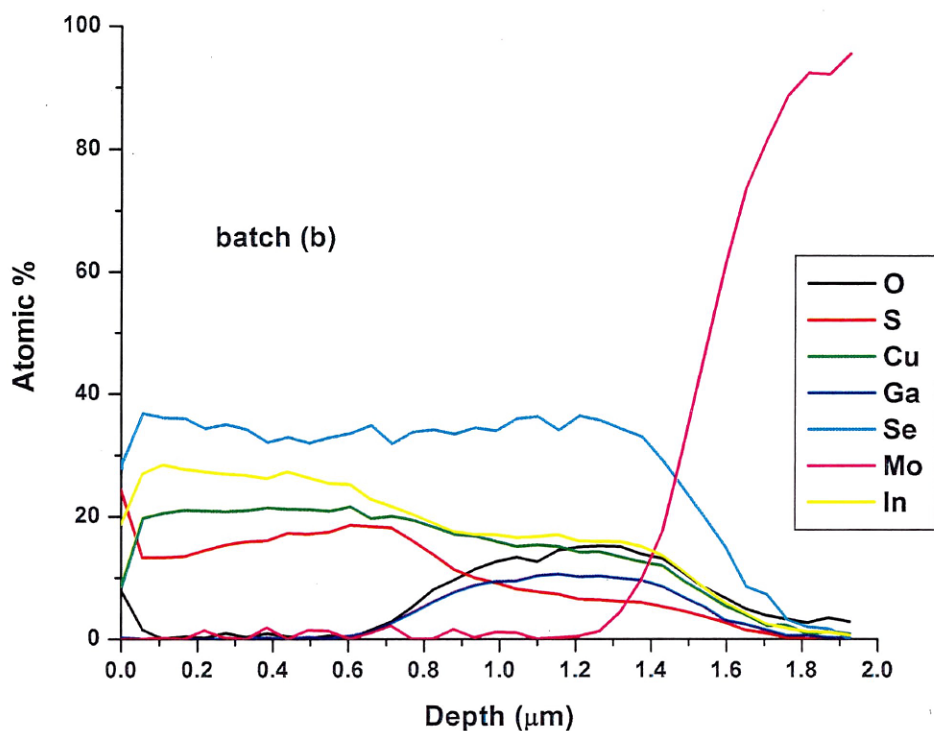
Figure 2.8 An AES depth profile of a CIGS precursor film annealed in batch (b), showing a low gallium content surface layer of CuIn(Se,S)$_2$.

In materials processed in batch (c) which contained both the indium and gallium compounds, the selective condensation of gallium versus indium is observed. Ga$_2$S$_3$ also undergoes a vapor decomposition at high temperatures[19], as seen in Equation (2.8).

$$Ga_2S_3 \rightarrow Ga_xS_y(g) + S_2(g) \qquad (2.8)$$
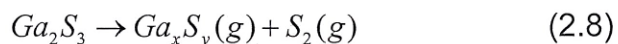
The selective condensation of gallium may indicate the vapor pressure of the gallium compounds is higher than that of the indium compounds, resulting in

a gallium-rich atmosphere during enrichment. Another possibility is that gallium has a higher sticking coefficient to the substrate. Assuming a similar mechanism of diffusion in Ga_xS_y, copper is seen to diffuse into the condensed layer, which is then selenized to form $Cu(In,Ga)(Se,S)_2$. The top layer composition is vastly different from the bottom bulk of the film, and the film composition can be approximated more readily as $CuGa(Se,S)_2/Cu(In,Ga)Se_2$. Peak splitting is pronounced in these films, indicating there are multiple phases present.
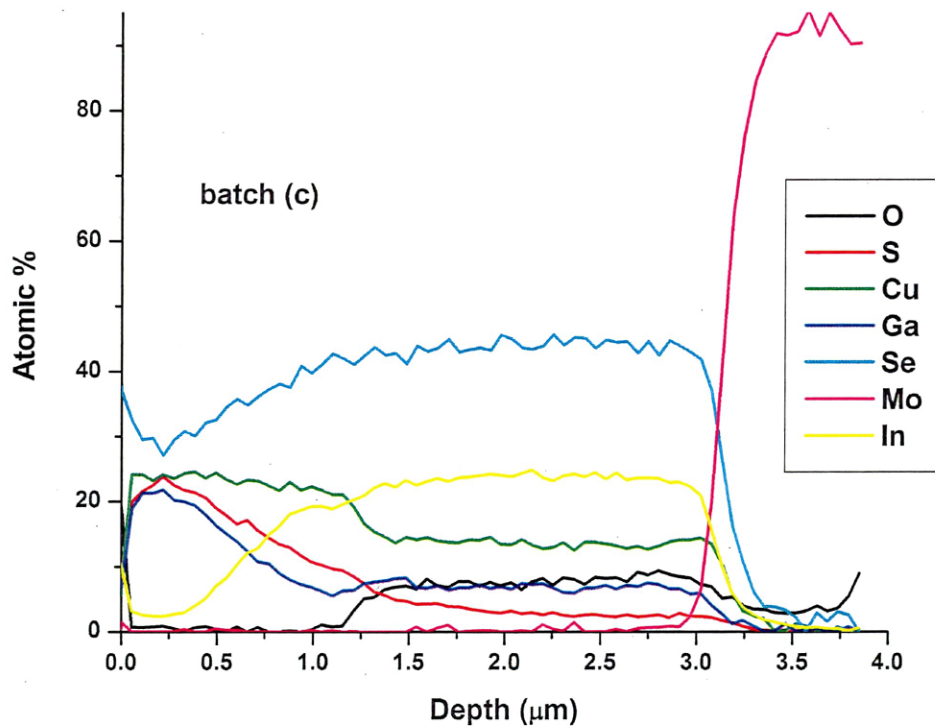
Figure 2.9 AES depth profile of a film processed in batch C, showing sulfur diffusion into the film.

2.4.6 Preliminary Electronic Properties

Initial photoconductivity type can be determined by illumination of the semiconductor in buffer solution. Those materials processed in a selenium atmosphere (both batches (b) and (c)) showed p-type photocurrent in preliminary light tests, while those from batch (a) showed very poor photoresponse. The films in batch (a) have no crystalline structure due to elemental loss of selenium and non-stoichiometry resulting from the annealing process. The films enriched in the gallium-containing atmosphere showed larger band gaps than the samples annealed without Ga_2S_3, which is detailed in Chapter 3. This corresponds with the known increase in band gap with the inclusion of gallium into the CIS system. The electronic properties of these materials are further discussed in Chapter 3.

2.5 Conclusions and Future Work

The composition of electrodeposited $Cu(In,Ga)Se_2$ thin films can be regulated by the relative copper and selenium flux in solution, though is independent of the indium and gallium solution concentrations when in excess. Maintaining a Cu/Se ratio in solution less than about 2 leads to the formation of precursors with a stoichiometry close to the preferred value of $Cu(In,Ga)Se_2$. Stoichiometric electrodeposited precursor materials show a small grain size, and broad CIGS diffraction peaks are evident in XRD patterns.

A selenium overpressure is essential for processing of these materials to maintain structural and electronic integrity. Without selenium, annealing caused elemental loss of Se_2 and film degradation. In films enriched and annealed in an

atmosphere containing selenium, the crystal size increased, and sharper XRD peaks corresponding to CIS alloys are observed.

Physical vapor deposition in an In_2S_3/Se atmosphere caused the formation of a sulfur containing CIS-based alloy thin film. Enrichment in an atmosphere containing In_2S_3/Ga_2S_3/Se caused the preferential deposition of a gallium-rich layer. The deposition of a top layer compositionally mismatched to the precursor resulted in the creation of two different material phases, evidenced by peak splitting in XRD patterns. It may be possible to homogenously alloy these phases with longer annealing times or higher annealing temperatures. The mechanism of alloying proceeds via diffusion at the condensed PVD layer/precursor interface.

It is recommended that Ga_2S_3 with a selenium overpressure be used to process these materials in order to obtain high gallium content thin films, and thus band gaps in the PEC water splitting range. Precursor films with higher gallium content will be necessary to avoid phase segregation. Longer processing times and higher substrate temperatures may allow greater diffusion in enriched materials, making it possible to obtain alloyed films without phase separation. Slow diffusion can limit the amount of homogeneity obtained via this process, and thinner precursor films are suggested. In fact, films as thin as 1μm can be used for high efficiency absorbers with this material group.

The advantage of this synthesis process using electrodeposited precursor films is the elimination of one or more steps during high vacuum deposition. Eliminating one or more source compounds will lead to a lower intensity deposition process. This process can potentially be used to fabricate materials in the CIS-family with higher band gaps suitable for photoelectrochemical hydrogen production, as well as other applications. Compositional grading in these

materials can be obtained through physical vapor enrichment, which can be a useful material property for increasing efficiencies in both PV and PEC devices.

REFERENCES

1. M.A. Contreras, J. Tuttle, A. Gabor, A. Tennant, K. Ramanathan, S. Asher, A. Franz, J. Keane, L. Wang, and R. Noufi, High Efficiency Graded Bandgap Thin-Film Polycrystalline Cu(In,Ga)Se$_2$-Based Solar Cells. *Solar Energy Materials and Solar Cells* **41-42**, p. 231-246 (1996).

2. O. Madelung, M. Schulz, and H. Weiss, eds. Physics of Ternary Compounds. Numerical Data and Functional Relationships in Science and Technology, Vol. 17; Semiconductors. 1985, Springer-Verlag: Berlin.

3. T. Bak, J. Nowotny, M. Rekas, and C.C. Sorrell, Photo-Electrochemical Hydrogen Generation from Water Using Solar Energy. Materials-Related Aspects. *International Journal of Hydrogen Energy* **27**, p. 991-1022 (2002).

4. N.G. Dhere and R.G. Dhere, Thin-Film Photovoltaics. *Journal of Vacuum Science & Technology A (Vacuum, Surfaces, and Films)* **23** (4), p. 1208-1214 (2005).

5. M. Gossla and W.N. Shafarman, Five-Source PVD for the Deposition of Cu(In,Ga)(Se,S)$_2$ Absorber Layers. *Thin Solid Films* **480-481**, p. 33-36 (2005).

6. S. Shirakata, Y. Kannaka, H. Hasegawa, T. Kariya, and S. Isomura, Properties of Cu(In,Ga)Se$_2$ Thin Films Prepared by Chemical Spray Pyrolysis. *Japanese Journal of Applied Physics Part 1-Regular Papers Short Notes & Review Papers* **38** (9A), p. 4997-5002 (1999).

7. D. Lincot, J.F. Guillemoles, S. Taunier, D. Guimard, J. Sicx-Kurdi, A. Chaumont, O. Roussel, O. Ramdani, C. Hubert, J.P. Fauvarque, N. Bodereau, L. Parissi, P. Panheleux, P. Fanouillere, N. Naghavi, P.P. Grand, M. Benfarah, P. Mogensen, and O. Kerrec, Chalcopyrite Thin Film Solar Cells by Electrodeposition. *Solar Energy* **77** (6), p. 725-737 (2004).

8. D.S.C. Albin, J. J.;Tuttle, J. R.;Contreras, M. A.;Gabor, A. M.;Noufi, R.;Tennant, A. L., *Recrystallization Method to Selenization of Thin-Film Cu(In,Ga)Se$_2$ for Semiconductor Device Applications.*, U.S., Editor. 1995, Midwest Research Institute, Kansas City, Missouri: U.S.

9. R.G. Noufi, A. M.;Tuttle, J. R.;Tennant, A. L.;Contreras, M. A.;Albin, D. S.;Carapella, J. J., *Method of Fabricating High-Efficiency Cu(in,Ga)(Ses)2 Thin Films for Solar Cells*, U.S., Editor. 1995, Midwest Research Institute, Kansas City, Missouri: U.S.

10. R.N. Bhattacharya, Hiltner, J.F., Batchelor, W., Contreras, M., Noufi, R.N., Sites, J.R., 15.4% $CuIn_{1-x}Ga_xSe_2$-Based Photovoltaic Cells from Solution-Based Precursor Films. *Thin Solid Films* **361-362**, p. 396-399 (2000).

11. T. Nakada, H. Ohbo, T. Watanabe, H. Nakazawa, M. Matsui, and A. Kunioka, Improved $Cu(in,Ga)(S,Se)_2$ Thin Film Solar Cells by Surface Sulfurization. *Solar Energy Materials & Solar Cells* **49**, p. 285-290 (1997).

12. J.E. Mahan, <u>Physical Vapor Deposition of Thin Films</u>. 2000: John Wiley & Sons.

13. L. Thouin, S. Massaccesi, S. Sanchez, and J. Vedel, Formation of Copper Indium Diselenide by Electrodeposition. *Journal of Electroanalytical Chemistry* **374** (1-2), p. 81-88 (1994).

14. M. Ruckh, J. Kessler, T.A. Oberacker, and H.W. Schock, Thermal-Decomposition of Ternary Chalcopyrite Thin-Films. *Japanese Journal of Applied Physics Part 1-Regular Papers Short Notes & Review Papers* **32**, p. 65-67 (1993).

15. C.A. Koval, R.L. Austermann, J.A. Turner, and B.A. Parkinson, The Effects of Surface Energetics and Surface Oxide Layers on the Cyclic Voltammetry of Metallocenes at Nonilluminated P-InP Electrodes. *Journal of the Electrochemical Society* **132** (3), p. 613-623 (1985).

16. D. Abou-Ras, G. Kostorz, A. Strohm, H.W. Schock, and A.N. Tiwari, Interfacial Layer Formations between $Cu(In,Ga)Se_2$ and In_xS_Y Layers. *Journal of Applied Physics* **98** (12), p. 123512-1-123512-123512-7 (2005).

17. D. Abou-Ras, D. Rudmann, G. Kostorz, S. Spiering, M. Powalla, and A.N. Tiwari, Microstructural and Chemical Studies of Interfaces between $Cu(In,Ga)Se_2$ and In_2S_3 Layers. *Journal of Applied Physics* **97** (8), p. 84908-1-84908-84908-8 (2005).

18. M. Marudachalam, R.W. Birkmire, H. Hichri, J.M. Schultz, A. Swartzlander, and M.M. AlJassim, Phases, Morphology, and Diffusion in

$CuIn_xGa_{1-x}Se_2$ Thin Films. *Journal of Applied Physics* **82** (6), p. 2896-2905 (1997).

19.   C.Y. Jones and J.G. Edwards, Observation of a Phase Transformation of Ga_2S_3 in a Quartz Effusion Cell above 1230 K by Means of Neutron Scattering. *Journal of Physical Chemistry B* **105** (14), p. 2718-2724 (2001).

CHAPTER 3

BAND GAP AND BAND EDGE ENGINEERING
IN THE CU(IN,GA)(SE,S)₂ ALLOY SYSTEM

3.1 Abstract

The Cu(In,Ga)(Se,S)₂ alloy system allows the synthesis of homogeneous semiconductor materials with a band gap range of 1.0 to 2.4eV. This material system spans the required band gap for photoelectrochemical water splitting, which is between 1.7 and 2.1eV. Semiconductor alloy theory permits the prediction of the band gap of a binary alloy system based on the band gaps and bowing parameters of the original materials. In this chapter, this theory has been expanded for the Cu(In,Ga)(Se,S)₂ pentenary system, and an equation is developed to describe the band gap for this alloy based on the amount of gallium and sulfur. Experimental Cu(In,Ga)(Se,S)₂ materials were prepared from physical vapor enrichment of electrodeposited precursor films, as outlined in Chapter 2. The developed alloy equation was then applied to Auger depth profiles of these compositionally graded films to show the compositional dependence of the band gap throughout the depth of the material. The band gaps of these materials were then determined using photocurrent spectroscopy. Results exhibit multiple band gap values, resulting from compositional inhomogeneity. The higher band gap value is in the range of desired band gaps for application in photoelectrochemical hydrogen production. The experimental values closely matched values calculated using the developed empirical equation, providing a way to predict the optical

material properties from material composition using the alloy equation developed here.

3.2 Introduction

With a direct band gap of approximately 1.0eV, CuInSe$_2$ (CIS) thin films have been extensively examined for photovoltaic applications. CIS is part of a family of Cu-III-VI$_2$ chalcopyrite materials, which encompasses alloys with VI = S, Se and Te, and III = Al, Ga, and In. These alloys possess diverse energetics: CuGaS$_2$, for example, is a chalcopyrite semiconductor with a band gap of 2.43eV[1]. Alloying this material with CIS to form Cu(In,Ga)(Se,S)$_2$ (CIGSS), can yield a material with tunable properties, enabling a band gap range of 1.0 to 2.43eV, yet maintaining a homogeneous system. Materials within this band gap range have diverse applications, including photoelectrochemical hydrogen production, which requires a semiconductor with a band gap between 1.7 to 2.0 eV[2].

Cu(In,Ga)Se$_2$ materials have realized photovoltaic efficiencies greater than 19%[3]. One strategy for increasing the photovoltaic performance and efficiencies in these compound semiconductors is by engineering the electronic properties through band gap grading. Band gap grading involves intentionally tailoring the band gap by varying the alloy composition as a function of depth in the material. This compositional gradient affects the conduction band and/or valence band positions[4]. Graded band positions are used to create electric fields within the semiconductor that can contribute to overall device performance. Typically, this grading is done with gallium in CuInSe$_2$, forming Cu(In,Ga)Se$_2$, which is known to shift the conduction band minimum toward vacuum (negative)

by lowering the electron affinity[5]. Two types of grading in CIS are typically employed, termed "normal" and "notch". A "normal" profile involves a higher band gap layer near the back contact(Figure 3.1a). This profiling is achieved by increasing the conduction band energy toward the back contact through gallium incorporation. A conduction band energy decrease towards the interface pushes electrons toward the surface of the material and inhibits recombination at the back contact, creating a back surface field (BSF)[6]. The second type of grading, the "notch" structure, has a higher band gap region at the film surface, with "normal" profiling toward the back contact[7](Figure 3.1b). "Notch" profiling enables a higher open circuit voltage due to the larger band gap at the surface, and can be optimized to the solar spectrum for maximum efficiency. The back portion of the film serves the purpose as the "normal" grading cell outlined above, creating a BSF effect.
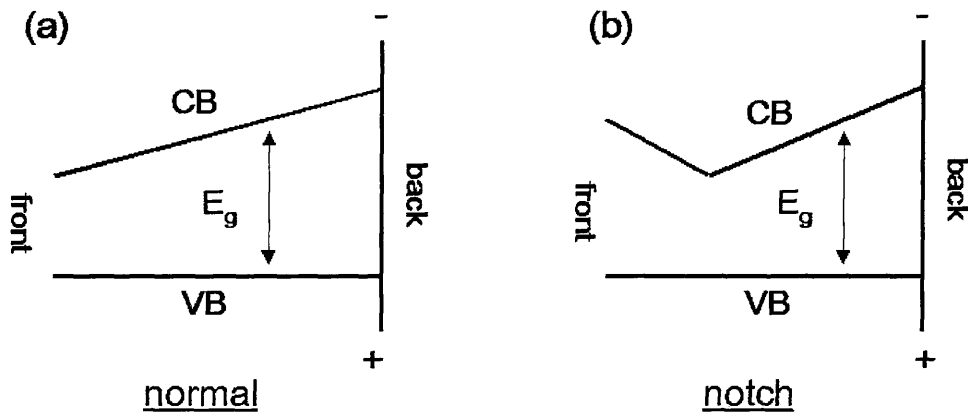
Figure 3.1 (a) A "normal" graded band gap structure for p-CIGS photovoltaic devices, showing the conduction band (CB) increase toward the back of the device obtained through gallium grading (b) A "notch" grading structure, with an increase in gallium toward the front and back contacts.

The CIS alloy system is a promising candidate for meeting several system criteria for PEC water splitting through the engineering of material energetics and corrosion characteristics. To date, band gap grading has not been applied to any PEC systems, however, band gap grading in photoelectrochemical cells could serve at least two functions. The first is an increase in device performance and efficiency, similar to that for PV devices, by creating internal electric fields to enhance charge separation. The second function serves to change the band edge positions at the interface. The proper energetic positioning of the band edges is essential for obtaining a system that performs both the water oxidation and reduction reactions. Grading in the CIS alloy system also includes the possibility of added corrosion resistance from one or more of the alloyed elements.

In this chapter, compositionally graded $Cu(In,Ga)(Se,S)_2$ (CIGSS) thin film materials are addressed. These films were prepared from electrodeposited $Cu_nIn_mGa_zSe_y$ precursors that were enriched via physical vapor deposition (PVD) to incorporate sulfur and gallium to increase the band gap. Details regarding film synthesis and characterization are given in Chapter 2. An empirical equation describing the band gap of CIGSS as a function of composition has been independently developed based on semiconductor alloy theory. This is then applied to show band gap grading throughout the bulk of the prepared films, and is correlated to electrochemical measurements, confirming energetic predictions. Calculation of the band gap throughout the depth of the film is an important tool for predicting the properties of graded band gap materials, with applications in both photovoltaics and photoelectrochemistry.

3.3 Alloy Theory

An grading equation, slightly different from that obtained by Bar, et al [8], was developed from binary alloy theory for application in the CIGSS system. For a basic semiconductor alloy of two materials, $A_{1-x}B_x$, the varying concentration of x changes the optical properties of the material. Semiconductor alloy theory uses Equation (3.1) to predict the band gap (E_g) of the new alloy material, where b is known as the optical bowing coefficient.

$$E_g(A_{1-x}B_x) = (1-x)E_g(A) + xE_g(B) - bx(1-x) \tag{3.1}$$

The optical bowing coefficient (b) corrects for non-linearity in the change in lattice parameters as the material is alloyed. These parameters can be determined experimentally through band gap measurements on a series of alloys, or theoretically through computation. Figure 3.2 shows the values used for the bowing coefficients between each solid solution, as well as the endpoint band gaps, obtained from published experimental data[1, 9].

The alloy of interest, $Cu(In_{1-x}Ga_x)(Se_{1-y}S_y)_2$, can be simplified to $Cu(A_{1-x}B_x)(C_{1-y}D_y)_2$ in order to apply alloy theory. A predictive equation to calculate the band gap (E_g) of the alloy was derived through the following steps, shown in Equations (3.2) -(3.5) . Table 3.1 shows the abbreviated representation of the intermediate materials in the equation.

$$E_g(Cu(A_{1-x}B_x)(C_{1-y}D_y)_2) = (1-y)E_g(CuA_{1-x}B_xC_2)$$
$$+yE_g(CuA_{1-x}B_xD_2)+by(1-y)$$

$$(3.2)$$

$$E_g(CuA_{1-x}B_xC_2) = (1-x)E_g(CuAC_2)+xE_g(CuBC_2)-b'x(1-x)$$

$$(3.3)$$

$$E_g(CuA_{1-x}B_xD_2) = (1-x)E_g(CuAD_2)+xE_g(CuBD_2)-b''x(1-x))$$

$$(3.4)$$

$$E_g(Cu(A_{1-x}B_x)(C_{1-y}D_y)_2) =$$
$$(1-y)\{(1-x)E_g(CuAC_2)+xE_g(CuBC_2)-b'x(1-x)\}$$
$$+y\{(1-x)E_g(CuAD_2)+xE_g(CuBD_2)-b''x(1-x))\}-by(1-y)$$

$$(3.5)$$
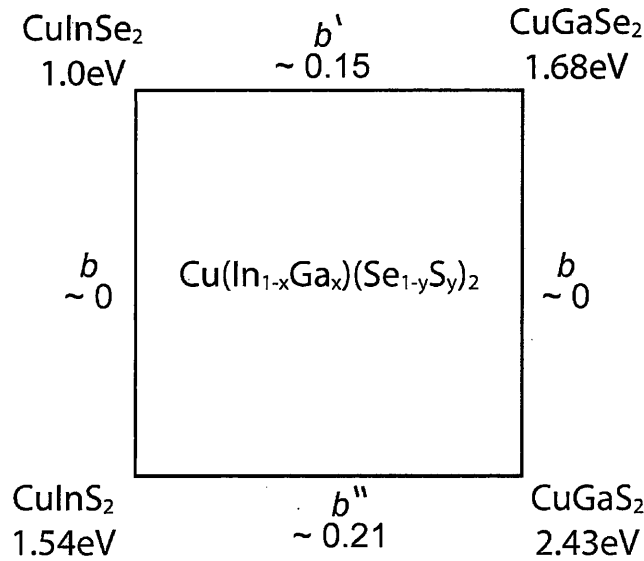
Figure 3.2 End points and bowing coefficients in the Cu(In,Ga)(Se,S)$_2$ system[9]

Table 3.1 Equation representation of each alloy in Equations 3.2 - 3.5.

Representation	Cu-III-VI$_2$
CuAC$_2$	CuInSe$_2$
CuAD$_2$	CuInS$_2$
CuBC$_2$	CuGaSe$_2$
CuBD$_2$	CuGaS$_2$
CuABC$_2$	Cu(In,Ga)Se$_2$
CuABD$_2$	Cu(In,Ga)S$_2$

Substituting the endpoint band gaps and experimental bowing coefficients shown in Figure 3.2 into Equation (3.5), the empirical equation relating the band gap to the gallium and sulfur ratios within the material is seen in Equation (3.6).

$$E_g(Cu(In_{1-x}Ga_x)(Se_{1-y}S_y)_2 = 1.00 + 0.53x + 0.54y + .15xy + .15x^2 + 0.06x^2y \qquad (3.6)$$

By inputting x and y into this equation, the band gap of a $Cu(In_{1-x}Ga_x)(Se_{1-y}S_y)_2$ alloy can be predicted from experimentally determined gallium and sulfur ratios. Analogously, one can start with a desired semiconductor band gap range, and use this equation to determine the amounts of gallium and/or sulfur needed in the structure. Figure 3.3 shows a three-dimensional representation of possible gallium and sulfur alloy concentrations that give rise to band gaps in the range of 1.7-2.1eV, suitable for water splitting applications. A large range of possible alloy compositions can give rise to the same band gap. This composition range can have effects on corrosion and

energetic properties of a PEC system. Different amounts of gallium or sulfur in the material could lead to differing corrosion characteristics between two films with the same band gap. In this same way, differing compositions can give rise to materials with altered band edge positions, providing a way to tailor the surface energetics in a material with a specific band gap.
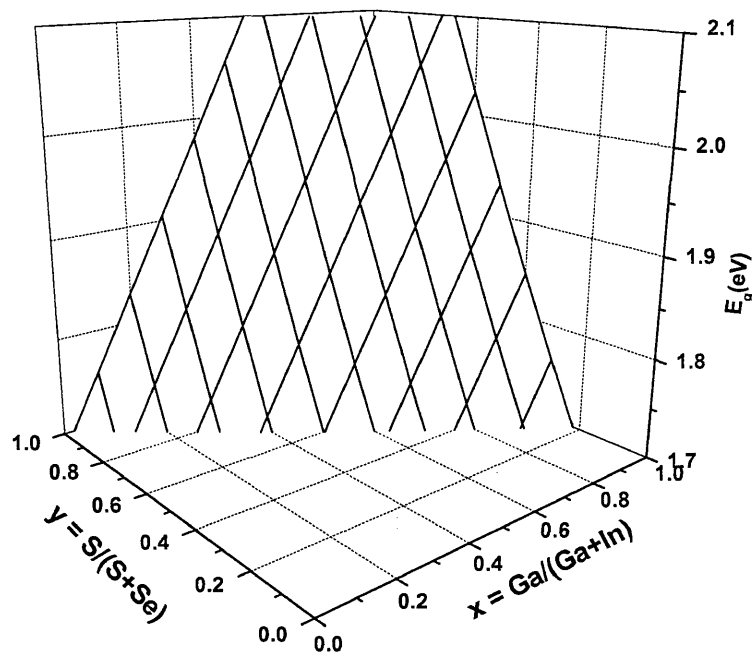
Figure 3.3 Three dimensional representation of possible alloy compositions giving rise to thin films in the band gap range of 1.7 - 2.1eV.

3.4 Experimental

The materials for this study were prepared using a two step process: electrodeposition of Cu-In-Ga-Se precursor films from aqueous metal salt

solutions onto molybdenum coated glass substrates, followed by enrichment via physical vapor deposition (PVD) in a combined In_2S_3, Ga_2S_3, and Se atmosphere. This synthesis process and the resulting film composition and morphology are detailed in Chapter 2.

Electrodes were prepared using roughly $1cm^2$ square sections of the final materials. A small section of the film was removed from the substrate, and contact to the Mo substrate was made using silver paint and copper wire. The edges were then insulated with non-conducting epoxy, and the electrodes were baked at 80°C for 1 hour to cure the epoxy. This insulation left only the surface of the electrode in contact with solution. Figure 3.4 depicts the electrode preparation.

Auger electron spectroscopy (AES) survey scans and depth profiles were done at 5.0 keV using a Physical Electronics PHI 670 Auger instrument. Preliminary photoresponse measurements were performed by measuring the photovoltage shift (either negative or positive) under high intensity illumination in a two-electrode electrochemical cell, using a Pt counter electrode in an aqueous buffer solution. Current-voltage characteristics of these materials were examined using a Princeton 263A potentiostat, in both dark and full spectrum light at one sun illumination ($100mW/cm^2$) from a 150W tungsten source.
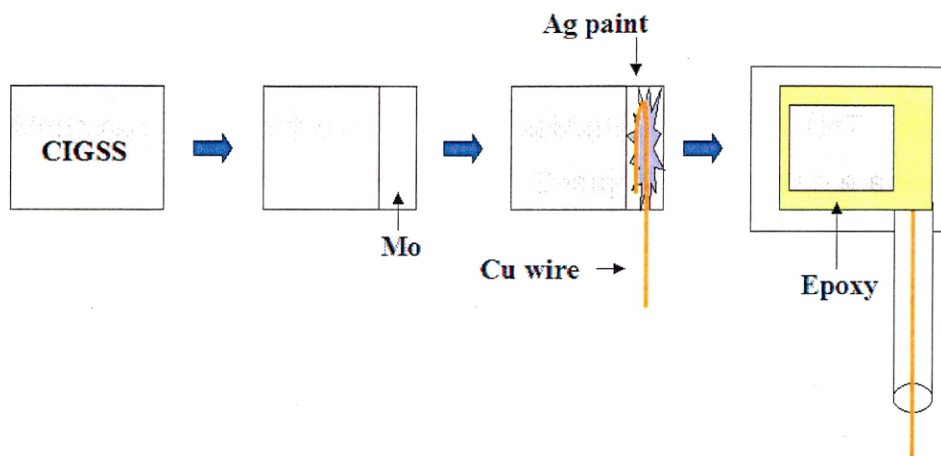
Figure 3.4 Schematic showing the preparation of electrodes for electrochemical measurements.

Material band gaps were determined using photocurrent spectroscopy, as previously described[10]. A three-electrode cell with a Pt counter electrode and a saturated calomel electrode (SCE) reference was used in an aqueous solution of 0.1M Na_2SO_3 in pH 10 buffer. A Princeton Technology 101 monochromator was used to step through wavelengths from a 100W tungsten illumination source. Two photoresponse curves were collected for each material, as the low and high band gaps observed could not be measured on the same scan. Lamp spectra for normalization were obtained using a thermopile with a low-noise amplifier and an appropriate color filter to eliminate second-order interference in the data collection. A Princeton 263A potentiostat and Stanford SR830 lock-in amplifier interfaced with a computer were used to register the photocurrent response as a function of wavelength.

3.5.1 Film Structure, Composition, and Morphology

The films prepared in Chapter 2 were shown to have compositionally graded profiles, with surface enrichment of both gallium and S. The films had sharp, split x-ray diffraction peaks, indicating the presence of multiple phases within these materials. Further discussion of the composition, structure, and morphology of these materials can be found in Chapter 2, Section 4.

3.5.2 Initial photoresponse and current-voltage characteristics

Initial photoresponse measurements of the samples showed a negative photovoltage shift upon illumination, indicating p-type conductivity. P-type materials are desirable for photoelectrochemical water splitting. In a p-type PEC set-up, water is reduced to hydrogen at the electrode surface, and the electrode is cathodically protected from corrosion by minority carrier electrons at the surface. Current-voltage curves in dark and light can give an indication of the photoactivity. Small amounts of both positive and negative photocurrent in these materials can be observed under illumination, indicating low-doped or intrinsic behavior, and photoinduced electron transfer, shown in Figure 3.5. Due to the initial photovoltage measurements, this material can be considered as low-doped p-type. In this low-doped material, the Fermi level sits near mid-gap relative to the conduction and valence bands. Under bias and/or illumination, the Fermi level will move toward either the conduction or valence band depending on the direction of applied potential, shown in Figure 3.6. This in turn allows both reductive and oxidative current to flow, and photocurrent is observed both at moderate positive and negative potentials.

71
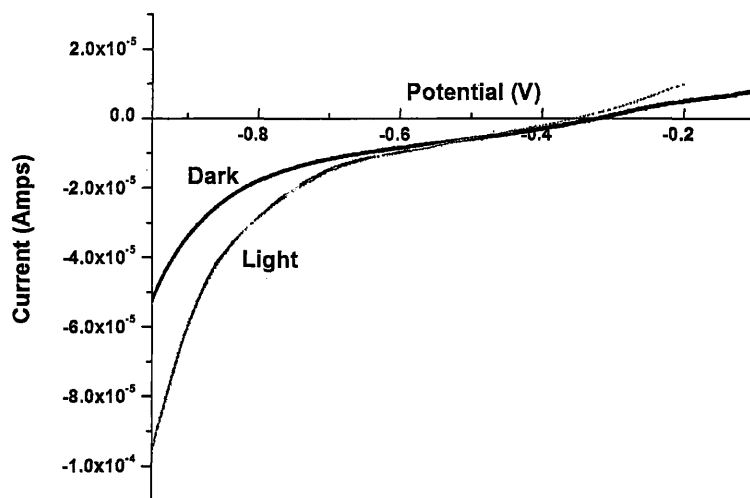
Figure 3.5 Current-voltage characteristics (vs. Ag/AgCl reference) of a film in both dark and 1-sun illumination. The response shows both positive and negative photocurrent, indicating a low-doped material.
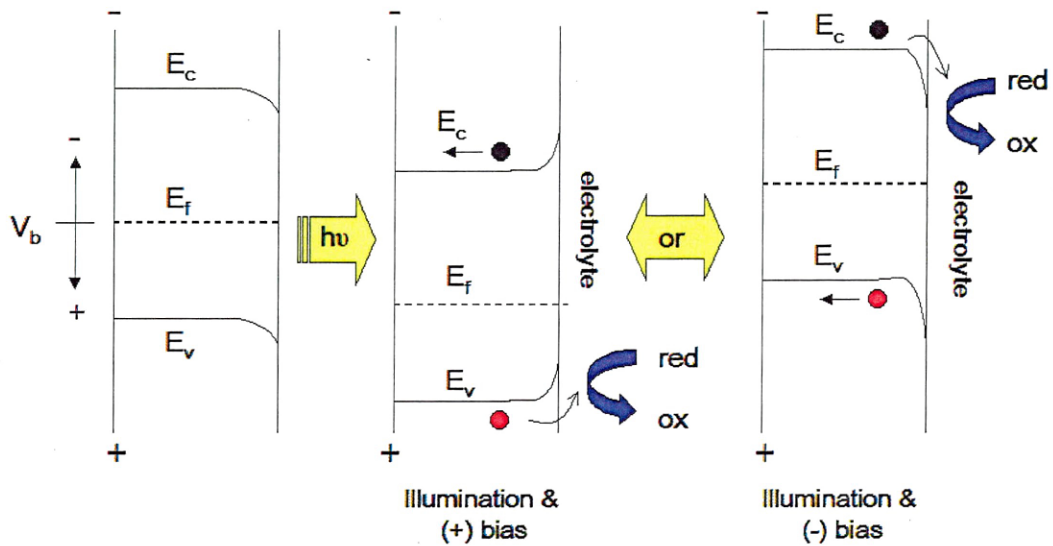
Figure 3.6 Semiconductor band diagrams showing the valence band (E_v), conduction band (E_c) and Fermi level (E_f) positions under voltage bias (V_b) and illumination. Black dots and red dots represent electrons and holes, respectively.

3.5.3 Band gap grading

Using AES depth profile data, compositional ratios of gallium {x = Ga/(Ga+In)}, and S {y = S/(S+Se)} were calculated throughout the depth of films. Equation (3.6) was then applied to this data to show the predicted band gap throughout the depth of the film based on these compositional ratios x and y.

Figure 3.7 shows an AES depth profile and calculated band gap results from a representative film. This figure illustrates the trend seen in all materials from this set, showing a higher calculated band gap in the top of the film, decreasing throughout the depth of the material. A higher band gap correlates to both gallium and sulfur enrichment in the top portion of the film. It can be seen

that the increase in gallium and sulfur ratios causes a direct increase in the band gap overall, as is expected, since they represent x and y in the band gap prediction equation. A low calculated band gap is seen at the surface of the material due to the formation of surface oxides on air and moisture exposure, giving inaccurate ratios of x and y.
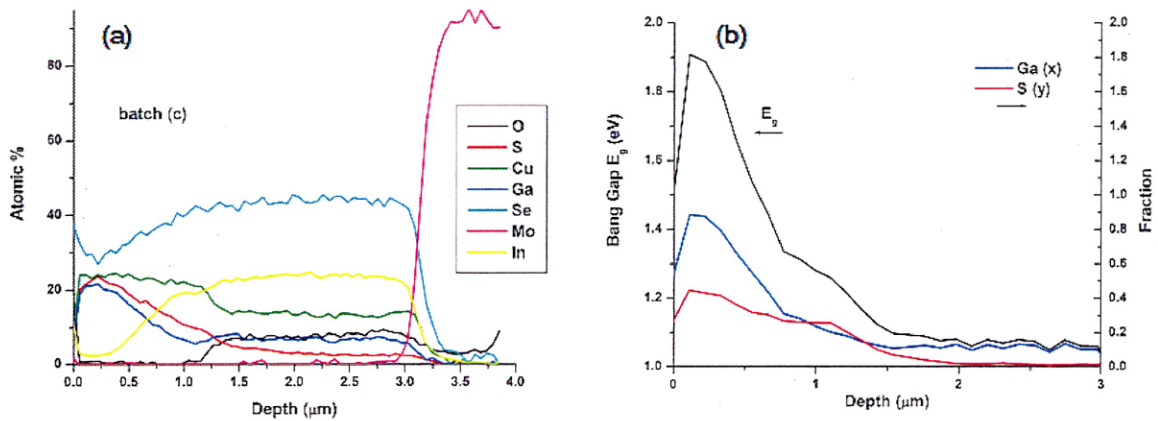
Figure 3.7 (a) AES depth profile of film A, showing gallium and sulfur grading in the material. (b)The calculated band gap profile showing a graded band gap due to these variations.

As the alloy composition changes, the conduction and valence band positions change within the film. It was stated earlier that gallium affects the conduction band position, and it is also known that sulfur substitution in these materials affects both the valence and conduction band position[9]. A qualitative energy diagram illustrating the influence of sulfur and gallium enrichment in these films can be seen in Figure 3.8.
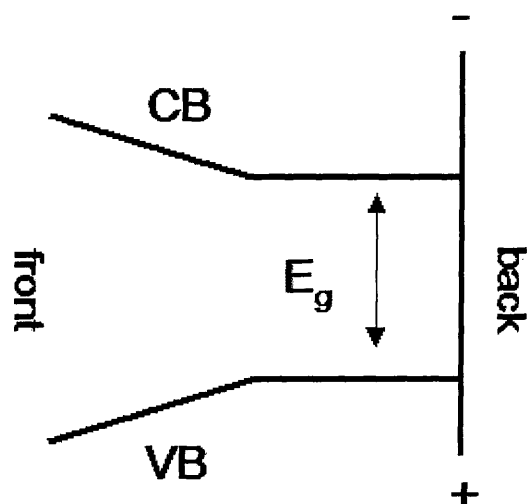
Figure 3.8 Band edge and band gap grading from samples with sulfur and gallium surface enrichment, showing the resulting shifts in conduction and valence band positions.

The increased band gap at the front region of the film allows for a larger open circuit voltage (V_{oc}) from the material. A larger open circuit voltage allows for more driving force for the water splitting reaction. The decrease in valence band position shuttles holes toward the back contact, which is a desirable feature for reducing electron-hole recombination in the space-charge region and increasing overall current from the device. The conduction band increase at the surface shuttles electrons toward the back contact, which increases recombination with holes in this region, undesirably decreasing the photoresponse. The extent to which this counteracts the transport of holes to the back contact will depend on the amount of conduction band and valence band shifts relative to each other, which ultimately depends on the amount of gallium and sulfur in the surface of the material. It is still undecided what the optimum thickness or depth of grading within the space charge region provides the

greatest overall device efficiencies[6]. The energetics in these materials are not ideal for either PV or PEC applications.

3.5.4 Photocurrent spectroscopy

Photocurrent spectroscopy measurements reveal two band gaps for these films, as seen in Table 3.2. The experimentally obtained high and low band gap spectra are shown in Figure 3.9(a) and (b), respectively. Two different band gaps arise due to the inhomogeneity of the materials, with solid solutions of $CuInSe_2 - CuGaS_2$ having a large range of possible band gap values. The observed high band gap results from the surface of the material with a higher gallium and sulfur content. The second, lower band gap, corresponds to the large volume of low band gap material in the bottom of the film containing little gallium and S.

The measured band gaps correlate to values that appear in the calculated grading profiles, though not the highest or lowest calculated values in every case. All of the higher band gap values occur within the top 0.35µm of the film, as determined from the depth profiles. The high absorption coefficient of CIS materials allows for a top thin layer of the film to absorb the majority of incident photons, and thus exhibit optical properties of this portion of the film. The presence of oxygen in the materials and inherent errors in elemental analysis may give rise to calculations resulting in values that don't accurately represent experimentally observed band gaps. Empirically obtained values can be correlated with a specific depth composition in the film, however this depth is not the same in all of the films.

76

Table 3.2 High and low band gap values experimentally observed in films with gallium and sulfur surface enrichment

Sample	E_g^1 (eV)	E_g^2 (eV)
A	1.21	1.91
B	1.16	1.93
C	1.22	1.83
D	1.10	1.85
E	1.23	1.75
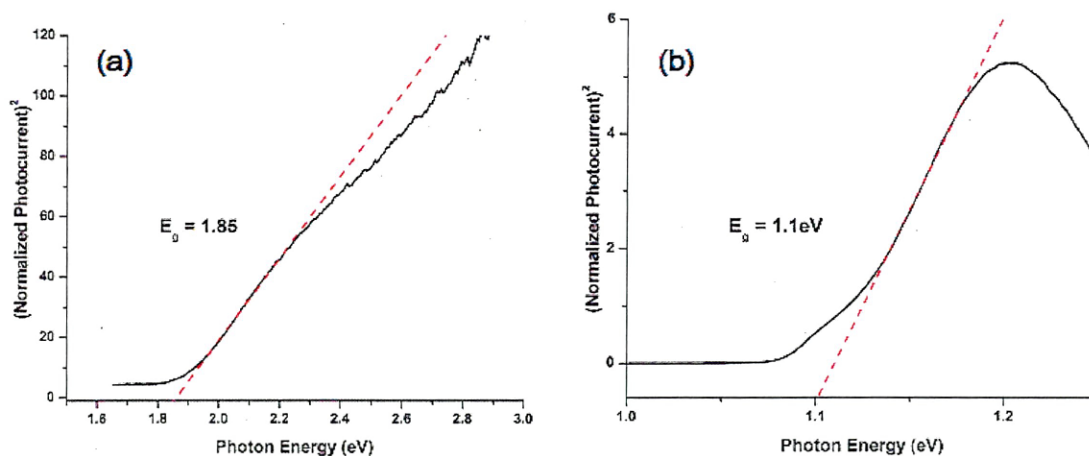
Figure 3.9 Photocurrent spectroscopy plots from sample D used to experimentally determine the band gap of these materials. **(a)** High observed band gap resulting from gallium and sulfur enriched film surface. **(b)** Lower observed band gap from bottom portion of film with little gallium and sulfur incorporation.

3.6 Conclusions and Future Work

A graded band gap structure is of significant interest in both photovoltaic and photoelectrochemical applications. The valence and conduction band positions in CIGSS thin films are affected by the amount of gallium and sulfur in the alloy. Intentional grading of these energetics is typically performed in CIS-based photovoltaic absorbers to increase efficiency and reduce recombination, however this approach has never been applied to PEC devices. In PEC, the positions of the conduction and valence bands can determine the ability to complete the water redox reactions, as well as increasing system efficiency and reducing recombination.

Band gaps of thin film alloys of CIGSS, prepared as described in a previous chapter, were investigated. AES depth profiles of these films allow the calculation of gallium and sulfur ratios as a function of depth. An equation to predict the band gap of these materials as a function of these ratios was developed from semiconductor alloy theory. This equation was then applied to the experimentally determined compositional ratios to illustrate the band gap variation with film depth. Films with gallium and sulfur surface enrichment were predicted to have higher band gaps at the surface of the film.

Photocurrent spectroscopy was used to experimentally determine the optical band gaps in these materials. Two band gaps were observed in these materials due to the presence of multiple alloy phases. Of these two observed band gaps, the higher value fulfills the band gap requirement for a PEC water splitting system. These materials had band gap values in the range of 1.75 − 1.93eV. Both experimentally observed band gaps appear in the grading profile calculated using the developed alloy equation. The lower band gap represents

the latter half of the film, where there is little gallium and sulfur incorporation. This is further evidence for the presence of two chalcopyrite phases in these materials, with different compositions, and thus different band gaps.

An optimal energetic scheme for PEC would have a minimum band gap of 1.7eV maintained throughout the film. This band gap energy can be achieved with both sulfur and gallium enrichment of $CuInSe_2$. Using these compounds to create a back surface field with gallium slightly increasing toward the back contact will increase overall efficiency. In addition, the increase of sulfur toward the surface can act in the same way. This can be achieved by the tradeoff of gallium and sulfur in the alloy, to maintain the same band gap, yet beneficially contributing to the surface energetics. This can be achieved using the electrodeposition/enrichment technique of material synthesis outlined in Chapter 2. Precursors with a high gallium content should be used, since gallium diffuses toward the back contact during annealing. Using a high gallium-content precursor film, and enriching it in an In_2S_3 atmosphere in the presence of a selenium overpressure may provide the increased sulfur content toward the surface, with an increased gallium content near the back contact, all while maintaining high enough ratios of both for a minimum 1.7eV band gap.

Developing a way to calculate the band gap in these complex pentenary systems is very important in maximizing our knowledge of their usefulness. Knowing the desired band gap profile, several compositions fitting this requirement can be calculated. Several compositions can be manufactured, each giving rise to the same band gap. This will allow for the determination of corrosion and energetic effects of gallium and sulfur alloying in $CuInSe_2$.

Theory has calculated that sulfur alloying alone cannot bring the valence band into the correct position for PEC water splitting[9]. Investigation of further band edge engineering through surface modifications and etching will play a role in determining the outlook for using singe CIGSS absorber layers for direct water splitting devices. Another possibility exists to couple these materials with an internal biasing layer, such as that in a monolithic PEC tandem device.

<u>REFERENCES</u>

1. O. Madelung, M. Schulz, and H. Weiss, eds. <u>Physics of Ternary Compounds</u>. Numerical Data and Functional Relationships in Science and Technology, Vol. 17; Semiconductors. 1985, Springer-Verlag: Berlin.

2. T. Bak, J. Nowotny, M. Rekas, and C.C. Sorrell, Photo-Electrochemical Hydrogen Generation from Water Using Solar Energy: Materials-Related Aspects. *International Journal of Hydrogen Energy* **27**, p. 991-1022 (2002).

3. K. Ramanathan, M.A. Contreras, C.L. Perkins, S. Asher, F.S. Hasoon, J. Keane, D. Young, M. Romero, W. Metzger, R. Noufi, J. Ward, and A. Duda, Properties of 19.2% Efficiency $ZnO/CdS/CuInGaSe_2$ Thin-Film Solar Cells. *Progress in Photovoltaics: Research and Applications* **11**, p. 225-230 (2003).

4. M.A. Contreras, J. Tuttle, A. Gabor, A. Tennant, K. Ramanathan, S. Asher, A. Franz, J. Keane, L. Wang, and R. Noufi, High Efficiency Graded Bandgap Thin-Film Polycrystalline $Cu(In,Ga)Se_2$-Based Solar Cells. *Solar Energy Materials and Solar Cells* **41-42**, p. 231-246 (1996).

5. S.H. Wei, S.B. Zhang, and A. Zunger, Effects of Ga Addition to $CuInSe_2$ on Its Electronic, Structural, and Defect Properties. *Applied Physics Letters* **72** (24), p. 3199-3201 (1998).

6. M. Topic, F. Smole, and J. Furlan, Band-Gap Engineering in $CdS/Cu(In,Ga)Se_2$ Solar Cells. *Journal of Applied Physics* **79** (11), p. 8537-8540 (1996).

7. C.H. Huang, S.S. Li, and T.J. Anderson, Device Modeling and Simulation of Cis-Based Solar Cells. *Conference Record of the Twenty-Ninth IEEE Photovoltaic Specialists Conference 2002 (Cat. No.02CH37361)*, p. 748-751 (2002).

8. M. Bar, W. Bohne, J. Rohrich, E. Strub, S. Lindner, M.C. Lux-Steiner, C.-H. Fischer, T.P. Niesen, and F. Karg, Determination of the Band Gap Depth Profile of the Pentenary $Cu(in_{(1-x)}Ga_x)(S_yse_{(1-Y)})_2$ Chalcopyrite from Its Composition Gradient. *Journal of Applied Physics* **96** (7), p. 3857-3860 (2004).

9. S.-H. Wei and A. Zunger, Band Offsets and Optical Bowings of Chalcopyrites and Zn-Based II-VI Alloys. *Journal of Applied Physics* **78** (6), p. 3846-3856 (1995).

10. J.D. Beach, *$In_xGa_{1-x}N$ for Photoelectrochemical Water Splitting*, PhD. Thesis in *Department of Physics*. 2001, Colorado School of Mines: Golden.

CHAPTER 4

CuGaSe$_2$/ITO/Si TANDEM PHOTOELECTRODES

FOR SOLAR-HYDROGEN PRODUCTION

4.1 Abstract

Thin film semiconductors are a desirable option for photoelectrochemical (PEC) hydrogen production due to the potential for high conversion efficiency as well as low-cost and large-area fabrication. CuInSe$_2$ (CIS) and related thin films have been thoroughly studied for application as solar energy conversion devices yielding high photovoltaic (PV) efficiencies. CuGaSe$_2$, with a band gap of ~1.7 eV, is a semiconductor in this alloy group with the minimum band gap for a PEC water splitting system. Previous studies have shown several materials within this system have a valence band position that is negative of the H$_2$O/O$_2$ oxidation potential, thus inhibiting the completion of the water splitting reaction in this system. The addition of bias from a photovoltaic (PV) junction within the electrode has been shown in other material systems to provide sufficient additional voltage to overcome these energetics, and does not require additional energy input from an outside source. Monolithic tandem cell configurations for photoelectrochemical hydrogen production have shown record efficiencies for solar energy conversion[1]. In this study, CuGaSe$_2$ (CGS) is examined as a top layer absorber on a Si PV junction in a tandem monolithic PEC device. These tandem materials are compared to individual CGS photoelectrodes to examine the potential of an ideal tandem system using CGS. While CGS alone has band edges too negative, the valence band position of the tandem cell is positive of the

83

water oxidation potential at most pHs, indicating potential water splitting capabilities. Preliminary tests on single absorbers show potential for sufficient corrosion resistance during water reduction.

4.2 Introduction

Large-area, high-speed fabrication methods and low-cost material requirements combined with high theoretical efficiencies make thin film semiconductors a desirable option for photoelectrochemical (PEC) hydrogen production. $CuInSe_2$ (CIS) and related thin films have been thoroughly studied as solar energy conversion devices, and high photovoltaic (PV) efficiencies (>19%) have been realized using $Cu(In,Ga)Se_2$[2]. While CIS has a band gap of about 1 eV and would not be suitable for direct water splitting, it has been shown that incorporation of gallium into CIS to form $Cu(In,Ga)Se_2$ (and finally $CuGaSe_2$) can increase the band gap to approximately 1.7 eV[3], the minimum band gap for a PEC water splitting system. Previous studies have shown several materials within this system have a valence band position that is negative of the H_2O/O_2 oxidation potential, thus inhibiting the completion of the water splitting reaction in this system[4-6].

Electrically biasing this system can overcome these non-ideal energetics; however, a bias from an external source of energy input is to be avoided. The addition of a bias from an internal photovoltaic (PV) junction in the form of a tandem device has been shown in other material systems to provide enough additional voltage to overcome these energetics. An internal PV bias does not require additional energy input from an outside source, nor complicated wiring schemes. Monolithic tandem cell configurations for photoelectrochemical

hydrogen production have shown record efficiencies for solar energy conversion[1].

Monolithic tandem cell configurations consist of a top PEC layer in series with a tunnel junction layered onto a PV substrate. An illustration of a tandem device is seen in Chapter 1. The role of the tunnel junction is to allow barrierless charge transfer from the top layer to the bottom layer (and vice versa). A good tunnel junction will make ohmic contact with the other layers without introducing additional system resistance. Tunnel junctions must be transparent as to not interfere with the absorption of lower energy photons in the bottom layer. For these reasons, transparent conducting oxides (TCO) are the chosen materials for this application. In this instance, indium-doped tin oxide (ITO) interfaced with the top p-CGS layer is used as the tunnel junction. Previous studies have shown that the $Cu(In,Ga)Se_2$/ITO heterojunction shows ohmic-behavior, and ITO has been successfully substituted as a back contact in CIGS PV applications[7].

Theory states that the optimum band gaps for a two absorber tandem system are 1.73eV and 1.16eV for maximum conversion efficiency[8]. $CuGaSe_2$ and Si are good matches to the band gap requirements for high efficiency tandem cells, with values of ~1.7eV and 1.1eV, respectively. In this study, $CuGaSe_2$ (CGS) is examined as a top layer absorber on a Si PV junction in a tandem monolithic PEC device. The optimum theoretical efficiency for CGS on Si is calculated for both photovoltaic and photoelectrochemical systems. Band edge positions, corrosion characteristics, and current-voltage behavior is evaluated for an experimental tandem device. This material is then compared to the performance of a single layer CGS absorber to examine the practical capabilities of this tandem system.

4.3 Theoretical Efficiencies

Multijunction photovoltaic structures have many possible configurations. Here, a two-terminal tandem structure utilizing CGS as the top layer and Si as the bottom layer are examined for both the theoretical photovoltaic and photoelectrochemical water splitting efficiencies.

The efficiency (η) of a photovoltaic cell is shown in Equation (4.1)[9], where V_{max} and J_{max} are the voltage and current at maximum power point, respectively, V_{oc} is the open circuit voltage, J_{sc} is the short circuit current, P_{out} is the output power of the cell, P_{in} is the total incoming power of radiation, and FF is the fill factor, defined in Equation (4.9).

$$\eta = \frac{P_{out}}{P_{in}} = \frac{V_{max}J_{max}}{P_{in}} = \frac{V_{oc}J_{sc}FF}{P_{in}} \tag{4.1}$$

When dealing with a tandem cell structure, an important factor is current matching within the system. Both cells are in series, and the current will be limited by the lower of the two cell currents. The overall efficiency (η_{total}) is the sum of the calculated efficiencies from each material when connected in series, seen in Equation (4.2)[10], where J_{sc} is the lower short circuit current density of the two materials.

$$\eta_{total} = \frac{J_{sc}V_{oc}^{CGS}FF^{CGS} + J_{sc}V_{oc}^{Si}FF^{Si}}{P_{in}} \tag{4.2}$$

The short circuit current in each cell can be calculated based on the band gap values and photon flux at a specific air mass. For this calculation it is

assumed that each incident photon that is absorbed generates one electron-hole pair in the semiconductor material. Both Air Mass 0 (AM0) and Air Mass 1.5 (AM1.5) data obtained from standard reference spectra[11, 12] are used, shown in Figure 4.1. The corresponding band gaps of both CGS and Si are indicated in this figure, showing the portion of the solar spectrum available for conversion in each layer.
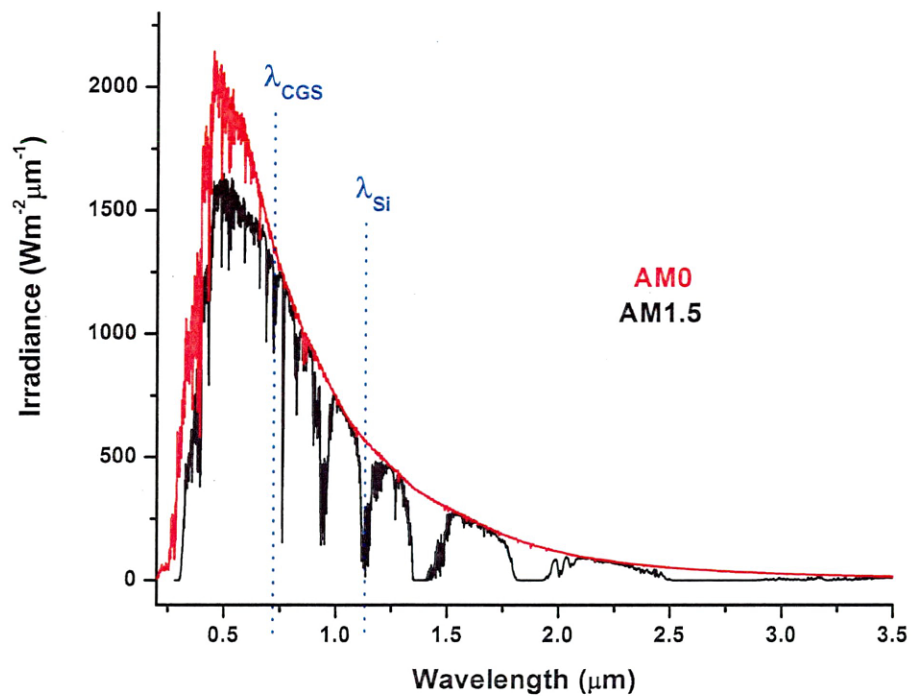
Figure 4.1. AM0 and AM1.5 spectral irradiance, showing the CGS (λ_{CGS}) and Si (λ_{Si}) band gap wavelengths. Only photons with a wavelength less than or equal to the band gap of the material can be absorbed.

Equation (4.3)[10] is used to determine the theoretical J_{sc} for each layer, where q is the electron charge and F(λ) is the photon flux at wavelength λ. The distribution of photon flux is integrated from low wavelengths, starting at 0.2um, up to the energy threshold (band gap) wavelength at which photons can no longer be absorbed in the top layer, or CGS. The photons with energies smaller than the band gap will pass through the top layer to the bottom portion of the device, which in turn absorbs photons equal to or greater in energy than its band gap. The bottom cell J_{sc} is then determined by integrating from the top cell limiting wavelength to the wavelength of its own limiting absorption (band gap).

$$J_{sc}^{CGS} = \int_{0.2\,\mu m}^{\lambda_{CGS}} qF(\lambda)d\lambda \ , \ J_{sc}^{Si} = \int_{\lambda_{CGS}}^{\lambda_{si}} qF(\lambda)d\lambda \qquad (4.3)$$

Open circuit voltage calculations are based on material parameters that vary between material systems. Equation (4.4)[9] shows the V_{oc} calculation, where J_0 is the dark saturation current. V_{oc} was determined using the J_{sc} for Si in both cases, since it is the lowest of the two values.

$$V_{oc} = \frac{kT}{q} \ln\left(\frac{J_{sc}}{J_0} + 1 \right) \qquad (4.4)$$

The dark saturation current in a material is a function of several material properties, including diffusion properties and carrier concentrations, and is represented by Equation (4.5)[9].

$$J_o = \left(\frac{qD_e n_i^2}{L_e N_A} + \frac{qD_h n_i^2}{L_h N_D} \right) \qquad (4.5)$$

D_e and D_h are the diffusion coefficients for electrons and holes, respectively, L_e and L_h are the diffusion lengths for electrons and holes, respectively, and N_A and N_D are the acceptor and donor doping densities, respectively. These constants are not well known for many semiconductors, and often the value of J_0 is estimated by using Equation (4.6) and inputting the highest reported V_{oc} and J_{sc} values from the literature to back calculate an estimated value. This was done for both Si and CGS, using literature values for V_{oc} to obtain J_0 [13, 14]. These V_{oc} values were used throughout the rest of the calculations.

The current-voltage (J-V) characteristics of a solar cell are described by Equation (4.6), with all variables previously defined. This is known as the Ideal Diode Equation in semiconductor physics[9].

$$J = J_0 \left[\exp(\frac{qV}{kT}) - 1 \right] - J_{sc} \tag{4.6}$$

Using the values obtained for both Si and CGS, the current-voltage characteristics of these individual cells in a tandem device are shown in Figure 4.2 for AM 0 and Figure 4.3 for AM 1.5. Si exhibits lower current due to the absorption of high energy photons by the top layer that do not reach the Si layer, and thus do not contribute to the generation of electron-hole pairs in this layer. The actual diode curve of the tandem device will be a composite of these individual curves, with the J_{sc} of Si limiting the current observed overall.

89
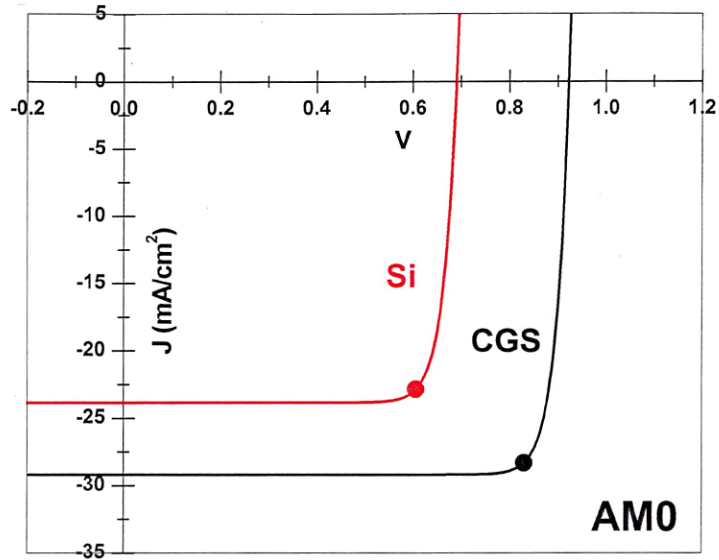
Figure 4.2 Theoretical diode curves at AM0 for Si and CGS in a tandem device. The calculated maximum power point is illustrated for each material in this device.
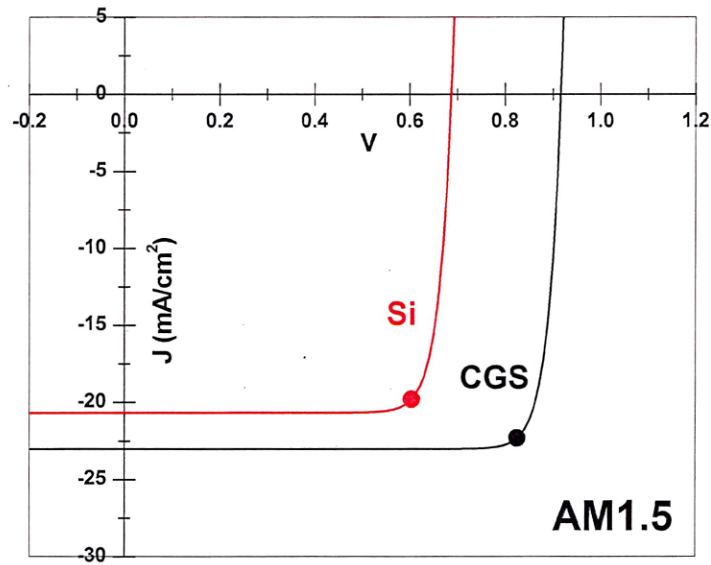
Figure 4.3 Theoretical diode curves at AM1.5 for Si and CGS in a tandem device. Maximum power points are marked for each material in this device.

To find the maximum power point voltage (V_{max}), which is needed for the calculation of the fill factor, the power expression in Equation (4.7) is differentiated and set equal to zero to find the value of V at maximum power, V_{max}. This differential equation shown in Equation (4.8) was then implicitly solved [15] using Mathematica's DSolve method. This calculation was based on J_{sc} of Si in each case, since it is the limiting current.

$$P = JV = J_o V \left[\exp\left(\frac{qV}{kT}\right) - 1 \right] - J_{sc} V \qquad (4.7)$$

$$\frac{qV_{max}}{kT} \left[\exp\left(\frac{qV_{max}}{kT}\right) - 1 \right] + \exp\left(\frac{qV_{max}}{kT}\right) = \frac{J_{sc}}{J_o} + 1 \qquad (4.8)$$

Using V_{max}, the fill factor can be determined by Equation (4.9), as given by Fan, et al.[10].

$$FF = \frac{V_{max}}{V_{oc}} \left[1 - \frac{\exp\left(\frac{qV_{max}}{kT}\right) - 1}{\exp\left(\frac{qV_{oc}}{kT}\right) - 1} \right] \qquad (4.9)$$

Using the fill factor (FF), V_{oc}, and J_{sc} for each individual cell, the overall efficiency is calculated according to Equation (4.2). This results in an overall theoretical photovoltaic conversion efficiency for a tandem device of this nature of 33% for AM0, and greater than 28% for AM1.5 solar insolation.

Table 4.1 shows constants used for both Si and CGS calculations and the resulting values obtained. The rest of the values are calculated from the equations set forth in this text. The two calculated values are those from AM 0 and AM 1.5, respectively. Note that these cells are electrically connected in series such that the voltages add, giving ~1.6V, which is sufficient for water splitting at these current densities. Actual calculations done using Mathematica are found in Appendix 2.

Table 4.1 Experimentally determined and theoretically calculated parameters used to determine tandem cell efficiencies. Two calculated values are from AM 0 and AM 1.5 radiation, respectively.

	<u>Si</u>	<u>CGS</u>	
V_{oc} (Literature)	0.702V	0.905V	Single Absorber
J_{sc} (Literature)	42.2mA/cm^2	14.88mA/cm^2	
J_o (Calculated)	5.82 E -11	9.32 E -15	Tandem Cell (AM 0 and AM 1.5)
J_{sc} (Theoretical)	23.82, 20.64 mA/cm^2	29.18, 23.01 mA/cm^2	
V_{oc} (Theoretical)	.691, .688 V	.917, .913 V	
V_{max}	.608, .605 V	.827, .823 V	
FF	.844, .844	.874, .874	
PV Efficiency	AM0: 33.0% AM1.5: 28.4%		

The theoretical maximum efficiency of the water splitting process can be found from Equation (4.10) by using the Gibbs Free Energy of hydrogen at 25°C as the voltage and the theoretical short circuit current density values from the solar cell calculations[16].

$$\eta = \frac{P_{out}}{P_{in}} = \frac{JV}{P_{in}} = \frac{J(1.23V)}{P_{in}}$$

(4.10)

The smaller of the two J_{sc} values is used since the cells are current limited when in tandem. Results in Table 4.2 are shown for both AM0 and AM1.5 conditions.

Table 4.2 Calculated theoretical solar-to-hydrogen conversion efficiencies for a tandem CGS/Si device at both AM0 and AM1.5 conditions.

	AM0	AM1.5
PEC Efficiency	29.3%	25.4%

It is important to keep in mind that theoretical J_{sc} values obtained are for photovoltaic devices. In CIS-based photovoltaics, a CdS or similar buffer layer is used in these devices. This buffer layer is thought to play an important role in photovoltaic performance by creating a p-n heterojunction[17]. In a PEC cell, this buffer layer is not used, and a Schottky-like junction is created by putting the semiconductor in contact with solution, creating a space charge region within the semiconductor. This region contributes to charge separation, however, the amount to which the semiconductor/liquid junction can contribute relative to the buffer layers used in PV devices is not known at this time. This makes predicting the true efficiency of a CIS-based PEC device based on PV parameters only an approximation of realizable performance.

4.4 Experimental

Tandem CGS/Si and single CGS thin film absorbers were fabricated in-house at NREL. Single absorber devices were deposited via three source physical vapor deposition (PVD) on molybdenum-coated soda lime glass substrates. Tandem devices investigated in this study were grown as $CuGaSe_2/ITO/n^{++}$-Si:p-Si, as seen in Figure 4.4. The $CuGaSe_2$ top layer was deposited on top of the ITO-coated Si solar cell using three source PVD, with a resulting thickness of 1.3 μm, confirmed by Auger depth profiling. The ITO tunnel junction was deposited using reactive sputtering onto a p-n Si substrate. The profile in Figure 4.5 reveals an even elemental distribution throughout the film, and a tunnel junction thickness of approximately 150nm corresponding to the thickness of the ITO layer.

Monolithic $CuGaSe_2$ Tandem Cell
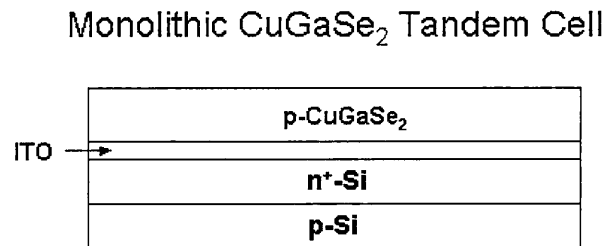
Figure 4.4 Physical representation of layered $CuGaSe_2/Si$ tandem structure.
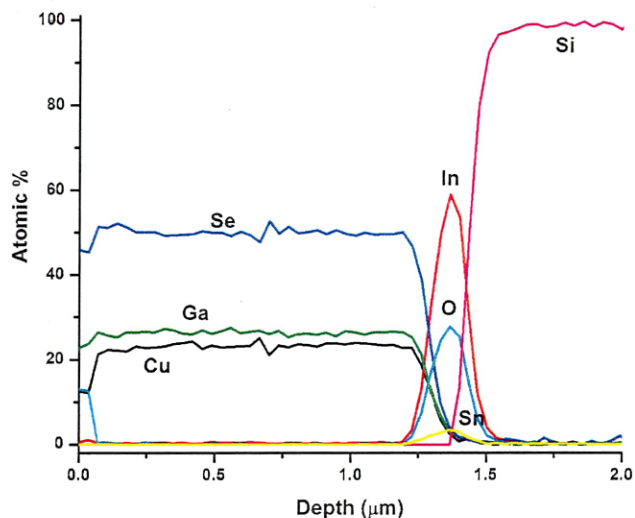
Figure 4.5 AES depth profile showing homogeneous distribution of elements throughout the film, with a CGS layer thickness of ~1.3um.

Illuminated open-circuit potential measurements were performed to determine the semiconductor flat-band potentials at different pH. Measurements were performed using a two-electrode cell set-up, with the working semiconductor electrode and an Ag/AgCl reference. High-intensity illumination from an Oriel DC lamp fitted with a 150W tungsten bulb was used to illuminate the electrode, and the open circuit potential measured using a Solartron 1287A potentiostat. Hydrion buffers were used as the pH solutions for flat band measurements.

When the cell is in open-circuit conditions, charge carriers generated from illumination accumulate in the depletion region of the semiconductor (Appendix 1) instead of performing redox reactions. As these charge carriers accumulate,

they reduce the electric field and thus the band bending within the space charge region of the semiconductor/electrolyte interface. If the illumination is of sufficient intensity, these charge carriers will flatten the bands until the generation of charge carriers is equal to their recombination, and the measured potential is the flat-band potential. This band flattening is shown in Figure 4.6.
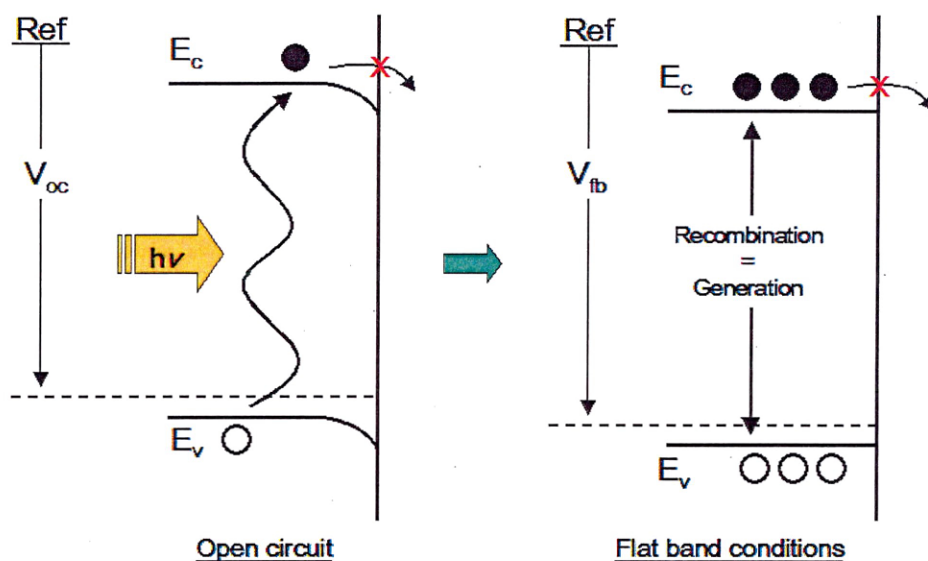
Figure 4.6 Band flattening during illuminated open circuit potential measurements enabling the determination of the flat-band potential (V_{fb}).

Three electrode current-voltage measurements were performed using a Pt foil counter electrode, and a saturated Ag/AgCl reference electrode. Two electrode measurements were performed using a platinum counter electrode. Illumination from a Cole-Parmer 41500 fiber-optic illuminator using a 150W tungsten bulb was used to approximate one-sun light intensity ($100mW/cm^2$), and the DC lamp

was used for higher intensity illumination, both calibrated using an Astral AD30 optical power meter. One sun current-voltage characteristics as well as high intensity light measurements were carried out separately in 1 mM ruthenium hexamine as a redox couple, 3M sulfuric acid, and 1M potassium hydroxide solutions.

Potentiodynamic analysis of the single absorber was performed by scanning from negative to positive potentials in a two electrode cell using a sulfuric acid electrolyte at pH 1, in both dark and 1 sun conditions. Further corrosion characteristics of these materials were examined under hydrogen production in a two-electrode cell, with $2mA/cm^2$ galvanostatically applied for a given length of time in 3M sulfuric acid. The corrosion solution contained Triton-X 100 as a surfactant to reduce the size of gas bubbles on the electrode surface.

Platinization of the samples was performed prior to corrosion measurements in order to reduce kinetic limitations at the material surface and therefore better understand barriers to the hydrogen production reaction at the semiconductor/electrolyte interface. To platinize the surface of the semiconductor, the electrode was immersed in an approximately 20mM solution of hexachloroplatinic acid. Reductive current was pulsed for 20 cycles: 0.5s on, 2s with no current passing for a total of $10mC/cm^2$ charge transfer. The platinization was done under ½ sun illumination from the fiber optic illuminator, in order to create charge carriers at the semiconductor surface, thus enhancing platinum deposition. The platinum is thought to be in the form of dispersed nanoparticle islands[18].

Auger Electron Spectroscopy (AES) depth profiling was used to examine the film compositions as a function of device depth. AES measurements were

performed at 5.0 keV with a Physical Electronics PHI 670 Auger instrument. Inductively coupled plasma employing mass spectroscopy detection (ICP/MS) was used to determined solution concentrations from corrosion measurements.

4.5.1 Flat Band Potentials

Illuminated open circuit potential measurements were performed to determine the effect of pH on the flat band potentials of these materials. Figure 4.7 shows flat band potentials (vs. NHE) for both the single absorber and tandem CGS materials. The single absorber shows valence band positions that cannot perform the water oxidation reaction, confirming previous reports on the CIS system. The valence band position of the tandem cell is positioned positive of the water oxidation potential at most pHs, indicating potential water splitting capabilities. The positive shift in the band position in the tandem cell is between 600-800mV, which is the expected output voltage from a Si p-n junction. From the empirically determined flat band potentials, a band energy diagram in pH 4 for the tandem device is shown in Figure 4.8. This band energy diagram shows the electron flow through the system, with the band edges straddling the water red-ox potentials, representing water splitting conditions.
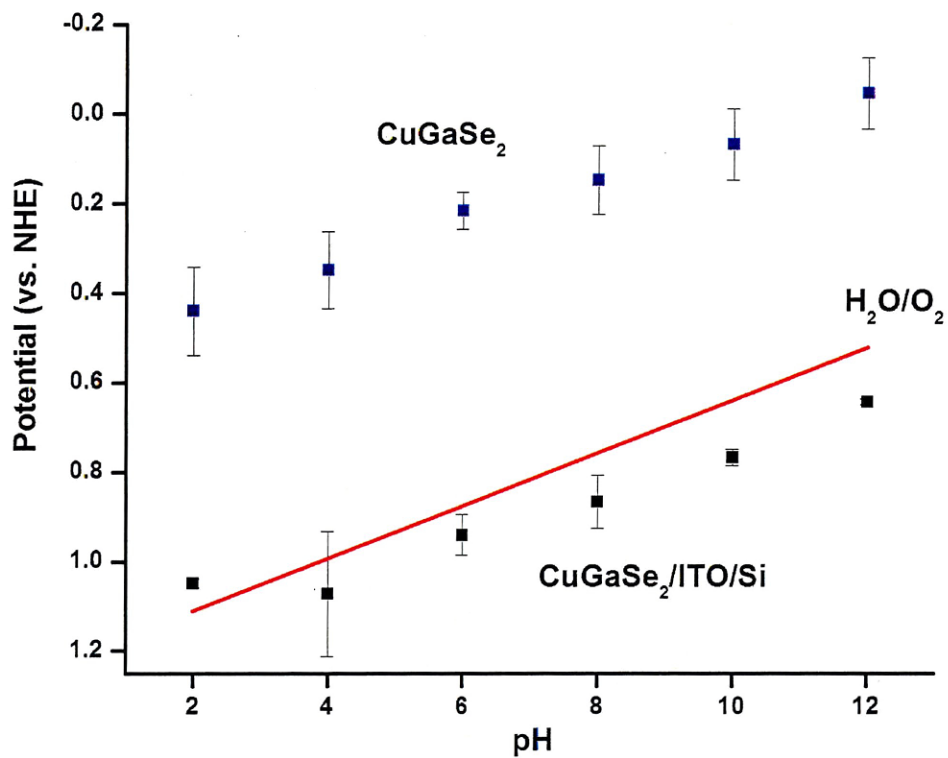
Figure 4.7 Flat band potentials of single CGS absorbers and the tandem device obtained by illuminated open-circuit potential measurements. Shown is the water oxidation potential.
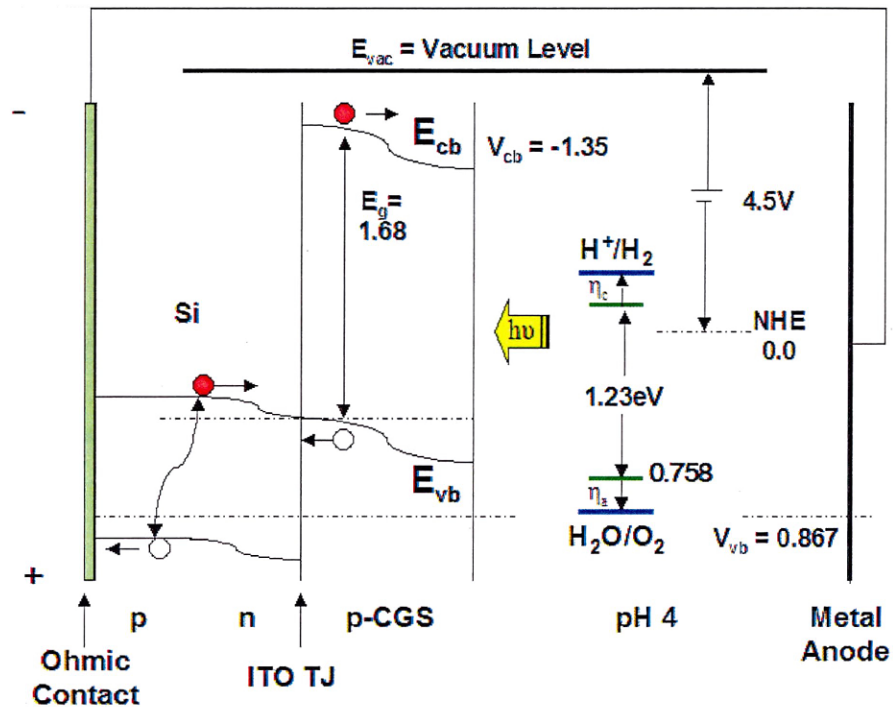
Figure 4.8 pH 4 energy diagram for a CGS on Si tandem device. Valence band potential is slightly positive of the water oxidation, favoring the completion of the water splitting reaction.

4.5.2 Current Voltage Characteristics

Figure 4.9 illustrates observed hysteresis in the illuminated current-voltage measurements of these materials between anodic and cathodic scans, showing surface reaction upon anodic bias. This anodic scan is affecting the surface of the material, possibly through oxidation or activation of surface species, resulting in a more favorable surface for reduction. This is seen in cathodic scans after anodic polarization, which show negative short circuit current, indicating unassisted reduction processes occurring at the electrode surface. The maximum current observed at 1-sun illumination on a cathodic scan after anodic polarization in ruthenium hexamine is -5.7μA.

Using the short circuit current obtained at 0V bias, the water splitting efficiency is calculated as 0.01%. This value is far from the estimated theoretical conversion efficiency of this tandem device. It is important to note that the observed short circuit current may be due to the photocurrent induced reduction of surface oxides as opposed to the reduction of H^+ to H_2.
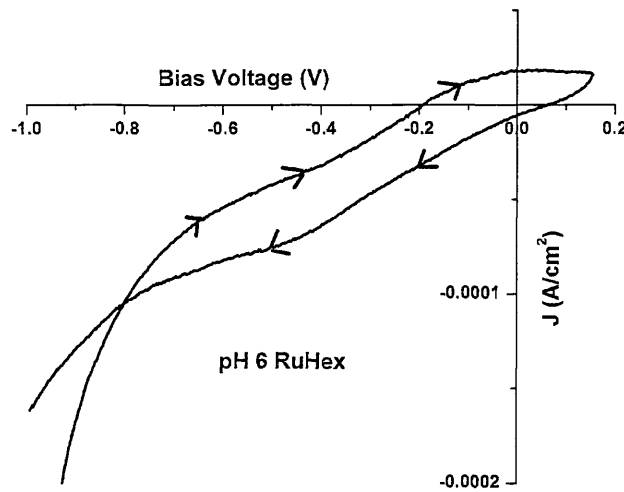
Figure 4.9 Two electrode current-voltage characteristics performed under 1-sun illumination. Observed hysteresis indicates electrochemical surface modification on the cathodic scan.

4.5.3 Corrosion Characteristics

Corrosion characteristics of the tandem materials were examined under hydrogen production conditions. Galvanostatic reduction was performed, with $2mA/cm^2$ current passed over two hours in a 3M sulfuric acid electrolyte. SEM surface images of the tandem devices taken after corrosion testing show delamination of the top CGS layer from the underlying tunnel junction, shown in Figure 4.10a. Area (a) is seen to contain components of the CGS top layer shown in the AES survey scans in Figure 4.10. The darker area (b) exhibits none of the components from the CGS or the interconnect layer in the AES survey scan. Only a Si signal is observed, indicating that the CGS layer delaminated, and the ITO is no longer present at the interface.
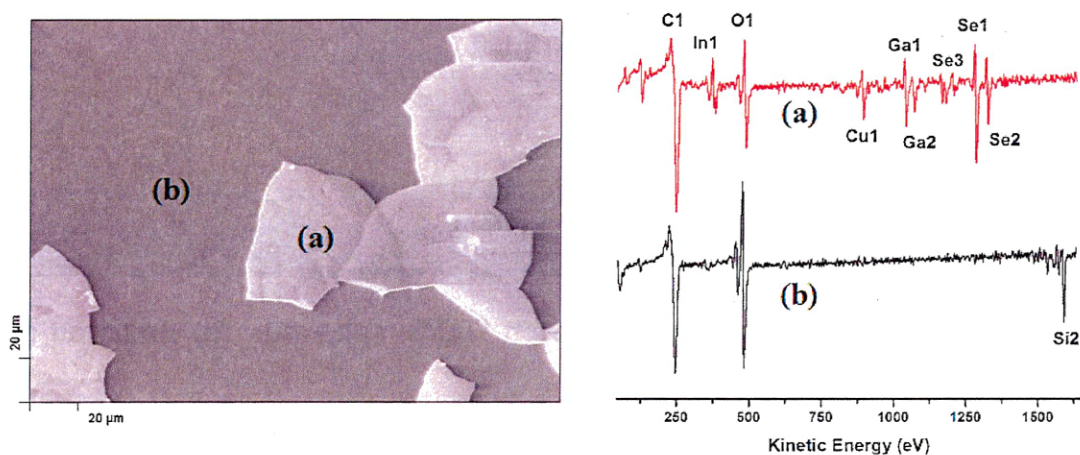
Figure 4.10 SEM image of tandem cell surface after corrosion test in 3M H_2SO_4 with corresponding AES survey scans. Area (a) is $CuGaSe_2$ film, and area (b) shows no indium signal from the substrate.

SEM investigation of the as-deposited material revealed microcracks in the top layer of CGS, seen in Figure 4.11. Indium-tin-oxide is known to be unstable in acid and reducing environments[19]. Diffusion of acidic electrolyte through these cracks in the top layer to the ITO tunnel junction and resulting reductive dissolution of the oxide layer caused the delaminating of the top layer. Thermal cracking of the ITO on the Si substrate at temperatures of 650°C for one hour during the CGS deposition likely affected the morphology of the top layer, which took on the cracked morphology as it was being deposited.
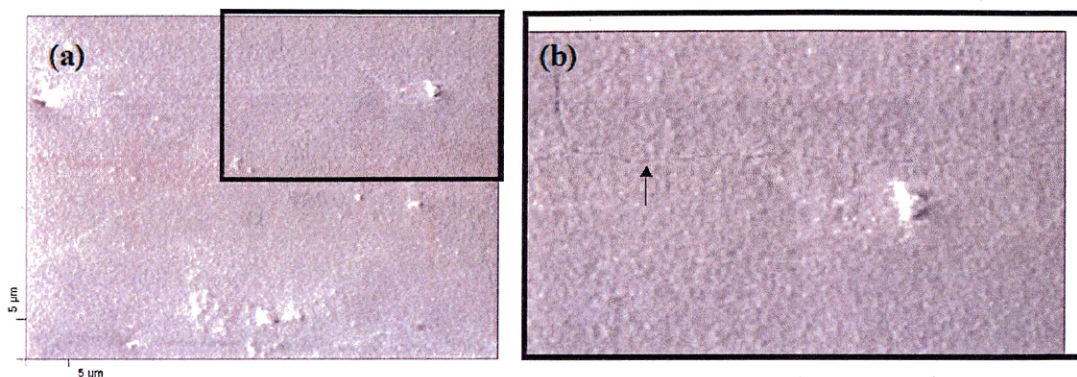
Figure 4.11 (a) As deposited $CuGaSe_2$ on ITO/Si substrate. **(b)** Enlarged area showing microcracks in the CGS film.

Single CGS layers were examined to determine the optimum corrosion characteristics of the top PEC layer in this tandem device. Preliminary investigation of single layer CGS showing good morphology revealed short-term stability of the material under reductive conditions. Potentiodynamic analysis shown in Figure 4.12 shows a reduction in anodic current under illumination, demonstrating cathodic protection of CGS. The illumination of the device creates charge carriers which decrease the oxidative current and metal dissolution at the surface of the semiconductor.
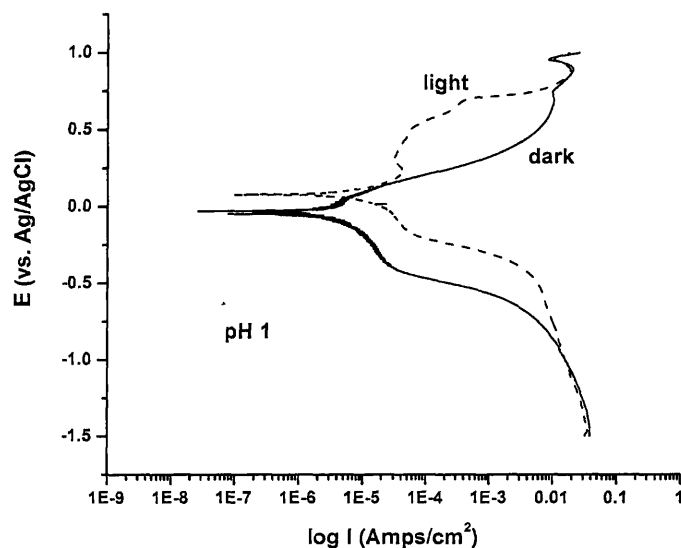
Figure 4.12 Potentiodynamic analysis of a CGS single absorber in dark and under illumination showing cathodic protection.

Corrosion of the single absorber during water photolysis was performed over a 24 hour period according to the same conditions used for the tandem device. Analysis of the corrosion solution via ICP/MS was performed, and results for the 24 hour corrosion test are shown in Table 4.4. A large amount of copper relative to the other elements was found in the corrosion solution, indicating the preferential removal of copper during hydrogen production. There are several possibilities for the dissolution of copper from the surface of the electrode. It has been shown that the native oxidation of CGS results in the formation of $Cu(OH)_2$, Ga_2O_3, and SeO_2 at the surface. This surface oxide formation is said to be accelerated by humid air[20], and it can thus be concluded that an aqueous environment will enhance this formation. The presence of a surface oxide or other surface species is evidenced by the redox waves observed in the current voltage measurements.

The concentrations of Cu, Ga, and Se in the corrosion solution can be used to calculate a corresponding thickness of the chalcopyrite structured material using Equation (4.11). For these calculations, C_x is the concentration of compound x in ppb in the solution, V_{soln} is the volume of corrosion solution, N_A is Avogadro's number, Vol_{cell} is the chalcopyrite $CuGaSe_2$ unit cell volume, MW is the molecular weight of compound x, N_x is the number of atoms of x in the unit cell, A is the electrode surface area, and 10^6 is a unit conversion factor. The parameters used in this equation for each element are listed in Table 4.3.

$$Etch\ Depth(cm) = \frac{C_x \cdot V_{sol'n} \cdot N_A \cdot V_{cell}}{MW \cdot N_x \cdot A \cdot 10^6} \qquad (4.11)$$

Table 4.3 Values used in the calculation of etch depths during corrosion measurements.

	Cu	Ga	Se
MW (g/mol)	63.55	69.72	78.96
N_x	13	10	8
Vol_{cell} (cm^3)		3.46 E -22	

The film thickness correlating to the quantity of dissolved material is seen in Table 4.4. The calculations for gallium and selenium show similar values, whereas the amount of material corresponding to the copper concentration in solution is an order of magnitude higher. This suggests the preferential dissolution of copper from the material, or the preferential formation of copper-oxide surface layers, and thus the dissolution of more copper from the film surface. When placed in contact with the sulfuric acid solution for corrosion

measurements, this surface oxide dissolves readily in solution according to Equation (4.12).

$$Cu(OH)_2 + 2H^+ \rightarrow Cu^{2+} + 2H_2O \qquad (4.12)$$
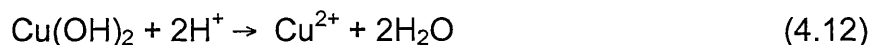
The presence of small quantities of gallium and selenium can also be attributed to the dissolution of these surface oxides, present in lesser amounts at the surface. The calculated thicknesses from the ICP analysis of the corrosion solution are based on the assumption that there is dissolution of the semiconductor lattice. There are 31 atoms in the ABC_2 chalcopyrite unit cell; 13 A atoms, 10 B atoms, and 8 C atoms. This does not represent the structure or number of atoms in an oxide layer. Thus, the calculated depth of corrosion only represents the corrosion of crystalline chalcopyrite semiconductor, and not that of the oxide layer. If the presence of the metal ions in solution is due to the dissolution of native oxides formed during air exposure, then the degradation of the material surface will be limited by the amount of native oxide formed. Once the material is under reductive conditions, the formation of these oxides will no longer be occurring, and the dissolution of the material will cease or be significantly reduced.

Table 4.4 Elemental concentrations in a 24 hour corrosion solution obtained by ICP/MS analysis. Calculated theoretical thickness of the dissolved film based on a chalcopyrite $CuGaSe_2$ unit cell structure.

	Cu	Ga	Se	Mo
Concentration (ppb)	106	7.4	9.2	4.09
Thickness (nm)	57	4.7	6.5	n/a

Comparisons of AES depth profiles on as-deposited and corroded CGS layers can be seen in Figure 4.13a and 4.13b, respectively. Depth profiles show an apparent 105nm difference in thickness between the corroded and as-grown sample. This is greater than the thickness of the dissolved layer calculated from ICP analysis of the corrosion solution. It is likely that the apparent difference in thickness is due to variations and anomalies during AES sputtering and analysis, making the actual depth of corrosion very difficult to quantify via this method.

The presence of surface oxides is observed in the depth profiles of both as-grown and corroded samples. In the corroded sample, there is no preferential removal of copper from the surface in greater quantity than selenium or Ga, and does not correspond to the thickness of observed film dissolution. This 24 hour corrosion test led to the removal of .004 - .007 μm of film, as calculated from the gallium and selenium data. This is a very promising result, supporting the hypothesis that cathodic protection inhibits dissolution of the material during device operation, and the formation and dissolution of native oxides is the main mechanism for material degradation.
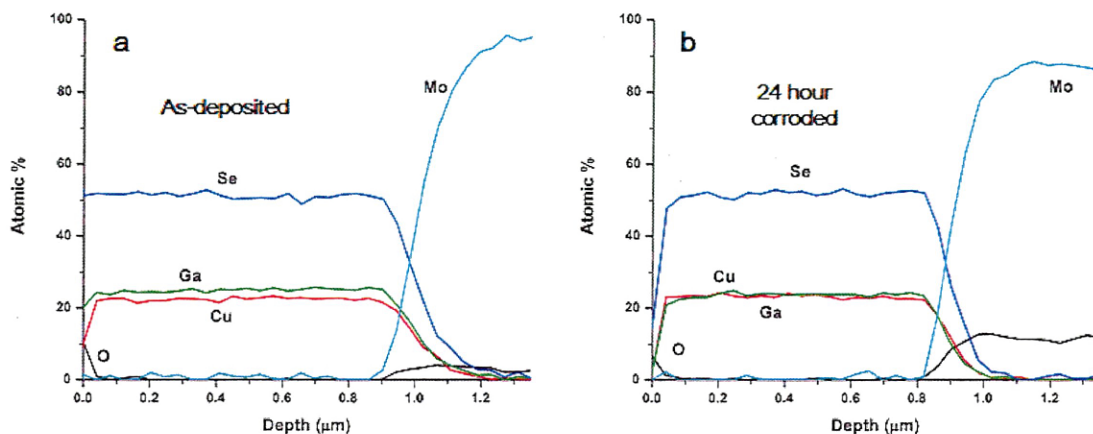
Figure 4.13 AES depth profiles of **(a)** uncorroded and **(b)** 24hr. corroded CGS absorber layers, showing similar depth profiling.

4.6 Conclusions and Future Work

Measurements show the band edge positions of single $CuGaSe_2$ absorbers cannot complete the water redox reaction. However, with built-in internal bias in a monolithic tandem device, system energetics show the possibility of water splitting. With a theoretical solar-to-hydrogen conversion efficiency of more than 25% in AM1.5 conditions, $CuGaSe_2$/Si tandem devices show great promise for photoelectrochemical hydrogen production.

Low experimental efficiency was achieved in fabricated CGS/ITO/Si tandem devices. This is not necessarily representative of attainable efficiencies due to the poor quality of the interconnect, which can cause device shorting and current loss. Optimization of the tunnel junction could greatly increase this efficiency.

Tandem cells showed corrosion due to interconnect instability, and will require further optimization of both the top layer and the interconnect material in these devices. An interconnect layer must be carefully chosen based on the growth and operating parameters of the system. For this tandem material, the interconnect must withstand high deposition temperatures in order to optimize the top layer morphology. With suitable morphology, there is less chance of the interconnect contacting solution, and thus the sensitivity of the interconnect to acidic environments may not be a concern. Other transparent conducting oxide interconnect materials such as fluorine-doped tin oxide (FTO) may reduce or eliminate this problem.

Other possibilities for improved film morphology and increased layer compatibility include lower temperature CGS depositions. Electrodeposition followed by annealing using temperatures lower than those for vapor deposited films is a possibility. Annealing electrodeposited CIS-based materials at temperatures in the range of 400-550°C has shown crystallization[21-23]. The success of this technique will depend on the ability of the substrate and tunnel junction to withstand these temperatures and annealing times. The electrodeposition of high gallium content thin films will also play an important role if these materials are to be fabricated at lower temperatures and cost.

Tests on single $CuGaSe_2$ absorbers show cathodic protection against oxidation under illumination. In a functioning device, only this top layer will be exposed to solution, and will be a key determining factor in the overall stability of these materials. Corrosion during hydrogen production in aqueous solution is hypothesized to be minimal in these reductive conditions. Dissolution of surface oxides produced from air exposure prior to testing is hypothesized to be the main mechanism for material corrosion. These initial results are promising in terms of

the lifetimes of these tandem systems, however in-depth corrosion studies are still necessary.

With improved film morphology and optimized tunnel junction interconnects, these materials show promise for photoelectrochemical water splitting, and are recommended for further investigation in tandem PEC configurations.

REFERENCES

1.   O. Khasalev and J.A. Turner, A Monolithic Photovoltaic-Photoelectrochemical Device for Hydrogen Production Via Water Splitting. *Science* **280** (17 April 1998), p. 425-427 (1998).

2.   M.A. Contreras, K. Ramanathan, J. AbuShama, F. Hasoon, D.L. Young, B. Egaas, and R. Noufi, Diode Characteristics in State-of-the-Art Zno/Cds/Cu(In$_{1-x}$Ga$_x$)Se$_2$ Solar Cells. *Progress in Photovoltaics: Research and Applications* **13** (3), p. 209-216 (2005).

3.   O. Madelung, M. Schulz, and H. Weiss, eds. Physics of Ternary Compounds. Numerical Data and Functional Relationships in Science and Technology, Vol. 17; Semiconductors. 1985, Springer-Verlag: Berlin.

4.   S. FernandezValverde, E. OrdonezRegil, R. ValenciaAlvarado, R. RiveraNoriega, and O. SolorzaFeria, Mass Spectrometry Quantification of Hydrogen Produced under Illumination of P-CuInSe$_2$ and Modified Surfaces. *International Journal of Hydrogen Energy* **22** (6), p. 581-584 (1997).

5.   A.M. Martinez, L.G. Arriaga, A.M. Fernandez, and U. Cano, Band Edges Determination of CuInS$_2$ Thin Films Prepared by Electrodeposition. *Materials Chemistry and Physics* **88** (2-3), p. 417-420 (2004).

6.   J.E. Leisch, R.N. Bhattacharya, G. Teeter, and J.A. Turner, Preparation and Characterization of Cu(In,Ga)(Se,S)$_2$ Thin Films from Electrodeposited Precursors for Hydrogen Production. *Solar Energy Materials and Solar Cells* **81** (2), p. 249-259 (2004).

7.   F.J. Haug, D. Rudmann, A. Romeo, H. Zogg, and A.N. Tiwari, Electrical Properties of the Heterojunction in Cu(In,Ga)Se$_2$ Superstrate Solar Cells. *Proceedings of 3rd World Conference on Photovoltaic Energy Conversion (IEEE Cat. No.03CH37497)*, p. 2853-8 Vol.3 (2003).

8.   T.J. Coutts, K.A. Emery, and J.S. Ward, Modeled Performance of Polycrystalline Thin-Film Tandem Solar Cells. *Progress in Photovoltaics: Research and Applications* **10**, p. 195-203 (2002).

9.   M.A. Green, *Solar Cells: Operating Principles, Technology, and System Applications*. 1982, Kensington: University of New South Wales.

10. J.C.C. Fan, B.Y. Tsaur, and B.J. Palm, Optimal Design of High-Efficiency Tandem Cells. *Conference Record of the Sixteenth IEEE Photovoltaic Specialists Conference - 1982*, p. 692-701 (1982).

11. ASTM, *ASTM G173-03 Tables: Extraterrestrial Spectrum, Terrestrial Global 37 Deg South Facing Tilt & Direct Normal + Circumsolar.* 1999.

12. ASTM, *2000 ASTM Standard Extraterrestrial Spectrum Reference E-490-00.* 2000, ASTM.

13. D.L. Young, J. Keane, A. Duda, A.M. AbuShama, C.L. Perkins, M. Romero, and R. Noufi, Improved Performance in $ZnO/CdS/CuGaSe_2$ Thin-Film Solar Cells. *Progress in Photovoltaics: Research and Applications* **11** (8), p. 535-541 (2003).

14. M.A. Green, K. Emery, D.L. King, S. Igari, and W. Warta, Solar Cell Efficiency Tables (Version 26). *Progress in Photovoltaics: Research and Applications* **13** (5), p. 387-392 (2005).

15. M.J. Morgan, G. Jakovidis, and I. McLeod, An Experiment to Measure the I-V Characteristics of a Silicon Solar Cell. *Physics Education* **29**, p. 252 (1994).

16. T. Bak, J. Nowotny, M. Rekas, and C.C. Sorrell, Photo-Electrochemical Hydrogen Generation from Water Using Solar Energy. Materials-Related Aspects. *International Journal of Hydrogen Energy* **27**, p. 991-1022 (2002).

17. Q. Nguyen, K. Orgassa, I. Koetschau, U. Rau, and H.W. Schock, Influence of Heterointerfaces on the Performance of $Cu(In,Ga)Se_2$ Solar Cells with CdS and $In(OH_X,S_Y)$ Buffer Layers. *Thin Solid Films* **431-432**, p. 330-334 (2003).

18. A. Heller, E. Aharon-Shalom, W.A. Bonner, and B. Miller, Hydrogen-Evolving Semiconductor Photocathodes. Nature of the Junction and Function of the Platinum Group Metal Catalyst. *Journal of the American Chemical Society* **104**, p. 6942-6948 (1982).

19. S.W. Gaarenstroom, M.P. Balogh, M.C. Militello, R.A. Waldo, C.A. Wong, N.A. Kelly, T.L. Gibson, and M.D. Kundrat, Characterization of Indium-Tin-Oxide Films with Improved Corrosion Resistance. *Surface and Interface Analysis* **37** (4), p. 385-392 (2005).

20. R. Wurz, A. Meeder, D.F. Marron, T. Schedel-Niedrig, A. Knop-Gericke, and K. Lips, Native Oxidation of $CuGaSe_2$ Crystals and Thin Films Studied by Electron Paramagnetic Resonance and Photoelectron Spectroscopy. *Physical Review B (Condensed Matter and Materials Physics)* **70** (20), p. 205321-1-205321-205321-10 (2004).

21. C. Guillen and J. Herrero, Effects of Thermal and Chemical Treatments on the Composition and Structure of Electrodeposited $CuInSe_2$ Thin-Films. *Journal of the Electrochemical Society* **141** (1), p. 225-230 (1994).

22. N. Stratieva, E. Tzvetkova, M. Ganchev, K. Kochev, and I. Tomov, Structural and Optical Properties of Electrodeposited $CuInSe_2$ Layers. *Solar Energy Materials and Solar Cells* **45** (1), p. 87-96 (1997).

23. L. Zhang, F.D. Jiang, and J.Y. Feng, Formation of $CuInSe_2$ and $Cu(In,Ga)Se_2$ Films by Electrodeposition and Vacuum Annealing Treatment. *Solar Energy Materials and Solar Cells* **80** (4), p. 483-490 (2003).

CHAPTER 5

ELECTRODEPOSITION OF CUGASE$_2$ THIN FILMS

5.1 Abstract

CuGaSe$_2$ is a chalcopyrite semiconductor with a band gap near 1.7eV. It
has been studied as a top layer in a monolithic tandem device for
photoelectrochemical water splitting. Typically, CuGaSe$_2$ is deposited via high-
temperature vapor deposition techniques. Here, electrodeposition is studied as a
low-temperature and low-cost route to the synthesis of CuGaSe$_2$ thin films.
Electrodeposition of CuInSe$_2$ and Cu(In,Ga)Se$_2$ thin films for photovoltaics has
been reported, however the gallium content in these materials is low. Gallium
incorporation has previously been shown to be difficult to obtain via
electrodeposition due to its exceedingly negative reduction potential in aqueous
solution. Using aqueous metal salt solutions, the effect of concentration,
deposition potential, and substrate identity on the electrodeposition of gallium
containing thin films was studied. The early onset of the H$_2$ gas evolution reaction
was found to contribute to poor film deposition and adhesion at large negative
potentials. Hydrogen reduction was found to occur at a more positive potential on
molybdenum electrodes than on indium-doped tin-oxide substrates. Varying the
Se/Cu ratio in solution affected the overall film composition, with higher ratios
suppressing gallium deposition until more negative potentials. Thin films
containing high gallium ratios were obtained and confirmed by ICP
measurements. Diffraction patterns of deposited films showed Cu$_x$Se$_y$ phases

present, however no peaks associated with gallium or Ga-compounds were observed.

5.2 Introduction

With a band gap of ~1eV, $CuInSe_2$ thin films are of significant interest in photovoltaic (PV) research. Gallium is commonly alloyed with these chalcopyrite materials, forming $Cu(In,Ga)Se_2$, which effectively increases the band gap, resulting in better photovoltaic performance in graded films[1]. Gallium incorporation in $CuInSe_2$ brings the material band gap closer to the ideal value of 1.4eV for solar energy conversion [2]. $CuGaSe_2$, on the other hand, is not typically investigated as an individual PV material due to its higher band gap of 1.7eV. However, using this high band gap material coupled to a lower band gap material in a tandem device could be promising for a high efficiency PV or photoelectrochemical (PEC) water splitting device.

In Chapter 4 we described the vapor deposition of $CuGaSe_2$ on an indium-doped tin oxide (ITO) coated silicon p-n junction in order to produce a tandem PEC water splitting device. The silicon junction acts as an internal PV bias, shifting the energetics of the device into desired positions for photoelectrochemical water splitting. One problem with this system was the incompatibility of the ITO layer at high temperature deposition conditions, resulting in thermal cracking and system breakdown in solution. Attempting to fabricate these materials in a low-temperature manner may eliminate the issue of interconnect instability, as well as reduce overall system cost.

CuInSe$_2$, Cu(In,Ga)Se$_2$, and CuGaSe$_2$ have been fabricated by several routes including physical vapor deposition and chemical vapor deposition, outlined in Chapter 1. Only CuInSe$_2$ and Cu(In,Ga)Se$_2$ have been reported to be prepared via electrodeposition[3], a low cost, ambient temperature and pressure method of thin film synthesis. However, CuGaSe$_2$ has not been electrodeposited, due to the difficulty in obtaining adequate amounts of gallium in the film. Examining the reduction potentials of the components shown in Equations (5.1) to (5.3), it is seen that gallium has a very negative standard reduction potential (E^0) of -0.549 vs. NHE[4],.

$$Cu^{2+} + 2e^- \Leftrightarrow Cu \qquad E^0 = +0.342V \qquad\qquad (5.1)$$

$$Ga^{3+} + 3e^- \Leftrightarrow Ga \qquad E^0 = -0.549V \qquad\qquad (5.2)$$

$$H_2SeO_3 + 4e^- + 4H^+ \Leftrightarrow Se + 3H_2O \qquad E^0 = +0.739V \qquad (5.3)$$
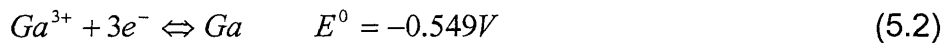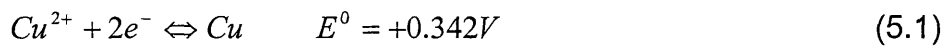
The Nernst Equation in (5.4) describes the concentration dependence of the cell potential. Here, R the ideal gas constant, T is temperature, F is the Faraday constant, n is the number of electrons transferred, and [Red] and [Ox] the activities of the reduced and oxidized species in solution. In very dilute solutions the activity of the ions can be assumed to be equal to their concentration, however in more concentrated solutions and in the presence of other ions, the activity will depend on the interaction between all of the solution components, and their behavior can be difficult to predict[5].

$$E = E^\circ - \frac{RT}{nF}\ln Q \quad ; \quad Q = \frac{[\text{Red}]}{[\text{Ox}]} \qquad (5.4)$$

When the deposition reaction occurs at a potential more negative than the thermodynamically predicted potential, this additional voltage is known as the overpotential. The term polarization is used to describe this deviation from the standard reduction values. The overpotential in electrodeposition can arise from the rate of electron transfer, the nucleation rate of the alloy, and the rate of mass transport of the solute to the electrode surface[5, 6]. In diffusion limited electrode reactions, mass transport of ions from the bulk solution through the Helmholtz layer (see Appendix 1) to the electrode surface is considered to be the main influence on the reaction rate[5]. As the reaction at the electrode surface proceeds, the oxidized species is consumed, and more reduced species is formed at the electrode interface. A concentration gradient of the oxidized species is created. The flux of reactant to the electrode surface (J), and thus the rate of reaction at the electrode surface is given by Fick's Law (Equation (5.5)), where i is the current, n is the charge on the oxidized ion, D_{ox} is the diffusion coefficient of the ion,, and x is the distance from the electrode surface[5]. At the limiting current density, the oxidized species will react as soon as it reaches the electrode surface. It is seen that the rate of reaction (and thus magnitude of the current density) is dependent on the diffusion of oxidized to the electrode surface.

$$J = \frac{i}{nFA} = -D_{ox}\left(\frac{\partial[Ox]}{\partial x}\right)_{x=0} \tag{5.5}$$

Experimentally determined diffusion coefficients of the aqueous ions used in this study are shown in Table 5.1.

Table 5.1. Diffusion coefficients of the aqueous ions used in this study.

	D (cm^2s^{-1})	Reference
Cu^{2+}	6.6 E -6	[7]
$HSeO_3^-$	9.2 E -6	[7]
Ga^{3+}	1.9 E -6	[8]

Another very important reaction in the electrodeposition of metal and semiconductor thin films is the hydrogen evolution reaction, seen in Equation (5.6). This reaction usually occurs simultaneously with the reduction reactions of interest for the film deposition when water is used as the solvent, and the deposition potentials are negative of the H_2 evolution potential.

$$2H_{aq}^+ + 2e^- \rightarrow H_{2(gas)} \quad E = 0.0V - 0.059pH \qquad (5.6)$$
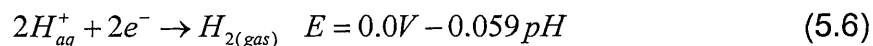
The reduction of H^+ at the electrode surface occurs at a potential that depends on the solvent pH, and in more acidic solution the onset of this reaction occurs at more positive potentials. This potential also varies depending on the nature of the electrode surface. At pH 2, the calculated voltage for the onset of the hydrogen production reaction is -0.12V vs. NHE (-0.32V vs. Ag/AgCl).

Solution pH also affects the state of the ions in solution through the formation of complex ions and precipitates. At pH 2, which was used in this study, Ga^{3+} is predicted to undergo only minimal formation of oxide or hydroxide compounds. Equation (5.7) shows the initial gallium complex formation step in aqueous solution. At pH 2, where the [OH⁻] is extremely low, most of the gallium is in the form Ga^{3+}.

$$GaOH^{2+} \rightleftarrows Ga^{3+} + OH^- \quad K = 4 \cdot 10^{-12} \tag{5.7}$$
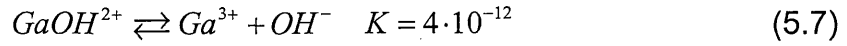
H_2SeO_3 has two protons which can dissociate with the equilibrium constants seen in Equation (5.8). At pH 2, $HSeO_3^-$ is the main form of selenous acid used in this work.

$$H_2SeO_3 \rightleftarrows H^+ + HSeO_3^- \quad K_1 = 2.7 \cdot 10^{-3}$$
$$HSeO_3^- \rightleftarrows H^+ + SeO_3^{2-} \quad K_2 = 2.6 \cdot 10^{-7} \tag{5.8}$$
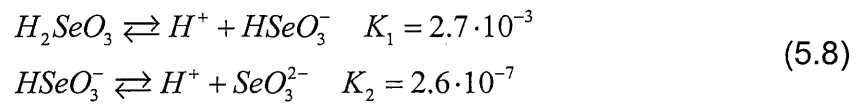
The mechanism of electrodeposition of $CuInSe_2$ alloy compounds is thought to occur through the initial formation of a binary Cu_xSe_y compound, followed by reaction with In^{3+} in the solution[9-11]. The formation of the $CuInSe_2$ compound can occur at more noble (positive) potentials than that of In^{3+} reduction alone, a process called alloy codeposition[12]. In codeposition, the Gibbs energy of formation of the alloy compound can shift the standard reduction potential to more positive values[13]. Equation (5.9) shows the influence of the Gibbs energy of formation (ΔG_f) on the reduction potential, where n is the number of electrons participating in the reduction reaction, and F is the Faraday constant. It can be seen that for any compound formation with a negative ΔG_f, the reduction potential will be shifted toward more positive values. Codeposition allows for the deposition of metal alloys from solution, even in conditions where the deposition of one of the lone alloy constituents may not occur at all.

$$\Delta E = -\frac{\Delta G_f}{nF} \tag{5.9}$$

In this study, $Cu_xGa_ySe_z$ alloy films are electrodeposited on both molybdenum and ITO-coated glass substrates. The effect of solution concentration and deposition potential on the composition of the deposited films is studied. Though the electrodeposition of $Cu(In,Ga)Se_2$ thin films has been previously studied, the electrodeposition of $CuGaSe_2$ has never been reported.

5.3 Experimental Methods

Electrochemical measurements were performed using a three electrode set-up, with a Pt foil counter electrode, an Ag/AgCl reference, and either a glassy carbon electrode, ITO/glass, or Mo/glass as the working electrode. All voltammograms were performed using a Solartron 1287 potentiostat, with a scan rate of 10mV/s from positive to negative potential. Electrodepositions were performed using the same counter and reference electrodes, and Mo/glass and ITO/glass were investigated as substrates. For the electrodepositions, the substrates were degreased by sonicating in acetone, then doubly rinsed in deionized water and dried in nitrogen. All solutions were made using 18MΩ purity deionized water with reagent grade chemicals. The salts used were $GaCl_3$ (10-100mM), $CuCl_3$ (10-100mM), and H_2SeO_3 (5-100mM), in varying quantities, depending on desired concentration. Initial experiments to determine the optimum pH for deposition showed that a pH approaching 3 and above caused the formation of $Ga(OH)_3$ (K_{sp} = 7.3E⁻36) as a white, gelatinous precipitate. It is desirable to use the highest possible pH to keep the reduction of hydrogen at the electrode surface to a minimum. The bath pH for these depositions was chosen to be pH 2, and maintained using a Hydrion phthalate buffer. Depositions were

123

performed potentiostatically versus the reference electrode, unstirred, for 30 minutes.

A PerkinElmer Elan DRC-e ICP-MS was used to determine the elemental concentrations in the deposited films. 100, 500, and 1000ppb solutions of Cu, Ga, and Se were used as standards. Solutions for ICP analysis were prepared by dissolving a 1cm^2 section of film in ~1mL of aqua regia then diluting to 25mL using deionized water of 18MΩ purity. The crystal structure of the films was investigated by x-ray diffraction (XRD) using a Scintag XGEN diffractometer with a Cu Kα anode source.

5.4 Results and Discussion

Current-voltage measurements were performed on individual solutions of 10mM GaCl$_3$, CuCl$_2$, and H$_2$SeO$_3$ in pH 2 buffer. The resulting curves at a glassy carbon electrode are shown in Figure 5.1, with the potential versus an Ag/AgCl reference. In these reduction waves, as the potential is scanned toward more negative values, the increase in the magnitude of the current density indicates a reaction at the electrode surface.

The reduction waves A and B observed for Cu^{2+} are attributed to the reactions in Equation (5.10).

$$\begin{aligned} A: \quad & Cu^{2+} + 2e^- \rightarrow Cu^0 \quad E^0 = +0.143 \left(vs. Ag/AgCl \right) \\ B: \quad & Cu^{2+} + e^- \rightarrow Cu^{1+} \quad E^0 = -0.038 (vs. Ag/AgCl) \end{aligned} \quad (5.10)$$
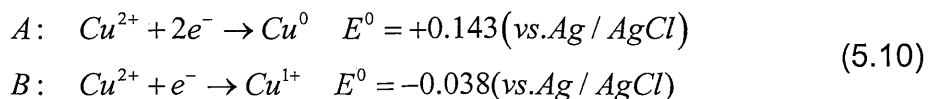
The reduction of H_2SeO_3 (Se^{4+}) to Se is observed in wave C via the mechanisms in Equation (5.11). The cathodic current after this peak is associated with continued Se^0 formation, as well as the further reduction of the Se to H_2Se (Se^{2-}).

$$C: \quad HSeO_3^- + 4e^- + 5H^+ \rightarrow Se^0 + 3H_2O$$
$$Se^0 + 2e^- + 2H^+ \rightarrow H_2Se$$

(5.11)
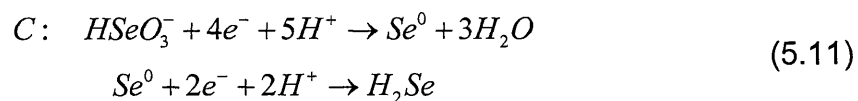
The reduction of gallium cannot be observed in this medium due to the preferential solvent reduction and production of hydrogen at this pH. Values of the observed reduction potentials all deviate from thermodynamic values due to solution concentrations, activities, and substrate effects.
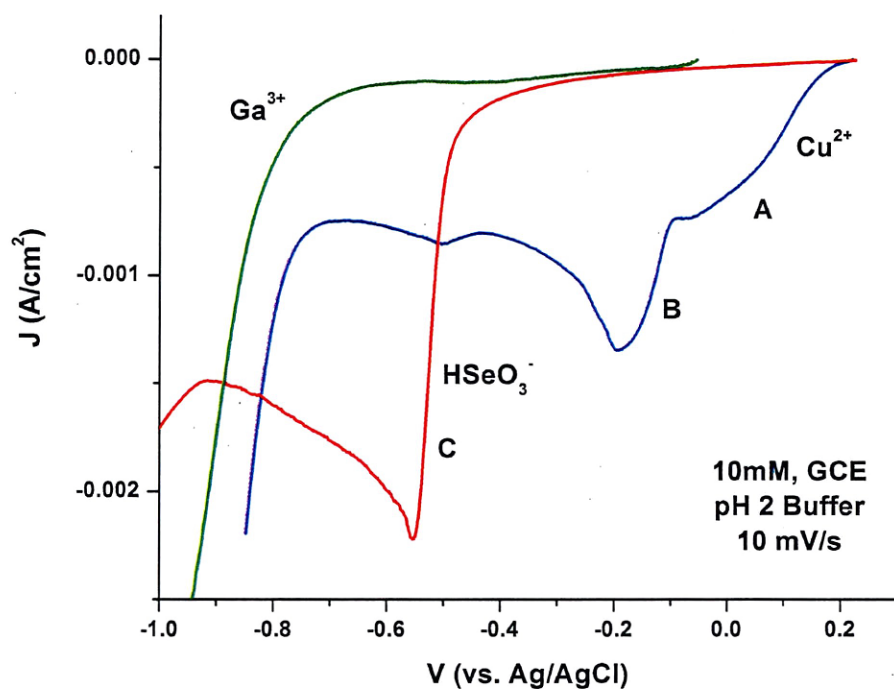
Figure 5.1 Voltammetry of individual 10mM solutions of $CuCl_2$, Ga_3Cl_3 and H_2SeO_3 at a glassy carbon electrode. The reduction waves labeled A, B, and C are correlated to the formation of Cu^0, Cu^{1+}, and Se^0, respectively.

5.4.1 Cu-Se System

Voltammetry was performed on solutions containing 10mM Cu^{2+} with varying ratios of Se/Cu (x). The voltammograms are presented in Figure 5.2.
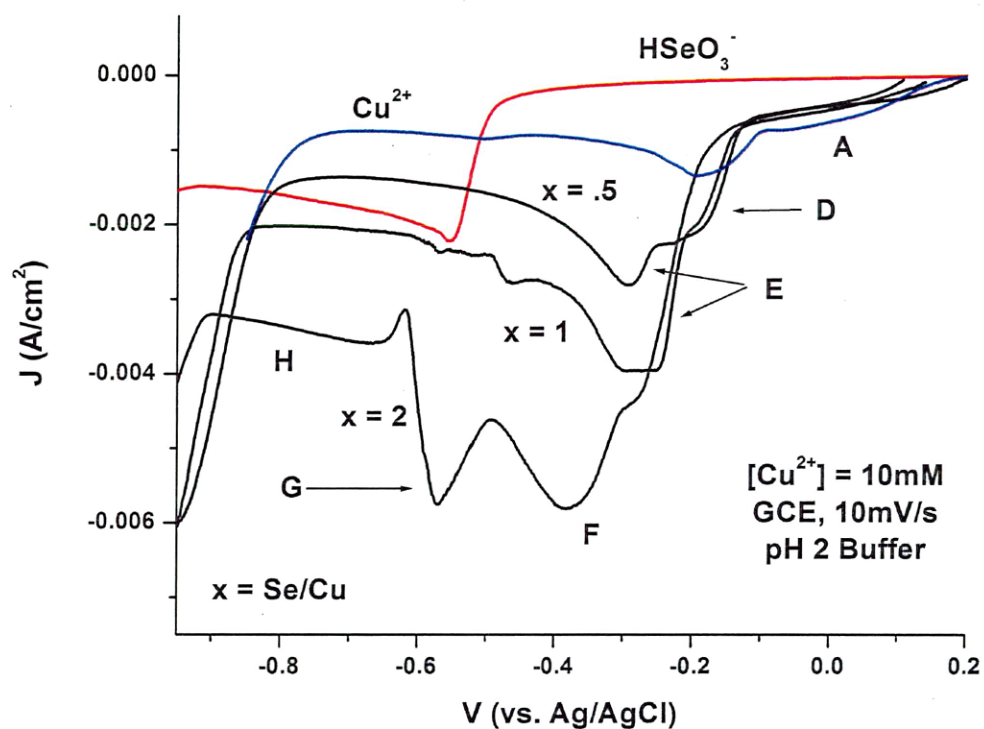
Figure 5.2 Voltammetry of solutions containing varying ratios of Se/Cu (x), showing the effect of increased selenium concentration on the reduction curves. Cu^{2+} and $HSeO_3^-$ baseline curves are shown for reference.

The behavior of the Se-Cu electrodeposition system has been well characterized in previous studies[7, 14, 15]. Initially, with a low Se/Cu ratio in solution, $Cu_{2-x}Se$ is formed (wave D). For clarity, this will be referred to in a

general form as Cu_2Se. With the addition of more selenium, this begins to change to CuSe (wave E), then Cu_3Se_2 (wave F), and with an excess of $HSeO_3^-$, Se^0 is also formed (wave G). An additional peak after the reduction of H_2SeO_3 into elemental Se is seen, corresponding to the reduction of elemental Se^0 to Se^{2-}, and the production of H_2Se (wave H). The observed reduction waves are explained in Equations (5.12) to (5.14).

$$A: \quad Cu^{2+} + 2e^- \rightarrow Cu^0$$
$$D: \quad (2-x)Cu^0 + HSeO_3^- + 4e^- + 5H^+ \rightarrow Cu_{2-x}Se + 3H_2O$$

$$(5.12)$$

$$E: \quad Cu_2Se + 4e^- + HSeO_3^- + 5H^+ \rightarrow 2CuSe + 3H_2O$$
$$F: \quad 3Cu_2Se + HSeO_3^- + 5e^- + 6H^+ \rightarrow 2Cu_3Se_2 + 3H_2O$$

$$(5.13)$$

$$G: \quad HSeO_3^- + 4e^- + 5H^+ \rightarrow Se^0 + H_2O$$
$$H: \quad Se^0 + 2e^- + 2H^+ \rightarrow H_2Se$$

$$(5.14)$$
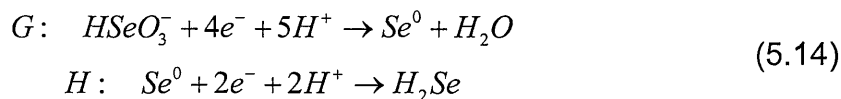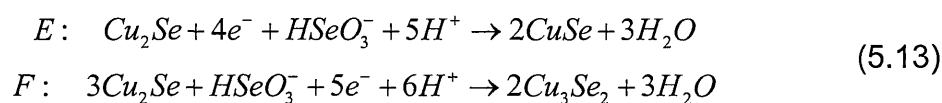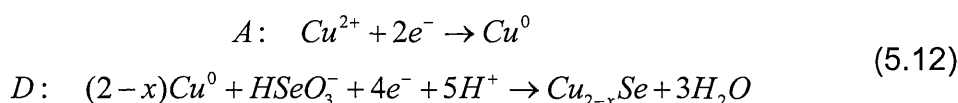
It can be seen that the onset of the deposition of the binary Cu_xSe_y compounds occurs at more noble potentials than that of the $HSeO_3^-$ reduction alone. Compound formation at more positive potentials indicates an alloy codeposition process is occurring, driven by the Gibbs energy of the alloy.

5.4.2 Ga-Se System

Figure 5.3 shows voltammograms of solutions containing increasing ratios of Ga/Se (z), with a $HSeO_3^-$ concentration of 10mM. The red curve shows the $HSeO_3^-$ reduction before the addition of Ga^{3+}.

128
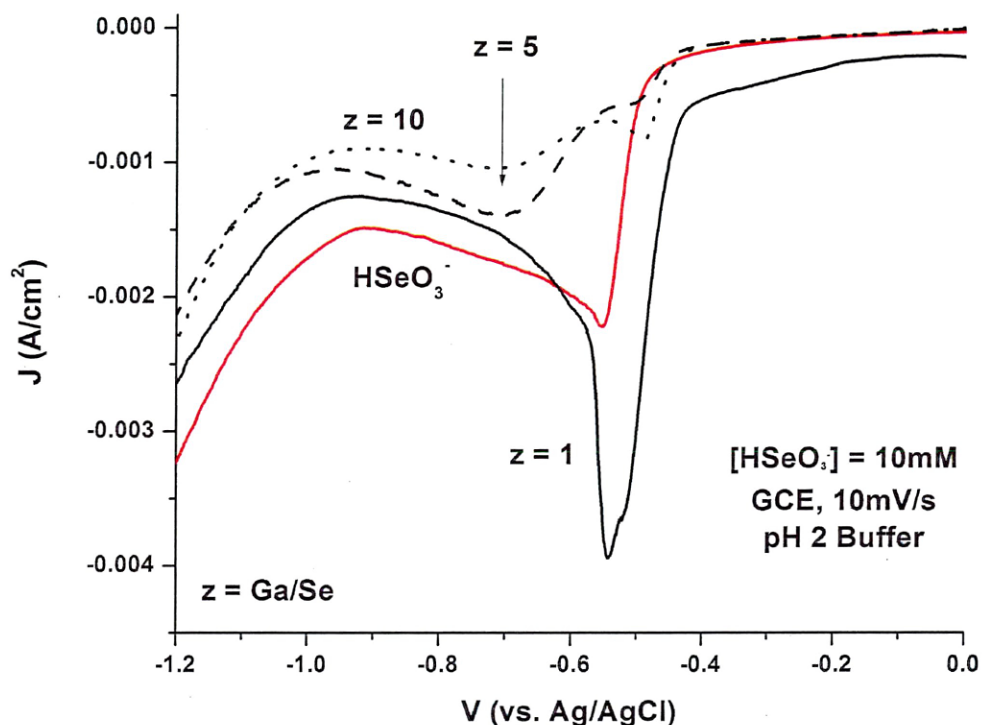
Figure 5.3 Voltammetry of solutions containing different Ga/Se ratios (z), showing the effect of increased Ga^{3+} concentration. The red curve shows the behavior of $HSeO_3^-$ before the addition of Ga^{3+}.

Initially, the addition of 10mM Ga^{3+} shows an increase in the current density associated with the Se^0 formation peak. This peak is likely the sum of the current density from both Se^0 formation and the formation of a Ga_xSe_y alloy occurring at a slightly more noble potential. As the $GaCl_3$ content of the solution is increased, the Ga_xSe_y peak becomes more apparent, and the sharp Se peak recedes. In the presence of excess Ga^{3+}, the $HSeO_3^-$ is reacting to form the

Ga_xSe_y alloy instead of Se^0. The addition of more $GaCl_3$ shows the Ga_xSe_y peak increasing in current density, indicating the formation of more compound due to more available reactant. The reduction wave after this compound formation is again due to the joint formation of Se^0 and subsequent reduction of Se^0 to H_2Se, or the direct reduction of $HSeO_3^-$ to H_2Se. More $HSeO_3^-$ is consumed in the Ga_xSe_y formation when more Ga^{3+} is added to solution, and the $HSeO_3^-$ reduction peak subsequently decreases. At this time the composition of the alloy is not known, however, one possible Ga_xSe_y alloy formation mechanism is seen in Equation (5.15) .

$$3HSeO_3^- + 2Ga^{3+} + 3H^+ + 3e^- \rightarrow Ga_2Se_3 + 3H_2O \qquad (5.15)$$
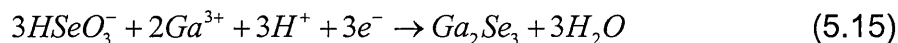
5.4.3 Cu-Ga System

The effect of the Ga^{3+} concentration on the voltammetry of 10mM Cu^{2+} solutions was examined at varying ratios of Ga/Cu (y), seen in Figure 5.4. The observed behavior of the Cu-Ga system can be explained by the interaction of Cl^- with Cu^{2+}. The source of the Cl^- in this case comes from the added $GaCl_3$ solution.
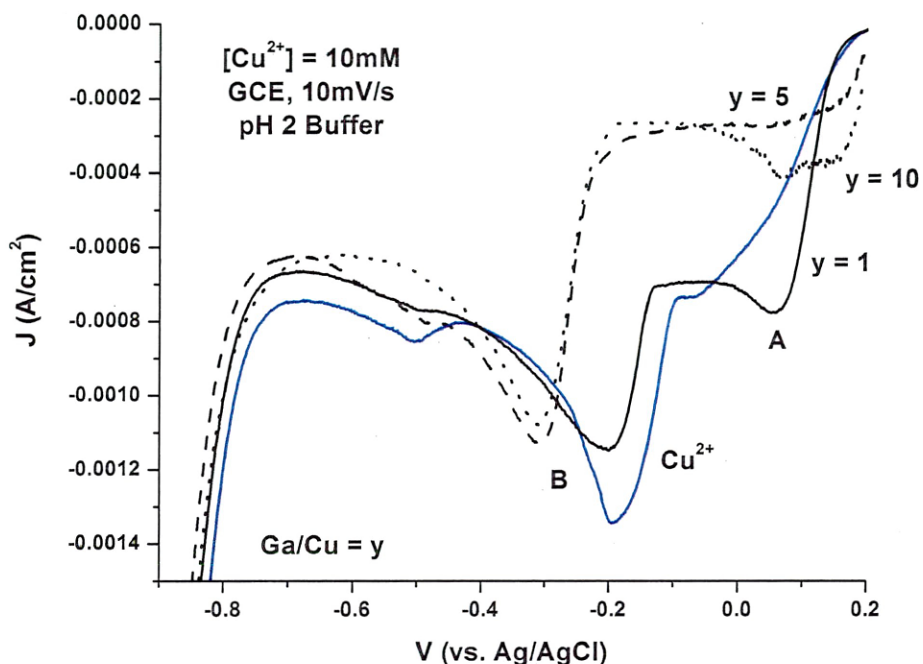
Figure 5.4 Voltammetry of solutions containing an increasing ratio of Ga/Cu (y). The addition of chloride ions from the GaCl$_3$ solution are seen to affect the copper deposition mechanisms.

It has previously been shown that the presence of Cl$^-$ ions in a Cu^{2+} bath acts to catalyze the deposition of Cu^0 through the mechanism seen in Equation (5.16), which leads to the deposition of an adsorbed CuCl compound. This compound then further reduces to Cu^0 at more negative potentials.

$$Cu^{2+} + Cl^- + e^- \rightarrow CuCl_{ads}$$
$$CuCl_{ads} + e^- \rightarrow Cu + Cl^-$$

(5.16)
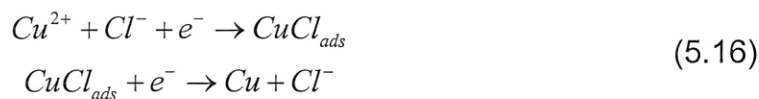
The initial increase in the Cu^{2+} > Cu^0 peak current density (wave A) arises from the activation of Cu^{2+} reduction by Cl$^-$ ions[16]. The peak decreases with the addition of an excess of Cl$^-$ that might shift the equilibrium of the above reactions

toward the formation of the adsorbed anion complex. The $Cu^{2+} > Cu^{1+}$ peak (wave B) shifts towards more negative potentials from the overpotential induced by concentration polarization of Cu^{2+} from the previous step. The similarity between the Ga = 5 and Ga= 10 peaks suggests a saturation effect of Cl^- ions on the Cu^0 activation.

5.4.4 Cu-Ga-Se System

Figure 5.5 shows voltammograms of solutions with Se/Cu = 1 upon the addition of $GaCl_3$ to the system. The addition of small amounts of gallium to the Cu/Se = 1 system show very little change in the voltammetric characteristics, with a small shift in the $Cu_{2-x}Se$ peak (wave E) toward more negative potentials. Upon the addition of larger amounts of Ga^{3+}, the Cu^{2+} reduction wave (A) increases due to chloride activation and the formation of a $CuCl_{ads}$ species. Wave F, associated with the reduction of CuSe, decreases in intensity at these higher Ga^{3+} concentrations. The formation of CuSe may be hindered by slow formation of Cu^0 from the adsorbed CuCl species. Wave F appears in solutions with a higher Ga^{3+} concentration, and likely pertains to the formation of a Ga_xSe_y alloy.

132
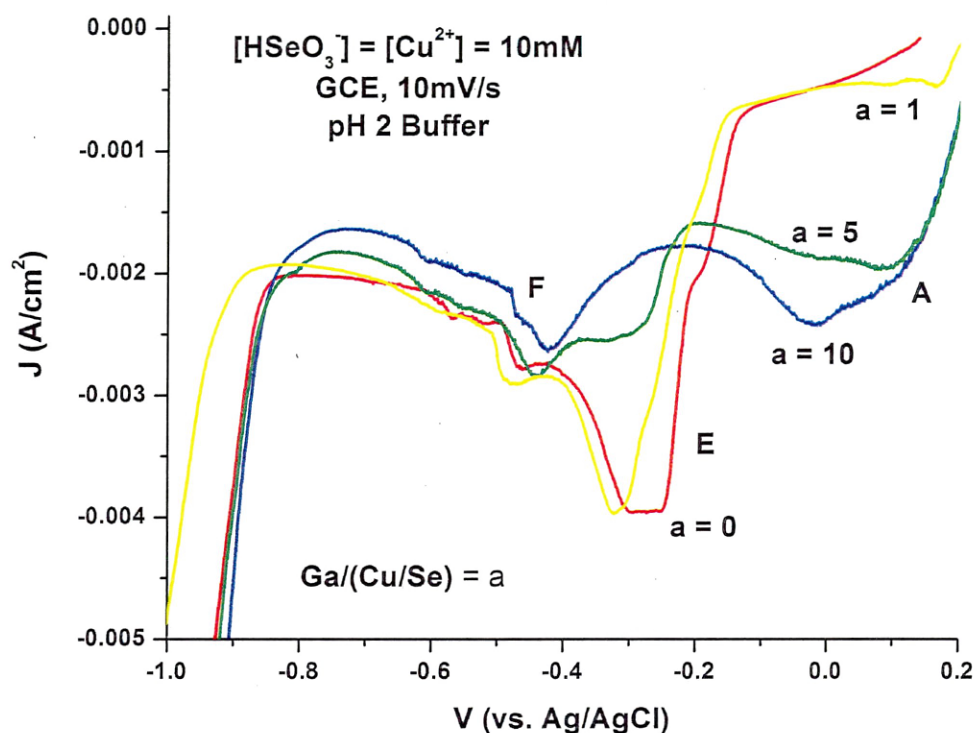
Figure 5.5 Voltammograms of 10mM solutions with a fixed Se/Cu ratio of 1. The amount of Ga^{3+} is increased from Ga/Se = 0 to 10.

5.4.5 Electrodeposition

Film electrodeposition was performed on both Mo and ITO coated glass substrates. Table 5.2 presents the concentrations and deposition conditions for the films prepared in this study. Not all potentials were examined for electrodeposition on each substrate. This is due to the observed hydrogen gas formation during depositions at more negative potentials, which caused the films to delaminate or prevented deposition entirely. At lower H_2SeO_3 concentrations, potentials more negative than -0.6V could not be used due to the large amount of

hydrogen evolution. With more selenium in solution, the production of hydrogen gas was suppressed at the electrode surface, and film deposition at more negative potentials could be achieved. In solutions with a higher H_2SeO_3 concentration, the formation of H_2Se according to Equation (5.17) prevented the evolution of H_2 gas bubbles at the surface, or at least decreased the quantity of evolved gas to enable the deposition of an adherent film.

$$H_2SeO_3 + 4H^+ + 4e^- \rightarrow Se^0 + 3H_2O$$
$$Se^0 + 2H^+ + 2e^- \rightarrow H_2Se$$

(5.17)
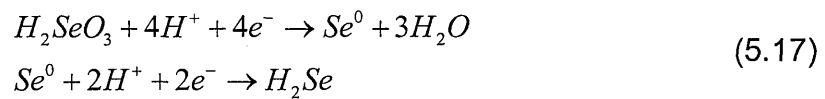
At more negative deposition potentials, ITO substrates were used instead of Mo. Molybdenum working electrodes showed a much earlier onset for H_2 gas evolution at their surfaces, and even with excess H_2SeO_3 in the deposition bath, H_2 production prevented film deposition. Clearly Mo has a lower overpotential for the hydrogen reaction than ITO. Reduction in the ITO possible begins with reducing the indium within the oxide film, delaying the onset of the H^+ reduction at the surface.

Table 5.2 The composition of deposition baths investigated for the given electrodeposition potentials. The chosen substrates for those parameters are shown. Ratios are given normalized to $[Cu^{2+}]$ = 10mM.

Cu:Ga:Se	-600mV	-700mV	-800mV	-900mV	-1000mV	-1100mV
1:10:0.5	Mo					
1:10:1	Mo					
1:10:1.5	Mo	Mo				
1:10:2	Mo	Mo	ITO	ITO	ITO	ITO

Voltammetry was performed on electrodeposition solutions using the same working electrode as the deposition substrate. These voltammograms were used to choose the deposition potentials for examination in this study. Figure 5.6 shows reduction curves at a Mo substrate of solutions containing Ga/Cu = 10 and $HSeO_3^-$ concentrations ranging from 5 – 20mM.
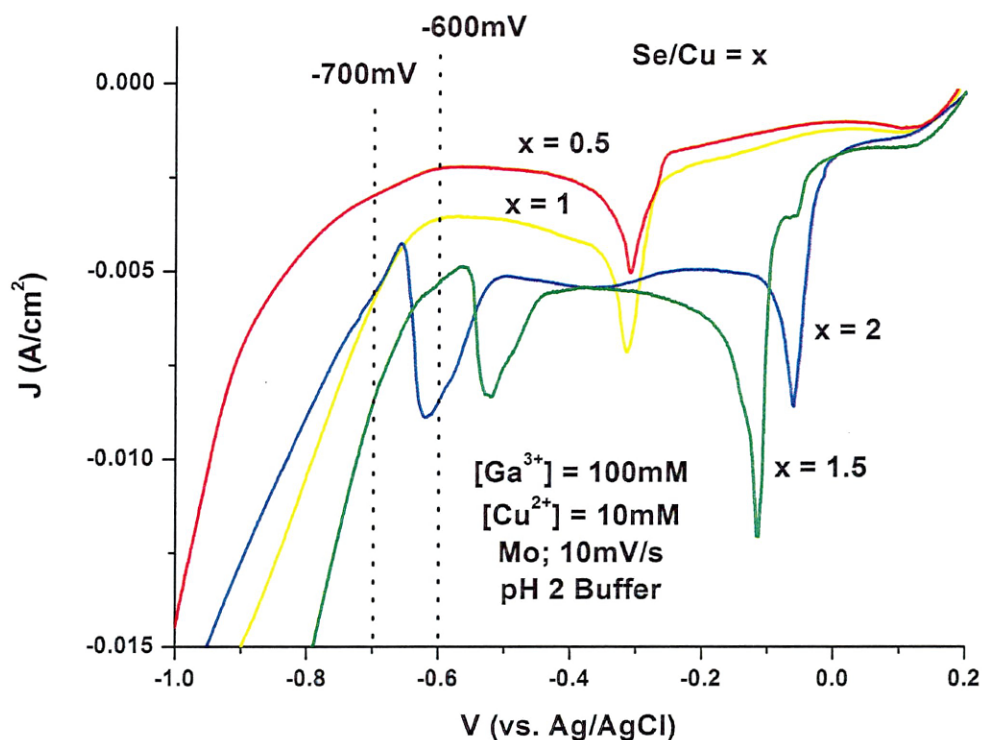
Figure 5.6 Voltammograms of deposition solutions containing Ga/Cu = 10, and varying amounts of Se. All scans were done using a Mo working electrode at 10mV/s.

Figure 5.7 shows a voltammogram of a deposition solution with a Cu:Ga:Se ratio of 1:10:2 using an ITO working electrode. It is seen that the onset of linear current corresponding to the reduction of H^+ into H_2 gas does not occur

until potentials around -1.2 V, far more negative than at the Mo working electrode. ITO provides a larger window of potentials for film depositions.
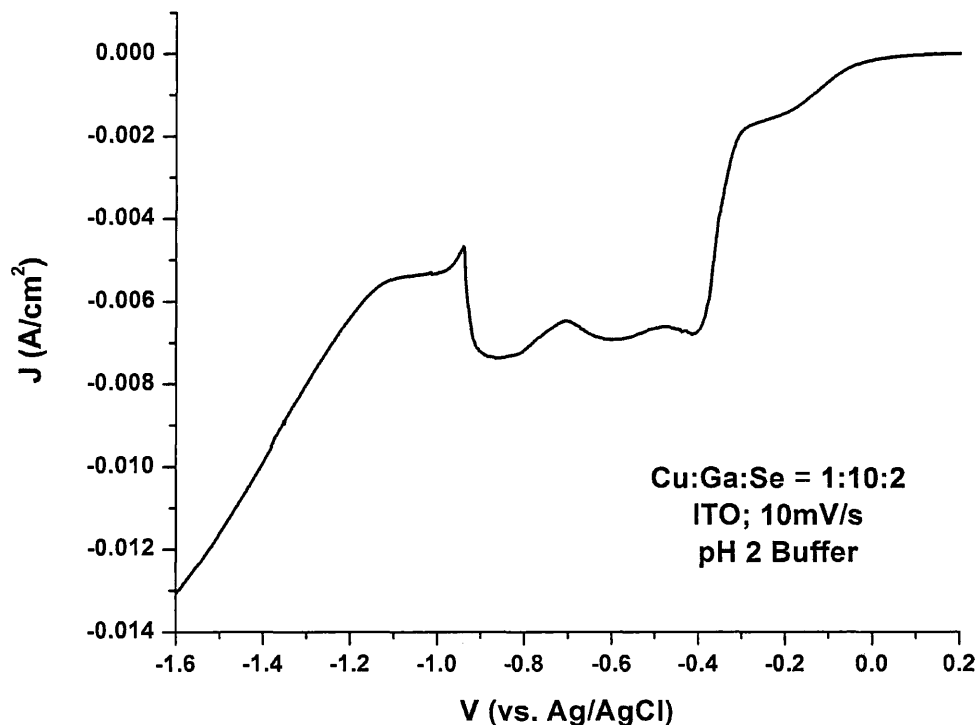
Figure 5.7 Voltammetry of a Cu:Ga:Se solution with a concentration ratio of 1:10:2 at an ITO working electrode, showing a delayed H^+ reduction onset.

The voltammograms at the Mo and ITO substrates exhibit different peak shapes and positions than those obtained at a glassy carbon electrode surface. Electrode kinetics are affected by the surface characteristics of the working electrode such as roughness, microstructure, and adsorbed species. Different working electrodes may have different overvoltages for the reactions in question.

Individual solutions were not studied at Mo and ITO working electrodes, and thus the actual reduction waves cannot be qualified. It is assumed that the peaks observed in these voltammograms correspond to the formation of Cu_xSe_y and possibly Ga_xSe_y alloys.

5.4.6 Microstructure

X-ray diffraction (XRD) measurements were performed on the electrodeposited films from the previous section. Table 5.3 lists the phases detected in the XRD patterns. All of the phases observed in the diffraction patterns were those of Cu_xSe_y, and no crystalline phases associated with Ga^0 or gallium containing alloys were found. Deposition from the solution with a Se/Cu ratio of 0.5 led to the formation of $Cu_{2-x}Se$. All other solutions with Se/Cu = 1.0 or higher led to the formation of CuSe, and those solutions with the higher Se/Cu ratio of 1.5 and 2 also showed the presence of Cu_3Se_2 in the deposited film. Figure 5.8 shows the XRD patterns from the as-deposited films on Mo glass at -600mV vs. Ag/AgCl. This figure shows that the solution concentration of $HSeO_3^-$ affects the phase of the Cu_xSe_y alloys observed in these films. No peaks associated with gallium alloys can be seen in these diffraction patterns.

137
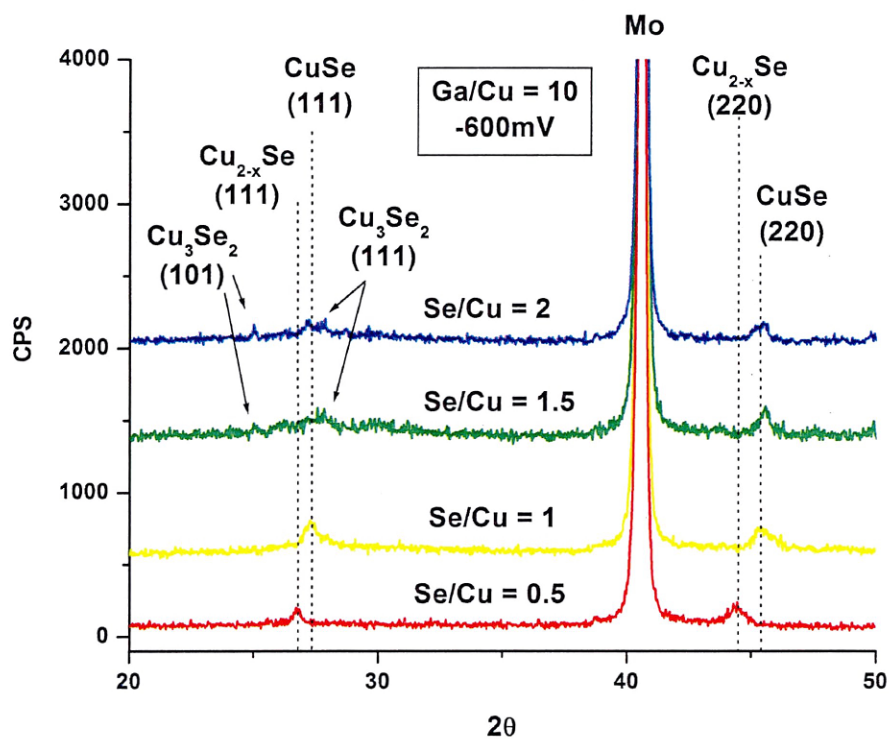
Figure 5.8 XRD patterns of films deposited from solutions with Ga/Cu = 10 and varying selenium concentrations. All depositions were done at -600mV vs. Ag/AgCl on Mo substrates.

Table 5.3 Phases present based on XRD measurements of electrodeposited films. The phase content is shown as a function of both the solution composition and the deposition potential. Solution composition shown normalized to $[Cu^{2+}]$ = 10mM.

	Phases Present in XRD Patterns					
Cu:Ga:Se	-600mV	-700mV	-800mV	-900mV	-1000mV	-1100mV
1:10:0.5	$Cu_{2-x}Se$					
1:10:1	CuSe					
1:10:1.5	CuSe, Cu_3Se_2	CuSe, Cu_3Se_2				
1:10:2	CuSe, Cu_3Se_2	CuSe, Cu_3Se_2	CuSe, Cu_3Se_2	CuSe, Cu_3Se_2	CuSe, Cu_3Se_2	CuSe

5.4.7 Composition of Electrodeposited Films

Electrodeposited films were analyzed by ICP/MS to determine the amount of Cu, Ga, and Se in the films. These values were converted to atomic percentages, shown in Table 5.4. Though XRD patterns did not indicate the presence of Ga^0 or gallium alloys, ICP measurements clearly indicate gallium incorporation was obtained in some of the electrodeposited films. This suggests that the gallium-containing phases are amorphous, or have a very small crystallite size. Annealing of these films may induce the growth of gallium-containing crystal phases.

139

Table 5.4 Film compositions resulting from different bath compositions and applied potentials. Compositions were determined by ICP-MS analysis.

Cu:Ga:Se	-0.6V	-0.7V	-0.8V	-0.9V	-1.0V	-1.1V

1:10:0.5

	-0.6V	-0.7V	-0.8V	-0.9V	-1.0V	-1.1V
Cu (%)	41.86					
Ga (%)	32.68					
Se (%)	25.45					

1:10:1

	-0.6V	-0.7V	-0.8V	-0.9V	-1.0V	-1.1V
Cu (%)	33.18					
Ga (%)	30.71					
Se (%)	36.11					

1:10:1.5

	-0.6V	-0.7V	-0.8V	-0.9V	-1.0V	-1.1V
Cu (%)	39.03	32.06				
Ga (%)	1.76	21.73				
Se (%)	59.22	46.21				

1:10:2

	-0.6V	-0.7V	-0.8V	-0.9V	-1.0V	-1.1V
Cu (%)	37.14	33.32	33.69	31.85	35.47	27.00
Ga (%)	0.84	1.15	2.00	0.87	1.12	18.27
Se (%)	62.02	65.52	64.31	67.28	63.41	54.72

Film depositions on Mo substrates were performed for four solution concentrations at -600mV vs. Ag/AgCl, and for the solutions with higher H_2SeO_3 concentrations at -700mV also. Figure 5.9 shows the film composition results as a function of the $HSeO_3^-$ solution concentration for those films deposited at -600mV on Mo. For a deposition potential of -600mV, solutions with higher H_2SeO_3 concentrations did not result in the deposition of gallium in the film. Depositions from solutions with lower H_2SeO_3 concentrations show the incorporation of gallium into the films, resulting in a compositional ratio greater than 30% determined by ICP. For the solution with Se/Cu = 1.5, gallium incorporation was achieved at the more negative potential of -700mV. Using the bath with the highest selenium concentration, -700mV was not enough to deposit gallium.

The film electrodeposited from Cu:Ga:Se = 1:10:1.5 at a potential of -700mV shows a film ratio of $CuGa_{0.7}Se_{1.4}$, closest to that of $CuGaSe_2$. Some films show very high amounts of gallium compared to the relative ratios found in $CuGaSe_2$. This may indicate that the deposition of gallium is not through the formation of the chalcopyrite compound, or may be through more than one mechanism.

141 ARTHUR LAKES LIBRARY
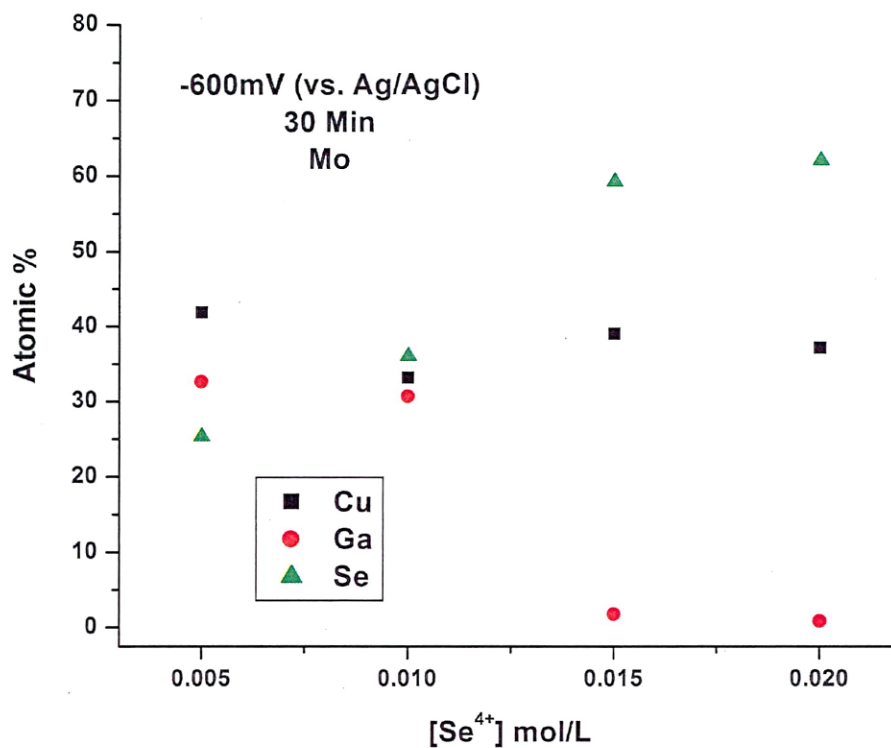
Figure 5.9 Electrodeposited film compositions as a function of $[Se^{4+}]$ in the deposition bath. All depositions were performed at -600mV vs. Ag/AgCl for 30min on Mo substrates.

A larger potential range for electrodeposition was examined for ITO substrates due to the suppression of H_2 gas evolution at more negative deposition potentials. Figure 5.10 shows the relative composition of films deposited from a deposition bath with Cu:Ga:Se = 1:10:2 as a function of the deposition potential. Sufficient gallium incorporation is not obtained from this bath until -1.1 V vs. Ag/AgCl. The reduction of gallium at this potential was likely the direct reduction of Ga^{3+} to Ga^0, resulting in metal deposition instead of compound formation. The quality of the deposition performed at this potential was poor due to the hydrogen evolution reaction.
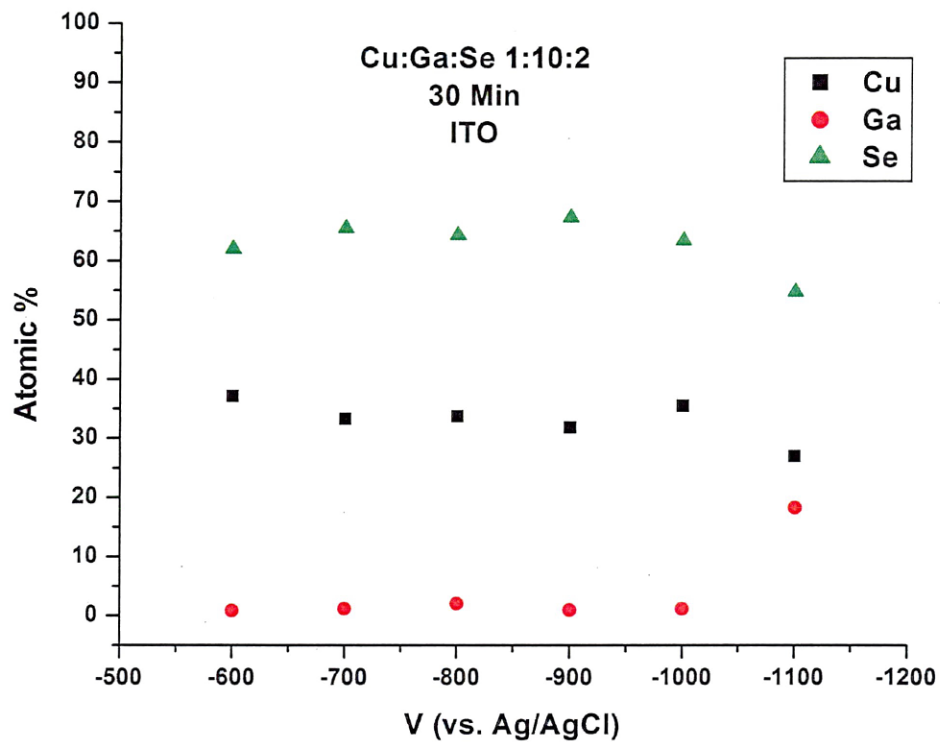
Figure 5.10 Relative film compositions as a function of deposition potential. Films were deposited from baths with Cu:Ga:Se = 1:10:2

The ICP results suggest that there may be several processes involved with the incorporation of gallium into these films. The first may proceed via a chemical reaction involving the formed Cu_2Se binary alloy, seen in Equation (5.18).

$$2Cu_2Se(s) + Ga^{3+}(aq) \rightleftharpoons CuGaSe_2 + 3Cu^+ \tag{5.18}$$

In solutions with more Se, the reaction of Cu_2Se with $HSeO_3^-$ competes with the reaction of Cu_2Se with Ga^{3+}. This may be why films deposited at more positive potentials from solutions with higher $[HSeO_3^-]$ showed no gallium incorporation.

The second method of gallium incorporation may be through the formation of a binary Ga_xSe_y compound. The formation of this alloy was observed in voltammetric studies of Ga^{3+}- H_2SeO_3 solutions. Results suggest kinetics may limit or dictate the formation of this alloy. There is a competition with Cu^{2+} and Cu_xSe_y for the reaction with $HSeO_3^-$ versus the reaction of $HSeO_3^-$ with Ga^{3+}. The kinetically favored reaction will occur at a faster rate. Depending on the solution concentration, both may occur simultaneously, or one may occur only after the subsequent depletion and concentration polarization of the competing reactants. Examining the diffusion coefficients in Table 5.1, it is seen that Ga^{3+} has the lowest mobility in solution. This may create a mass transport limitation resulting in the preferred Cu_xSe_y reactions rather than Ga_xSe_y formation.

The third reaction simply involves the reduction of Ga^{3+} according to Equation (5.2). This is the likely mechanism for the deposition of gallium from the solution with a Cu:Ga:Se ratio of 1:10:2, where potentials of -1.1V were needed to incorporate gallium into the films. It has been reported elsewhere that gallium reduction from aqueous acid solutions occurs around -1.1 V vs. Ag/AgCl[17].

5.5 Conclusions and Future Work

The wide variations in the reduction potentials of Cu^{2+}, Ga^{3+}, and $HSeO_3^-$ make the one-step electrodeposition of $CuGaSe_2$ difficult. In this work, the

incorporation of gallium into $Cu_xGa_ySe_y$ thin films was achieved, however non-stoichiometry in these films was observed. Stoichiometric films are necessary to avoid further synthesis steps which increase overall deposition cost and energy intensity. XRD revealed the presence of Cu_xSe_y phases in the electrodeposited films, however no crystalline phases associated with Ga^0 or gallium compounds were seen in the as-deposited films. This suggests that the Ga-containing phases in these electrodeposited films are amorphous, or have a very small crystallite size.

Substrate effects, solution composition, and applied potential are all very important factors in the electrodeposition process. The chosen substrate for electrodeposition affects the H_2 deposition rate and potential, which inhibits film deposition. Solution pH also plays a very important role in H_2 production at the electrode surface, and the interplay between ion precipitation and suppression of the H_2 reaction is difficult to balance.

The solution concentration ratios of Se/Cu affected both the film composition and microstructure. Films deposited from baths containing larger Se/Cu ratios required more overpotential to deposit gallium. Electrodeposition of alloy materials proceeds through several stages. For the $CuGaSe_2$ alloy system, the deposition of Cu_xSe_y competes with the deposition of Ga_xSe_y.

These results suggest that though the formation of a Ga_xSe_y alloy may be thermodynamically controlled, with reaction kinetics dictating the deposition of gallium. The reaction of selenium with copper is kinetically favored over that of selenium with gallium. The slow diffusion of gallium in the deposition bath may inhibit the reaction kinetics, even in baths with high gallium concentrations. Higher solution concentrations of selenium react with copper at more positive

145

potentials, and do not lead to gallium deposition until sufficient reductive conditions are achieved. Films deposited from baths with lower Se/Cu ratios had a higher gallium content, even when deposited at more noble potentials. The ability to deposit films at more positive potential leads to better film quality because of reduced hydrogen generation.

Deposition baths with a high Ga^{3+} concentration and low Se/Cu ratios are recommended for additional electrodeposition investigation. Further work in electrodepositing $CuGaSe_2$ films should include investigation of complexing agents such a SCN^- that are known to strongly complex Cu^{2+}, but weakly bind gallium and selenium to bring the deposition potentials closer together. Additional substrates with high hydrogen reduction overpotential, such as fluorine-doped tin oxide, may make depositions from acidic solutions at more negative potentials possible. Annealing of films with stoichiometry close to the preferred $CuGaSe_2$ should be performed to investigate the possible formation of a Ga-containing chalcopyrite phase.

Further possibilities for understanding the mechanism of formation of these compounds could employ the use of electrochemical quartz crystal microbalance studies (EQCM). Monitoring the mass changes at the reacting electrode surface will better elucidate what reduction processes are occurring at which potentials.

REFERENCES

1. M.A. Contreras, J. Tuttle, A. Gabor, A. Tennant, K. Ramanathan, S. Asher, A. Franz, J. Keane, L. Wang, and R. Noufi, High Efficiency Graded Bandgap Thin-Film Polycrystalline Cu(In,Ga)Se$_2$-Based Solar Cells. *Solar Energy Materials & Solar Cells* **41/42**, p. 231-246 (1996).

2. M.A. Green, Solar Cells: Operating Principles, Technology, and System Applications. 1982, Kensington: University of New South Wales.

3. D. Lincot, J.F. Guillemoles, S. Taunier, D. Guimard, J. Sicx-Kurdi, A. Chaumont, O. Roussel, O. Ramdani, C. Hubert, J.P. Fauvarque, N. Bodereau, L. Parissi, P. Panheleux, P. Fanouillere, N. Naghavi, P.P. Grand, M. Benfarah, P. Mogensen, and O. Kerrec, Chalcopyrite Thin Film Solar Cells by Electrodeposition. *Solar Energy* **77** (6), p. 725-737 (2004).

4. A.J. Bard, R. Parsons, and J. Jordan, Standard Potentials in Aqueous Solution, ed. IUPAC. 1985, New York: Marcel Dekker, Inc.

5. M. Paunovic and M. Schlesinger, Fundamentals of Electrochemical Deposition. 1998, New York: John Wiley and Sons, Inc.

6. A.J. Bard and L.R. Faulkner, Electrochemical Methods: Fundamentals and Applications. 1980, New York: John Wiley and Sons.

7. S. Massaccesi, S. Sanchez, and J. Vedel, Cathodic Deposition of Copper Selenide Films on Tin Oxide in Sulfate Solutions. *Journal of the Electrochemical Society* **140** (9), p. 2540-2546 (1993).

8. S. Kariuki and H.D. Dewald, Diffusion Coefficients of Gallium(III) in Potassium Nitrate and Potassium Chloride Supporting Electrolytes. *Electroanalysis* **9** (3), p. 231-234 (1997).

9. M. Kemell, H. Saloniemi, M. Ritala, and M. Leskela, Electrochemical Quartz Crystal Microbalance Study of the Electrodeposition Mechanisms of CuInSe$_2$ Thin Films. *Journal of the Electrochemical Society* **148** (2), p. C110-C118 (2001).

10. K.K. Mishra and K. Rajeshwar, A Voltammetric Study of the Electrodeposition Chemistry of the Cu+In+Se System. *Journal of Electroanalytical Chemistry* **271**, p. 279-294 (1989).

11. L. Thouin, S. Massaccesi, S. Sanchez, and J. Vedel, Formation of Copper Indium Diselenide by Electrodeposition. *Journal of Electroanalytical Chemistry* **374** (1-2), p. 81-88 (1994).

12. A. Brenner, Electrodeposition of Alloys. Vol. 1. 1963, New York: Academic Press.

13. F.A. Kroger, Cathodic Deposition and Characterization of Metallic or Semiconducting Binary Alloys or Compounds. *Journal of the Electrochemical Society* **125** (12), p. 2028-2034 (1978).

14. M. Kemell, M. Ritala, H. Saloniemi, M. Leskela, T. Sajavaara, and E. Rauhala, One-Step Electrodeposition of $Cu_{2-x}Se$ and $CuInSe_2$ Thin Films by the Induced Co-Deposition Mechanism. *Journal of the Electrochemical Society* **147** (3), p. 1080-1087 (2000).

15. L. Thouin and J. Vedel, Electrodeposition and Characterization of $CuInSe_2$ Thin-Films. *Journal of the Electrochemical Society* **142** (9), p. 2996-3001 (1995).

16. C. Gabrielli, P. Mocoteguy, H. Perrot, and R. Wiart, Mechanism of Copper Deposition in a Sulphate Bath Containing Chlorides. *Journal of Electroanalytical Chemistry* **572**, p. 367-375 (2004).

17. L. Gheorghies and C. Gheorghies, Preparation of GaAs Thin Films from Acid Aqueous Solution. *Journal of Optoelectronics and Advanced Materials* **4** (4), p. 979-982 (2002).

CHAPTER 6

SUMMARY AND CONCLUSIONS

In this dissertation, studies on the properties of $Cu(In_{1-x}Ga_x)(Se_{1-y}S_y)_2$ (CIGSS) thin film semiconductors and their application to photoelectrochemical (PEC) hydrogen production are described. Several criteria for PEC materials must be met, the most important of which are band gap, band edge positions, and corrosion characteristics. The CIGSS material system was identified as a potential material for this application due to its large band gap range, high photovoltaic (PV) efficiencies, and potential low-cost deposition pathways.

Results in Chapter 2 show that it is possible to prepare CIGSS thin films via the use of electrodeposited precursor materials. The compositions of these electrodeposited precursors were controlled using physical vapor deposition (PVD). The mechanism of compositional adjustment occurs via diffusion at the interface of the precursor and the condensed PVD layer. Multiple phases were observed in some films as a result of stoichiometric differences between precursor materials and the evaporated PVD layer. Longer annealing times and higher temperatures may allow for homogenization of the films. This technique is promising for low-cost fabrication, eliminating many steps in the typical high temperature, high vacuum vapor deposition process.

Chapter 3 described the development of an empirical equation describing the band gap in the CIGSS system based on gallium and sulfur alloying. Using values for bowing coefficients and end-point band gaps reported in literature, this equation was used to predict the band gap of this semiconductor system from knowledge of the alloy composition. This also provides a way to choose a desired band gap or band gap range, and determine the needed alloy

composition required to achieve this value. This equation was then applied to synthesized materials described in Chapter 2, which show a varying alloy composition through the depth of the films. This changing alloy composition results in a changing band gap value through the depth of the material. This is an example of band gap grading; a technique used in PV systems to increase efficiencies, but has never been applied to PEC systems.

Materials described in Chapter 2 have a band gap profile that differs based on the enrichment scheme. Materials prepared in a Ga_2S_3-containing atmosphere show high surface band gap values which decrease through the material toward the back contact. These films exhibited a high and low band gap value in photocurrent spectroscopy measurements, which resulted from inhomogeneous alloying during film preparation. Band gap grading could be a useful technique for increasing efficiencies and tailoring band energetics in PEC systems.

To address the issue of non-ideal band edge alignment, tandem photoelectrodes were prepared, as described in Chapter 4. First, the theoretical efficiencies of $CuGaSe_2$/ITO/Si PV and PEC materials were calculated for both air mass (AM) 0 and AM 1.5 radiation. The theoretical maximum solar-to-hydrogen conversion efficiency for this PEC device was predicted to be 25.4% at AM 1.5. Tandem cells were then fabricated via vapor deposition of $CuGaSe_2$ thin films on ITO/p-n Si substrates. Difficulties with the $CuGaSe_2$ morphology were encountered, which caused dissolution of the tunnel junction, leading to poor device characteristics. This is likely due to incompatibility of the multiple layers during the high temperature deposition techniques. Band edge positions in $CuGaSe_2$ single electrodes show values that are about 500 - 700 mV too far negative of the water oxidation potential, however the tandem photoelectrodes

show band edges in the proper position for water splitting due to the added internal bias from the Si PV junction. To determine the optimum corrosion characteristics, thin film $CuGaSe_2$ electrodes on molybdenum-coated glass were investigated, and Cu, Ga, and Se were found in the corrosion solution. Surface oxide dissolution is predicted to be one source of these elements. Cathodic protection was found in these single absorber materials, with a large reduction in oxidation current upon illumination. These are promising results for the stability of these materials.

Finally, the electrodeposition of $CuGaSe_2$ thin films was investigated and described in Chapter 5 as a potential low-temperature deposition technique for the top layer in tandem devices. The deposition of $Cu_xGa_ySe_z$ films on both molybdenum and indium-doped tin-oxide (ITO) substrates was performed, however the chalcopyrite crystal structure was not observed. The ability to incorporate gallium into these thin films via electrodeposition can be coupled with a post-deposition annealing and crystallization step, which is nevertheless a low-cost and lower-temperature route to $CuGaSe_2$ thin film fabrication. These results demonstrate the possibility of a more economical fabrication method of tandem $CuGaSe_2$/ITO/Si electrodes for PEC water splitting.

The results presented in this dissertation pertain to both the PV and PEC uses of $CuInSe_2$-based thin film semiconductors. The synthesis technique using electrodeposited precursors can be used for the fabrication of both PV and PEC devices containing sulfur and gallium. The calculation of band gap profiling is important for both areas of work, and will enable better understanding of band gap grading and its application to device efficiency. Tandem devices using $CuGaSe_2$ show high theoretical conversion efficiencies for both PV and PEC

devices. The top layer in these devices also shows promising electrochemical stability.

Cu(In,Ga)(Se,S)$_2$ materials do not have the proper band alignment for spontaneous PEC water splitting. Using these materials in a tandem device is the most promising technique for a PEC system without an external applied bias. Coupling this knowledge with the presented electrodeposition techniques and graded band gap profiles could provide a high efficiency, low-cost tandem device for PEC water splitting.

Further work on this material system should include a better understanding of band edge behavior at the semiconductor/electrolyte interface. Using the developed grading equation, semiconductors with different gallium and sulfur ratios giving rise to the same band gap can be fabricated. Then, the effect of these elements on the band positions and corrosion characteristics can be quantified. The fabrication of tandem systems using different interconnects will be important for material stability, and possibilities are fluorine-doped tin oxide (FTO), ZnO, and other transparent conducting oxides. The determination of ohmic or Schottky contact will be important in choosing the proper tunnel junction as well. A better understanding of the corrosion of CuGaSe$_2$ will be necessary, including that in acid and basic conditions. Overall, it is recommended that tandem devices using CIGSS alloys continue to be investigated for application in PEC water splitting, with the potential for a high efficiency, stable, low-cost system.

For applications and devices using semiconductor materials, electrical contact must be made to the semiconductor. Common semiconductor interfaces include those with a metal (Schottky junction), with another semiconductor (p-n junction), or with an electrolyte. Schottky junctions are the simplest semiconductor interface, and many of these properties extend to the description of the semiconductor/electrolyte interface.

Semiconductor Physics

Current flow in a semiconductor arises from the movement of conduction band electrons and valence band holes (or electron vacancies). In a semiconductor at T = 0K, when the conduction band is completely empty and the valence band is completely filled, there is no flow of charge carriers. A vacancy must be introduced to allow electron movement. At higher temperatures, some vacancies in the valence band are introduced allowing hole movement, and those electrons now occupying higher energy levels can move within the conduction band.

The chemical potential of electrons in a semiconductor is known as the Fermi Level (E_f). The Fermi-Dirac distribution function (Equation (1)) is used to describe the average distribution of electrons in the energy levels within a semiconductor, where E_F is the Fermi level, and E is the energy of the conduction band or valence band.

$$f(E) = \frac{1}{1 + \exp\left(\dfrac{E - E_F}{kT}\right)} \tag{1}$$

The number of allowed energy states in a semiconductor is zero within the band gap and non-zero at energies in the bands. This distribution of allowed energy states per unit volume is known as the density of states. The density of states for the conduction (N_C) and valence band (N_V) are defined by Equation (2), where m_e is the effective mass of electrons, and m_h is the effective mass of holes in the semiconductor[2].

$$N_C = \frac{2(2\pi m_e^* kT)^{3/2}}{h^3}$$

$$N_V = \frac{2(2\pi m_h^* kT)^{3/2}}{h^3}$$

(2)

If one knows the density of allowed states, and the probability of these states being occupied by electrons (given by the Fermi-Dirac distribution), then the actual distribution of electrons in the energy band of the semiconductor can be found. The total number of electrons in the conduction band (n) and the total number of holes in the valence band (p) can be found using Equation (3).

$$n = N_C e^{(E_V - E_F)/kT}$$

$$p = N_V e^{(E_F - E_C)/kT}$$

(3)

In an ideal semiconductor, the number of holes in the valence band and the number of electrons in the conduction band are equal, since every electron leaving the valence band leaves a hole behind. This is known as the intrinsic concentration of electrons (n_i). Using this model of a perfect semiconductor, it can be shown that the Fermi level lies in the middle of the band gap, seen in Equation (4).

$$n = p = n_i$$

$$np = n_i^2 = N_C N_V e^{-\left(\frac{E_C - E_V}{kT}\right)} \tag{4}$$

$$= N_C N_V e^{-\left(\frac{E_g}{kT}\right)}$$

The electronic properties of semiconductors are often modified by the introduction of impurity atoms into the crystal structure, a process known as doping. These impurity atoms can act to donate electrons to the conduction band of the semiconductor (donors), or to withdraw electrons from the valence band (acceptors). A material that is doped with electron donors is known as an n-type semiconductor, and that doped with acceptors a p-type semiconductor. The amount of donors or acceptors added to the semiconductor is in large excess than that of the intrinsic electron and hole concentrations. The doping densities of donors and acceptors are referred to as N_D and N_A, respectively.

In a p-type semiconductor the Fermi level is located in the band gap near the valence band, whereas in an n-type semiconductor, the Fermi level is located just below the conduction band. The location of the Fermi level can be quantified if the doping density and the effective density of states for the semiconductor are known. Equation (5) shows the difference between the Fermi level and the conduction or valence band for n or p type semiconductors, respectively. N_D and N_A are the donor and acceptor densities, respectively, and N_C and N_V are the density of states for the conduction and valence band[1].

$$E_F - E_c = kT \ln \frac{N_D}{N_C}$$

$$E_V - E_F = kT \ln \frac{N_A}{N_V} \tag{5}$$

Electrode/Electrolyte Interface

The electrode/electrolyte interface displays capacitance behavior. The interface consists of an assortment of oriented dipoles and charged ions which make up what is called the Electrical Double Layer (EDL). On the solution side of the interface there are several layers, one that is closest to the electrode surface, and one that extends into the solution bulk. The inner layer closest to the electrode surface is known as the Helmholtz layer, and consists of specifically adsorbed solvent and other ions in the solution. The Inner Helmholtz plane (IHP) is defined by the electrical center of these specifically adsorbed ions. Ions in the solution can only approach the electrode surface up to a certain distance due to their salvation. The plane of charges defined by these nearest solvated ions defines the Outer Helmholtz Plane (OHP). Ions in the OHP are non-specifically adsorbed, and constitute the diffuse layer, which extends from the OHP into the solution bulk. The structure and charge within the double layer can affect the rate of electron transfer across the electrode/electrolyte interface.
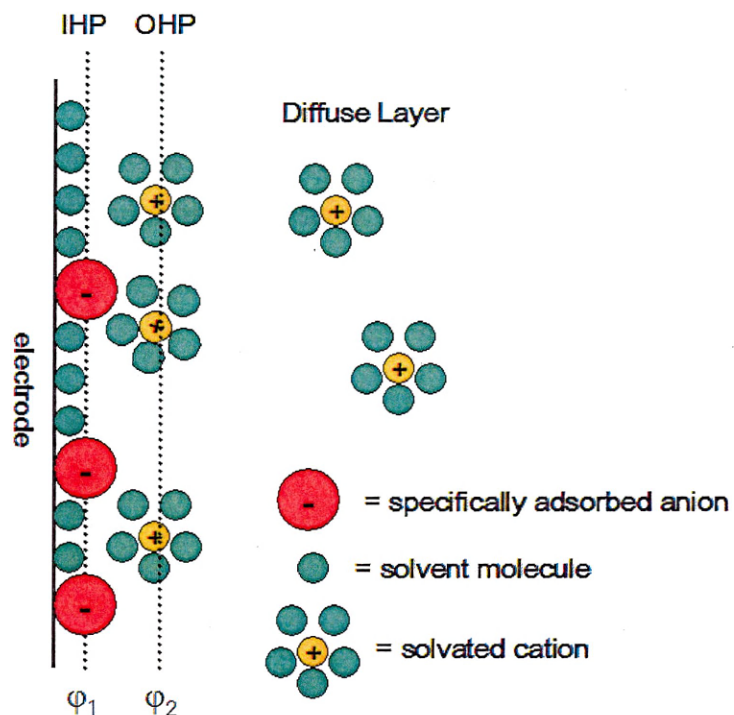
Figure 1. Illustration of the Electrical Double Layer (EDL) formed at the electrode/electrolyte interface. IHP and OHP are the boundaries of the Inner and Outer Helmholtz Planes, respectively. After Ref. [3].

Space charge layer

When two phases with different chemical potentials are interfaced, charge transfer occurs in order to establish thermodynamic equilibrium. In a liquid electrolyte, the chemical potential is equivalent to that of the redox couple in solution. The chemical potential of an ion in an ideal solution can be related to its concentration by Equation (6) where a_i is the activity of ion I, and μ^0 is the standard chemical potential for $a = a^0$.

157

$$\mu_i = \mu_i^0 + RT \ln\left(\frac{a_i}{a_i^0}\right)$$

(6)

in very dilute solutions, the activity of the ion is assumed to be equal to the concentration, however, in the presence of other ions and in concentrated solutions, this assumption does not necessarily hold true, and ion-ion interaction and ion-solvent interaction can play a role in activity[4].

For a redox system of $\mathrm{Re}d \Leftrightarrow Ox + e^-$, the electrochemical potential of the system (μ_{redox}) is defined by Equation (7).

$$\mu_{redox} = \mu_{red} - \mu_{ox}$$

$$\mu_{redox} = \mu_{red}^0 - \mu_{ox}^0 - RT \ln\left(\frac{a_{ox}}{a_{red}}\right)$$

(7)

To find the Fermi level, the units of electrochemical potential (joule mole^{-1}) must be converted to electron volts (eV) by Equation (8), which is then applied to Equation (7) [2].

$$E_{F,redox} = \left(\frac{e}{F}\right)\mu_{redox}$$

$$E_{F,redox} = E_{F,redox}^0 - kT \ln\left(\frac{a_{ox}}{a_{red}}\right)$$

(8)

When the semiconductor and electrolyte are put into contact under equilibrium conditions, $E_F = E_{F,redox}$. This equilibration leads to a potential difference across the interface, and electrons can be transferred from the phase with the higher Fermi potential (closer to the vacuum) to the phase with the lower Fermi potential.

158

In a metal electrode, the density of charge carriers is very high, and counter charges to the electrical double layer are located just below the electrode surface. In a semiconductor, the conductivity is based on dopants that contribute charge carriers to the material whose concentration is much lower than that for metals. Thus, the counter charge in a semiconductor is spread out below the electrode surface. The depth of counter charge into the material from the surface is known as the space charge layer or depletion layer in the semiconductor, and possesses a potential distribution and corresponding electric field. The potential of this electric field as a function of distance into the semiconductor electrode is described by Equation (9), where ϵ_s is the static dielectric constant of the semiconductor, and w_d is the width of the depletion layer[5].

$$E(x) = \left(\frac{qN_A}{\varepsilon_s} \right) \cdot \left(w_d - x \right) \quad \left(0 \leq x \leq w_d \right) \tag{9}$$

This shows that the maximum potential of the electric field lies at x = 0, or the semiconductor surface. This space charge layer and the electric field associated with it contributes to the separation of charge carriers in the semiconductor material.

When a p-type semiconductor is interfaced with an electrolyte, and the electrolyte Fermi level lies in the middle of the semiconductor band gap, then holes are transferred to the electrolyte to establish equilibrium. This creates band bending within the depletion layer driving electrons to the surface, seen in Figure 2. When an n-type semiconductor is interfaced with an electrolyte, electrons are transferred to solution and band bending occurs driving electrons to the bulk. This band bending and the resulting electric field is the basis for important electrical properties making this interface useful for photoelectrochemical applications.

159

When the semiconductor/electrolyte interface is illuminated, electrons are excited from the valence band to the conduction band in the semiconductor. The space charge region and the resulting electric field within the semiconductor serves to separate the electron-hole pairs. In a p-type semiconductor, electrons diffuse toward the electrolyte interface, and holes toward the back contact. In an n-type semiconductor, the opposite occurs in the presence of the electric field. Recombination of the electron-hole pair occurs if diffusion to the depletion region is not fast enough to separate the charge carriers.
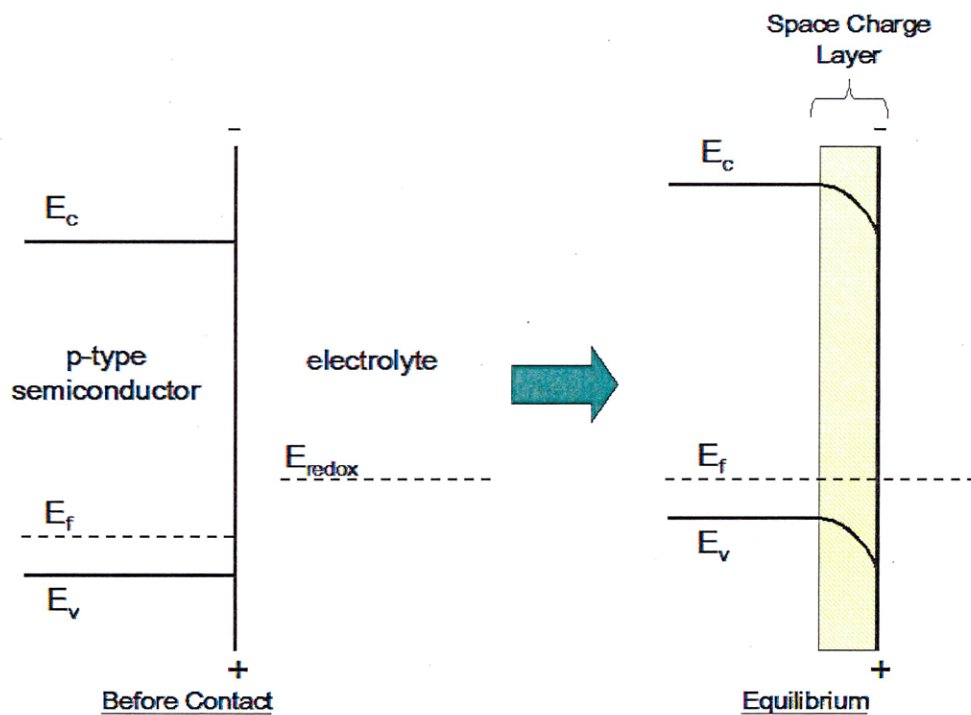
Figure 2. Band bending occurring at the semiconductor/electrolyte interface, showing the creation of the space charge region adjacent to the electrode surface.

Adsorbed ions from the solution also create a potential drop in the electrolyte adjacent to the interface through charging of the Helmholtz layer, shown above. The charge on the inner Helmholtz plane adjacent to the semiconductor surface is what dictates the band edge positions of the semiconductor when interfaced with solution. In many semiconductors, it is reported that H^+ and OH^- are the dominant adsorbed species at the surface of the semiconductor[6]. These species create a pH dependent charge at the interface, and thus a pH dependent value of the valence and conduction band edge positions, often following a Nernstian behavior.

Reactions under Illumination

When photo-generated carriers are pushed to the semiconductor surface under the influence of the depletion layer, they can then be transferred to the electrolyte to perform redox reactions. At the surface of an n-type semiconductor holes perform oxidation, whereas reduction occurs at the surface of p-type semiconductors.

Electron transfer at an electrode/electrolyte interface can be thought of during reduction as the transfer of electrons from the electrode into vacant electronic states within the electrolyte. Oxidation can be thought of as transfer of electrons from the electrolyte to vacant electronic states within the electrode. Reduction processes involve the conduction band in a semiconductor, and oxidation involves interaction with holes in the valence band.
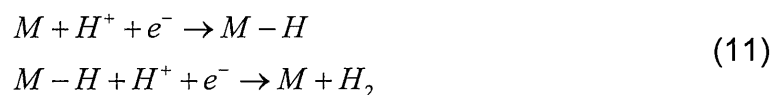
Flat Band Potential

It is of great interest to determine the actual value of the band edge positions at the interface. The valence and conduction band energetic positions will determine what reactions can occur across the interface. As we have seen, the bands are bent

throughout the space charge region. The band position at the interface is fixed by the charge in the inner Helmholtz layer, a process called band edge pinning. The position of the energy bands at the interface is found by determination of the flat band potential (E_{fb}), which is the value of the Fermi level when the bands are flattened. The flat band potential of a semiconductor is found when there is no difference between the band energies in the bulk of the semiconductor and at the surface of the semiconductor (the potential drop within the space charge layer is zero, i.e. there is no electric field). Knowing the E_{fb} of the Fermi level, and the doping density of the semiconductor, the band edge positions of the semiconductor at the interface can be determined using Equation (5). This gives a reference for the determination of possible surface reactions, such as the water redox reactions of interest in this dissertation, or even potential corrosion reactions.

Water Electrolysis

Many mechanisms have been suggested for the adsorption and decomposition of water at the surface of a metal or semiconductor material. On metal electrodes, there are two proposed pathways for the cathodic evolution of hydrogen. Equation (10) shows a charge transfer step, followed by what is known as a chemical desorption step. Equation (11) shows this same charge transfer step, followed by an electrochemical desorption step[4].

$$
\begin{aligned}
M + H^{+} + e^{-} &\rightarrow M - H \\
2(M - H) &\rightarrow M + H_{2}
\end{aligned}
\tag{10}
$$

$$
\begin{aligned}
M + H^{+} + e^{-} &\rightarrow M - H \\
M - H + H^{+} + e^{-} &\rightarrow M + H_{2}
\end{aligned}
\tag{11}
$$

Corrosion

Reactions can occur at the semiconductor surface in addition to the desired reactions of interest. These additional reactions can contribute to the electrochemical corrosion or decomposition of the semiconductor surface. Both anodic and cathodic dissolution can occur, via hole or electron interaction at the semiconductor surface, respectively. Oxidation can cause dissolution of metal ions from the semiconductor lattice, and cathodic decomposition can cause the reduction of metal ions at the surface of the semiconductor, coating the material with a thin metal layer. The following are cathodic and anodic reactions proposed for semiconductor dissolution, where MX is the compound semiconductor, and M is the metal in question [2].

$$MX + ze^{-} + solvent \rightarrow M + X_{solvent}^{z-} \tag{12}$$

$$MX + zh^{+} + solvent \rightarrow M_{solvent}^{z+} + X \tag{13}$$
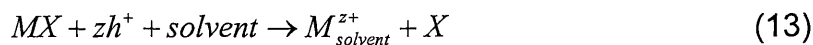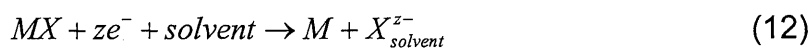
Each of these reactions will have a specific reaction potential associated with it. If the reaction potential lies within the water redox potentials in the dark, then these reactions may contribute to corrosion of the semiconductor surface. Under illumination, the potentials must lie not only outside of the water redox potentials, but outside of the semiconductor band edges to prevent corrosion. The reaction kinetics will also play a role in the competition between these processes. This makes predicting the dominant process of corrosion versus redox reaction very difficult.

References

1. Green, M.A., *Solar Cells: Operating Principles, Technology, and System Applications*. 1982, Kensington: University of New South Wales.

2. Memming, R., *Semiconductor Electrochemistry*. 2001, Weinhein: Wiley-VCH.

3. Bard, A.J. and L.R. Faulkner, *Electrochemical Methods: Fundamentals and Applications*. 1980, New York: John Wiley and Sons.

4. Paunovic, M. and M. Schlesinger, *Fundamentals of Electrochemical Deposition*. 1998, New York: John Wiley and Sons, Inc.

5. Lewis, N.S., *Progress in Understanding Electron-Transfer Reactions at Semiconductor/Liquid Interfaces*. Journal of Physical Chemistry B, 1998. **102**(25): p. 4943-4855.

6. Nozik, A.J., *Photoelectrochemistry: applications to solar energy conversion*, in *Annual review of physical chemistry, vol.29*. 1978. p. 189-222.

Appendix B
Mathematica Code for Theoretical Tandem Cell Efficiencies

This appendix shows the code used to calculate the efficiencies for a GuGaSe2/Si tandem photovoltaic device under both AM 0 and AM 1.5 solar irradiation. This was performed using Mathematica version 5.0.

```
<< Miscellaneous`PhysicalConstants`
```

```
a = ElectronCharge/(BoltzmannConstant 300 Kelvin)
```

$$\frac{38.6817\,Coulomb}{Joule}$$

This is a calculation of Jo based on literature values of Jsc and Voc for the highest recorded cell efficiencies to date (mA/cm2)

```
JZEROSI = 42.2 / ((Exp[.706 a Joule/Coulomb]) − 1)
```

5.82166×10^{-11}

```
JZEROCGS = 14.88/((Exp[.905 a Joule/Coulomb]) − 1)
```

9.31726×10^{-15}

```
JZEROLIST = {JZEROCGS, JZEROSI, JZEROCGS, JZEROSI}
```

$\{9.31726 \times 10^{-15},\ 5.82166 \times 10^{-11},\ 9.31726 \times 10^{-15},\ 5.82166 \times 10^{-11}\}$

The following are Jsc values obtained for CGS and for Si in a tandem from AM0 and AM1.5 data from NREL. Though I show both Jsc values for CGS and Si, those for Si are used for the following calculations, since the lowest Jsc value actually limits the the overall Jsc from the cell.

JSCCGSAM0 = 29.18
JSCSIAM0 = 23.82
JSCCGSAM15 = 23.01
JSCSIAM15 = 20.64
JSCLIST = {JSCSIAM0, JSCSIAM0, JSCSIAM15, JSCSIAM15}

29.18

23.82

23.01

20.64

{23.82, 23.82, 20.64, 20.64}

I will now calculate the theoretical open circuit voltages based on the Jsc theoretical and Jo calculated according to Green

VOCLIST = (1 Coulomb/a /Joule) Log[(JSCLIST/JZEROLIST) + 1]

{0.917164, 0.691215, 0.913459, 0.687511}

VOCCGSAM0 = Extract[VOCLIST, 1]

0.917164

VOCSIAM0 = Extract[VOCLIST, 2]

0.691215

VOCCGSAM15 = Extract[VOCLIST, 3]

0.913459

VOCSIAM15 = Extract[VOCLIST, 4]

0.687511

I now need to calculate the Vmp, and from that the Jmp so that I can calculate the fill factor

NSolve[a x $e^{\wedge}$(a x) + $e^{\wedge}$(a x) == (JSCSIAM0 / JZEROCGS) + 1, x]
x /. %

$$\left\{\left\{x \rightarrow \frac{0.826786 \, \text{Joule}}{\text{Coulomb}}\right\}\right\}$$

$$\left\{\frac{0.826786 \, \text{Joule}}{\text{Coulomb}}\right\}$$

$$\text{VMPCGSAM0} = \frac{0.8267862726375779 \, \text{Joule}}{\text{Coulomb}}$$

$$\frac{0.826786 \, \text{Joule}}{\text{Coulomb}}$$

NSolve[a x $e^{\wedge}$(a x) + $e^{\wedge}$(a x) == (JSCSIAM0 / JZEROSI) + 1, x]
x /. %

$$\left\{\left\{x \rightarrow \frac{0.608484 \, \text{Joule}}{\text{Coulomb}}\right\}\right\}$$

$$\left\{\frac{0.608484 \, \text{Joule}}{\text{Coulomb}}\right\}$$

$$\text{VMPSIAM0} = \frac{0.6084839718440133 \, \text{Joule}}{\text{Coulomb}}$$

$$\frac{0.608484 \, \text{Joule}}{\text{Coulomb}}$$

NSolve[a x $e^{\wedge}$(a x) + $e^{\wedge}$(a x) == (JSCSIAM15 / JZEROCGS) + 1, x]
x /. %

$$\left\{\left\{x \rightarrow \frac{0.823191 \, \text{Joule}}{\text{Coulomb}}\right\}\right\}$$

$$\left\{\frac{0.823191 \, \text{Joule}}{\text{Coulomb}}\right\}$$

$$\text{VMPCGSAM15} = \frac{0.8231910538237941 \, \text{Joule}}{\text{Coulomb}}$$

$$\frac{0.823191 \, \text{Joule}}{\text{Coulomb}}$$

NSolve[a x e^(a x) + e^(a x) == (JSCSIAM15/JZEROSI) + 1, x]

x /. %

$$\left\{\left\{x \rightarrow \frac{0.604925 \, \text{Joule}}{\text{Coulomb}}\right\}\right\}$$

$$\left\{\frac{0.604925 \, \text{Joule}}{\text{Coulomb}}\right\}$$

$$\text{VMPSIAM15} = \frac{0.6049249690789827^{\cdot} \, \text{Joule}}{\text{Coulomb}}$$

$$\frac{0.604925 \, \text{Joule}}{\text{Coulomb}}$$

VMPLIST = {VMPCGSAM0, VMPSIAM0, VMPCGSAM15, VMPSIAM15}

$$\left\{\frac{0.826786 \, \text{Joule}}{\text{Coulomb}}, \frac{0.608484 \, \text{Joule}}{\text{Coulomb}}, \frac{0.823191 \, \text{Joule}}{\text{Coulomb}}, \frac{0.604925 \, \text{Joule}}{\text{Coulomb}}\right\}$$

There are two ways to calculate FF. The first only needs Vmp not Jmp, and is from Fan

FFLIST = Coulomb / Joule (VMPLIST / VOCLIST)
(1 − ((Exp[a VMPLIST] − 1) / (Exp[a Joule VOCLIST / Coulomb] − 1)))

{0.874128, 0.844434, 0.87374, 0.843816}

FFCGSAM0 = Extract[FFLIST, 1]

0.874128

FFSIAM0 = Extract[FFLIST, 2]

0.844434

FFCGSAM15 = Extract[FFLIST, 3]

0.87374

FFSIAM15 = Extract[FFLIST, 4]

0.843816

Another way is by finding the Jmp from the diode equation, which will be used as comparison.

JMPLIST = JZEROLIST (Exp[a VMPLIST] − 1) − JSCLIST

{−23.0978, −22.8492, −20.0115, −19.7941}

FFLIST2 = Coulomb / Joule VMPLIST JMPLIST / (VOCLIST JSCLIST)

{−0.874128, −0.844434, −0.87374, −0.843816}

These give the SAME values! Now we can calculate efficiencies based on FFLIST and our smalles JSC vals

AM0EFFICIENCY =
JSCSIAM0 VOCSIAM0 FFSIAM0 + JSCSIAM0 VOCCGSAM0 FFCGSAM0

33.0003

AM15EFFICIENCY =
JSCSIAM15 VOCSIAM15 FFSIAM15 + JSCSIAM15 VOCCGSAM15 FFCGSAM15

28.4473